UNIVERSITY OF SOUTHAMPTON

THE USE OF A MAGNETIC SUSPENSION BALANCE FOR THE MEASUREMENT OF AERODYNAMIC MAGNUS FORCES ON A BODY OF REVOLUTION

by

Robert Ian Henderson

A Thesis submitted in fulfilment of the requirements for the Degree of Master of Philosophy

Department of Aeronautics and Astronautics

June 1976

UNIVERSITY OF SOUTHAMPTON

ABSTRACT

FACULTY OF ENGINEERING AND APPLIED SCIENCE

AERONAUTICS AND ASTRONAUTICS

Master of Philosophy

THE USE OF A MAGNETIC SUSPENSION BALANCE FOR THE MEASUREMENT OF AERODYNAMIC MAGNUS FORCES ON A BODY OF REVOLUTION

by Robert Ian Henderson

This thesis describes the development of equipment and techniques for the wind tunnel measurement of steady aerodynamic forces and moments, including Magnus effects, on an axisymmetric body with a variety of base shapes. The body had the basic shape of the 7-calibre Army Navy spinner. This work differs from most of the previous studies in using a magnetic balance and suspension system for the force measurements. The effects of sting or strut interference on the air flow have thus been eliminated, in particular allowing the effect of base geometry on the Magnus characteristics to be assessed.

Measurements have been confined to the low subsonic speed range (below 75 metres per second) and to Reynolds numbers in the range 0.54×10^6 to 0.79×10^6 referred to model length. For the greater part of the tests a transition band was employed at the nose of the model to ensure a fully turbulent boundary layer. In the Magnus measurements, spin rates up to 400 revolutions per second were used, the spin ratio covering the range 0 to 0.4.

Extensive data on the Magnus characteristics of the body with nine different base shapes are presented in an Appendix. The existence of a negative Magnus effect at the base is revealed for low angles of attack and low spin ratio. This is shown to disappear in the case of one particular base geometry.

TO LINNET

ACKNOWLEDGEMENTS

The work described in this thesis has followed on naturally from that of my supervisor, Dr. M.J. Goodyer, who, with Dr. M. Judd, designed and built the magnetic wind tunnel balance used for this series of measurements. I am also indebted to both for their practical help and for a continual supply of useful ideas. Dr. Goodyer is also responsible in large part for the summary of the Magnus force data presented in Chapter 8.

Thanks are also due to Miss S. Abdel Kawi, with whom the work load was shared during the earlier stages of development and during the steady aerodynamic tests.

Throughout the period of the contract, the wind tunnel facility

CORRIGENDA

Page	Line	Change
Acknowledgements	10	Replace 'steady' with 'simple'
Contents	4	Replace 'Steady' with 'Simple'
" "	5	Replace 'Steady' with 'Basic'
1	9	Replace 'steady and' with 'aerodynamic'
1	16	Replace 'Steady' with 'Basic'
3	3	Replace 'steady' with 'basic'
16	Title	Replace 'STEADY' with 'SIMPLE'
16	2	Replace 'steady' with 'basic'
16	3	Replace 'steady' with 'zero spin rate'
22	Title	Replace 'STEADY' with 'BASIC'
22	1	Replace 'steady' with'zero spin rate'

CONTENTS

1. INTRODUCTION

Over the past decade, magnetic balance-suspension systems for use with wind tunnels have been under development in various parts of the world, notably in Europe and the U.S.A. The novelty and inherent complexity of such devices has meant inevitably that much of the time and effort spent on them has been used in their improvement and on the development of test techniques, and that relatively little time has been spent on the acquisition of the aerodynamic data for which they were devised. This pattern has been repeated to some extent in the steady and Magnus force measurement work described in this thesis.

The work carried out has been supported by a contract from the Royal Armaments Research and Development Establishment at Fort Halstead, Sevenoaks. The initial contract was placed in 1970. One object was to develop techniques of Magnus force measurement with the magnetic balance, and produce results for the 7-calibre Army-Navy spinner which would supplement those already obtained from range firings. Steady aerodynamic measurements on the the same model were also to be undertaken in a preliminary investigation.

The original proposal was to use the 'low stiffness' method of force measurement outlined in section 6.1 of this thesis, whereby the size of the Magnus force resulting from pitch in the vertical plane is estimated from the displacement it gives to the model in the horizontal plane. This method was never actually used, since it proved possible to estimate force in the normal way from suspension system currents, with zero model displacement in the horizontal plane.

The testing was confined to the subsonic range. With the size of test model used, the length-based Reynolds number remained in the critical region for practical values of air speed (i.e. up to approximately 100 metres per second) and boundary layer tripping was necessary. A position upstream of the shoulder was chosen for a roughness band. Some tests were also carried out without boundary layer tripping.

When the capability of detecting and measuring Magnus force on the basic shape had been demonstrated, R.A.R.D.E. granted an extension to the contract of one year to continue the work on a number of base geometries. Specifically, these were:

Case	Base configuration
1.	The basic blunt base.
2.	The blunt base, but with a corner radius of 4.6% of the base diameter (D).
3.	A hemispherical base.
4.	A 5° half-angle boattail base, length 0.5D.
5.	A 5° half-angle boattail base, length 1.0D.
6.	A 10° half-angle boattail base, length 0.5D.
7.	A 10° half-angle boattail base, length 1.0D.
8.	A 10° boattail base, as case 7, but with a base cavity, depth 0.071D, diameter 93% of local base diameter.
9.	As case 8, but with a cavity depth of 0.213D.

Spin rates of 24,000 r.p.m. could be attained with the aerodynamic spinning device developed for the Magnus work, giving a peripheral speed of 27.7 metres per second, and thus a spin ratio (pD/2V) of 0.42 at an air speed of 65 metres per second.

For the greater part of the work, the length of time required for data acquisition was shortened by the use of a tape recording technique, the analysis being left to a later date, and performed on a small digital computer. The success of this method, and of the complete system, is shown in the data presented in this thesis. A large amount of data has been processed and plotted in graphical form, each graph representing the result of a single test run lasting 120 seconds. This forms the first comprehensive set of data on the effect of base shape on the Magnus characteristics of the 7-calibre Army-Navy spinner. It has been found that the precise configuration of the base has a very large influence on the sign and magnitude of the Magnus force and Magnus moment in the range of pitch incidences covered, 0 to 7°.

In the thesis which follows, no attempt has been made at a theoretical model of the spinning projectile. The work has consisted entirely in the measurement of the Magnus and steady aerodynamic forces on the test model. However, a brief summary of some of the published theoretical work on the Magnus effect has been included in Chapter 5.

2. DESCRIPTION OF THE FACILITY

2.1. The high-speed wind tunnel

The wind tunnel used for the measurements described in this thesis is a closed circuit induced-flow atmospheric tunnel the design of which is based on a similar one developed at the National Physical Laboratory. The working section, around which are mounted the suspension system electromagnets, is hard-walled and constructed from 1 inch thick Tufnol. Its internal dimensions at the centre of the test section are 20 cm high and 15 cm wide, and the vertical dimension increases downstream at the rate of 8 mm per metre to compensate for boundary layer growth. The floor of the test section is a plate of toughened glass approximately 20 mm thick. The tunnel is driven by an injector unit consisting of four slots of individually adjustable aperture fed from a single manually operated valve in the compressed air line (the supply is at a nominal 250 p.s.i.). The return circuit is constructed of plywood and is directly above the working section/ injector part of the tunnel. A group of wire mesh screens, two of a fine mesh and two of a coarser mesh, is placed a short distance upstream of the contraction section to reduce the turbulence level. Hot wire probe measurements* of the turbulent intensity at representative airspeeds on the centre line of the working section give a root mean square velocity fluctuation of 0.15% of the free stream velocity.

2.2 The Magnetic Suspension System

2.2.1 Introduction

The Univeristy of Southampton magnetic suspension wind tunnel balance is an existing facility, developed around the 20 x 15 cm high speed wind tunnel described in the first section.[1] In its normal mode of operation it acts as a 6 degree-of-freedom position control servo of type 1, that is, it incorporates integral of position error feedback in all control loops. Control forces are applied magnetically by means of an array of 7 electromagnets arranged around the working section and driven from 6 independent phase-fired thyristor power supplies. The fields generated by the electromagnets act on permanent magnets fixed in the model, the main magnet being, typically, a cylindrical bar of Alcomax III, the others being subsidiary magnets of Platinax II or samarium cobalt. For applications not requiring the use of roll

---

* Surveys of the test section flow angularity and turbulence levels appear in Appendices C and D, respectively.

control the subsidiary magnets are not needed.

Feedback signals for the servo loops are produced photoelectrically be means of light source photocell pairs, the exact geometrical arrangement depending on the shape of the model to be tested. The output of each photovoltaic cell is ideally a linear function of the area illuminated, and thus of the position of the edge of the model being monitored. In order to produce signals representing translation or rotation about orthogonal axes, the outputs are combined in operational amplifier summing circuits in the required proportions. Two sets of position sensors are employed in most applications: primary sensors, with a range of approximately ±1 cm (limited by the physical size of the beam and cell, or the diameter of the model, whichever is the smaller); and secondary sensors, with a diameter of approximately 1 mm. The main signals for the position control loops are derived from the primary cells, and for applications requiring precise positioning the integrators are fed from the secondary cells, whose small dimensions minimise the effect of drift.

The compensation system, which provides the stability and determines the response characteristics of the suspension system, is divided into 6 separate parts, one dealing with each degree of freedom. The compensator for any particular loop consists of a number of cascaded phase-advance circuits (usually two, although three have been used on occasior) with the facility for gain adjustment. In addition, the bandwidth of the system is limited with several simple lag elements to attenuate high frequency noise, in particular that produced by the thyristor power amplifiers. In normal operation, integral-of-position-error feedback is introduced into each loop to reduce the steady-stateerror to zero.

2.2.2. The electromagnet array

(a) the lateral plane

A symmetrical arrangement of 4 magnets is employed for control of position in the horizontal plane. Each magnet comprises three independent windings, one of which is fed with a constant current (the 'bias' current) and the other two of which are used for control. Referring to Fig. 2.1, each of the two lateral thyristor power amplifiers drives current through a right- and a left-hand electromagnet producing a magnetic field which is uniform in the region of the

centre-line of the wind tunnel and directed at right angles to it. The bias current is arranged to flow so as to produce fields in the opposite direction to the control fields, so allowing the unidirectional thyristor supplies to reverse the resultant fields. The bias and control windings each consist of approximately 130 turns, therefore a standing current approximately equal to the bias current is required from the lateral power amplifiers for zero magnetic field.

As indicated in Fig. 2.1, the two right-hand (and the two left-hand) sets of coils are each wound on a common 'horseshoe' of transformer steel laminations. The presence of the laminations improves the rigidity of the coil support structure and increases the field strength for a given current, but disadvantages are that unwanted coupling is introduced between the forward and aft coils, the inductance of the control coils is increased and there is the possibility of hysteresis.

The third coil on each electromagnet is used for the independent control of roll attitude, but in this case was not required.

(b) The vertical plane

At the present time, the deployment of electromagnets in the vertical plane is asymmetrical, with a single 'horseshoe' mounted above the upper wall of the wind tunnel. As with the lateral magnets there are 3 separate windings on each 'leg' of the horseshoe, but in this case each set is series connected to a power amplifier. Gravity provides a bias force, and therefore the vertical control currents stand at a level dependent on the weight of the model, on the strength and geometry of the permanent magnet, and on the vertical position of the model.

(c) The axial direction

A pair of concentric coils is used to apply forces along the axis of the wind tunnel. They are air-cored and wound around the working section in close proximity to the other electromagnets, but upstream of them. The inner of the pair consists of approximately 500 turns of 12 s.w.g. copper wire, and the outer of 400 turns. The two windings are usually connected in parallel. However, in the experimental work described here, one of the windings was used to carry bias current; as in the case of the lateral coils, this was to allow both positive and negative forces to be applied to the model. Because of its greater

cross-sectional area, the inductance of the axial coil is larger than that of the other control coils, despite its having no soft-iron core.

The principle of axial force generation with this system is illustrated in Fig. 2.2, As with all the force components it can be thought of as arising from the integral of the scalar product of the field gradient with the magnetic moment per unit length of the bar magnet. Alternatively, the pole of the bar magnet nearer the coil experiences a greater force of attraction than the other pole's repulsion.

2.2.3. Position sensing

The position sensing system chosen for the University of Southampton magnetic balance is an optical one. Several beams of light approximately 2 cm in width are directed across the edges of the model towards photosensors. With the model removed the whole width of each beam falls on its photosensor, which consists of a focussing lens and photovoltaic cell. For axisymmetric bodies, or winged models with cylindrical fuselages, a crossed beam arrangement is employed. The light sources are mounted outside the wind tunnel and direct beams though small windows in the upper corners of the working section so as to intercept the lower edge of the body before emerging from the glass floor. The photosensors are placed beneath the lower window to receive the light beams. There is one pair of crossed beams for each end of the model, so that information on vertical and horizontal position, and pitch and yaw, can all be extracted from these four position signals.

The arrangement is simpler for axial position monitoring, with only one cell receiving the movements in this degree-of-freedom. It has been found advantageous to use the shadow cast by the nose, rather than the tail, as this allows greater freedom in the choice of model base geometry.

For accurate positioning, and freedom from drift, three small 'secondary' sensors are employed, one with its own light source. The small physical size of these cells (1mm x 2mm) makes errors in indicated position far less sensitive to changes in beam intensity than the main sensors. The accumulation of dust on the windows in the test section

is one of the main cuases of positional drift during a test, and drift can alter the force and moment calibrations significantly.

2 .2.4. The control system

As stated in section 2 .2.1, the control system for position and attitude stabilisation divides naturally into 6 individual subsystems, each dealing with one translational or rotational degree of freedom. For each subsystem, an input signal, proportional to displacement or rotation about one axis, must be extracted from the outputs of the position sensors. This signal is then subtracted from a voltage representing the desired attitude of the model. The difference signal is then input to the compensation circuit, where the response characteristics of the system are determined. The final stage portions out the compensated signals into the thyristor power amplifiers, so as to produce, as far as possible, pure forces or torques on the model.

A functional block diagram of the complete system is shown in Fig. 2 .3 and the control system for a single degree of freedom in Fig. 2 .4.

2 .2.5. Component transfer functions

(i) Model in magnetic field

The geometry of the electromagnet system makes it simpler to use a magnetic pole approach for all except rolling motions, which will not be discussed here. Forces and torques are developed on the permanent magnet inside the model which is considered as a dipole of length ℓ, with a pole strength q_m. Considering first, vertical and horizontal heaving motions of the model, the force on the model is

$$\underline{F} = q_m \underline{H}_1 - q_m \underline{H}_2$$

where $\underline{H}_1$, $\underline{H}_2$ are the magnetic field vectors at each pole.* For simplicity, we can assume $\underline{H}_1 = -\underline{H}_2$, and consider the force acting on one half of the model. Thus, the z component of the force is

$$F_z = 2q_m H_z;$$

where H_z is the z-component of the field at one end of the magnet. The field in the vicinity of the pole may possess a finite gradient, $\partial H_z/\partial z$,

* Symbols are defined in the Nomenclature.

and this must be taken into account in the equation of motion. Therefore, expanding H_z in a Taylor series about $z = z_o$ to first order gives

$$H_z = H_{z_o} + (z - z_o)\, \partial H_z/\partial z.$$

A linear dependence of H_z on the current flowing in the electromagnets producing it is assumed and also that the effect of a change in z on the gradient of H_z with current i is negligible, i.e., that $\partial^2 H_z/\partial i \partial z = 0$. The equation of motion for the z direction then becomes

$$m\, \partial^2 z/\partial t^2 = 2q_m \left\{ i(t)\, \partial H_z/\partial i + (z - z_o)\, \partial H_z/\partial z \right\}$$

Taking the Laplace transform and rearranging:

$$\frac{Z(s)}{I(s)} = \frac{\partial H_z/\partial i}{(m/2q_m)s^2 - \partial H_z/\partial z}$$

A corresponding equation exists for the rotational modes of motion with the mass, m, replaced by the moment of inertia, I_1, z replaced by α, q_m replaced by $q_m \ell/2$,

$$\frac{A(s)}{I(s)} = \frac{\partial H_z/\partial i}{(I_1/q_m \ell)s^2 - \partial H_z/\partial z} \qquad 2.1$$

In the horizontal plane, symmetry of the electromagnet array ensures that $\partial H_y/\partial y \approx 0$. A small negative gradient in fact exists, arising from the field of the suspension coils mounted over the working section. This field has a sizeable positive gradient in the vertical (or z) direction.* A similar small lateral gradient arises from the field of the axial coil. In order to linearise the equations so that the Laplace transform can be used, it has been assumed that the field gradients are independent of the contribution of the lateral magnets to the field strength, and that the other fields do not vary.

---

* See footnote under section 6.1.

(ii) Power amplifiers and coils

The power amplifiers driving the suspension coils are all phase-fired thyristor units operating from 3-phase 440 volt mains. Their commutating frequency is therefore 150 Hz, which is far enough above the frequencies of interest in the control circuits for their transfer function to be assumed a constant. They are connected to the coils of the suspension system through load resistors of 1 or 2 ohms. The inductance of a typical coil is approximately 40 mH, and its resistance 0.2 ohms. Capacitance is small enough to be neglected.

The transfer function of a coil or coil pair can thus be approximated to a simple lag:

$$\frac{I(s)}{E(s)} = \frac{1/R}{s\tau + 1}$$

where $\tau = L_c/R$ and L_c = the coil inductance, R = total circuit resistance. Typical values for τ are in the region of 0.035 sec.

(iii) Position sensors

A simple lag is normally included in the amplification stage of a position sensor to reduce random noise. The time-constant is usually approximately 0.001 sec, and can be neglected for the purpose of feedback design.

2.2.6. Control system stabilisation and compensation

The compensation of the control system responsible for the vertical position of the model will be discussed as an illustration.

The root locus of the uncompensated system is shown in Fig. 2.5. The poles on the real axis at ± 12.5 sec^{-1} result from the denominator of equation (2.1) and are a consequence of the field gradient, which splits what would otherwise be a second order pole at the origin. The pole at -30 sec^{-1} is the result of the transfer function of the electromagnets and their power supplies. (Values have been calculated for the model used eventually in the Magnus force measurements). It can be seen that there is always a root of the characteristic equation in the right-half plane, no matter what the loop gain, and that compensation is essential for stability. The compensator used in all control loops was a phase-advance network built around an operational amplifier, and at least two such stages were needed in order to provide an adequate margin of stability. The transfer function of the

arrangement of Figure 2.6 is

$$G(s) = K\frac{(1 + k\tau s)}{(1 + \tau_1 s)}$$

where $k = (R_1 + R_2)/R_2$, $\tau_1 = R_1R_2C/(R_1 + R_2)$ and $K = R_3/(R_1 + R_2)$.

This circuit was used for the ease with which its gain could be varied (by placing a potentiometer at R_3) and because of the possibility of adding a feedback capacitor in parallel with R_3, if needed, to reduce the bandwidth at high frequencies. This was necessitated by the high noise levels of the position signals, originating largely from the switching transients of the thyristor power supplies.

The pole-zero diagram of the phase lead network is shown in Fig. 2.7 the pole lying at $-1/\tau_1$, and the zero at $-1/k\tau_1$.

The first step in the design if a suitable compensator was to choose a location for the closed loop roots of the final system, based on the required damping ratio and settling time. A damping ratio of 0.5 was deemed adequate, with a settling time of 0.2 seconds, giving the required root locations as:

$$s = -20 \pm 20\sqrt{3}j$$

The locations of the compensator zeros were then chosen to be as close to the desired root location as possible, without coming inside the pole at -30, which would alter the form of the root locus. The position of the poles of the compensator were calculated from the 'angle requirement' that the vector sum of the angles from the poles and zeros must be 180^o at the roots. The loop gain of the system was evaluated from the 'magnitude requirement'

$$K_p = \frac{|z_1|\ |z_2|\ldots|s-p_1|\ |s-p_2|\ldots}{|p_1|\ |p_2|\ldots|s-z_1|\ |s-z_2|\ldots}$$

The transfer function of a suitable compensator with two identical stages was thus found to be

$$G(s) = \left(K \frac{(0.031s + 1)}{(0.0027s + 1)} \right)^2$$

Suitable component values, choosing R_1 = 51k, would be: R_2 = 4.9k, C = 0.6 μF. The loop gain, K_p, was calculated to be 8.7. A sketch of the root locus for this particular case is shown in Fig. 2-8.

Similar computations were carried out for the other loops. Values obtained were not strictly adhered to in the final design, as it is possible to improve performance by shifting the zeros of the compensator individually, bringing one of them inside the pole at -30, for instance. In addition, integral feedback was added in most cases, which placed a pole at the origin of the s-plane and a zero a small distance along the real axis, see Fig. 2-9. This has a small destabilising effect on the system, the precise effect depending on the location of the integrator zero. A normal position would be at -10 sec^{-1}, with an integrator time constant of 0.1 sec.

2.2.7. Calibration of the balance

(i) Vertical forces and moments

Calibration of the suspension system for forces and moments in the vertical plane is, in principle, the easiest to carry out, as it is a relatively simple matter to suspend weights from the test model and record the electromagnet currents required to keep it stationary. Normally, the currents are not themselves recorded; instead, the voltage developed across a shunt in the circuit is amplified and displayed on a digital voltmeter. For the body of revolution used in the Magnus tests, a number of 'collars' of assorted weights were produced. These could be slipped over the model and fixed in any desired position.

Force calibrations were carried out by fixing weights at the reference point chosen for moment measurements and plotting the relevant vertical coil current signals against the weight. The calibration was usually performed at a small number of pitch incidences, e.g. 0^{o}, 5^{o}, 10^{o}, 15^{o}. Moment calibrations were similar, except that a single weight was selected and moved to various positions along the body.

In both cases, the axial current was plotted in addition to the two vertical coil currents. This is because there is a considerable interaction between the three coils, owing to the induction of magnetic pole strength in the upstream leg of the iron yoke by the axial field. This induced effect largely cancels in the lateral system because of the symmetry of that magnet array.

Linearity of the plots is usually excellent. The lift force and pitching moment in the balance axes can therefore be expressed by the following equations;

$$F_z = c_{11}e_1 + c_{12}e_2 + c_{13}e_3$$

$$T_\alpha = c_{21}e_1 + c_{22}e_2 + c_{23}e_3$$

where F_z, T_α are the force and moment components, and e_1, e_2, e_3 are the voltage changes (at the outputs of the current signal amplifiers) produced by the application of these forces.

The procedure for evaluating the constants c_{ij} from the slopes of the calibration curves will be dealt with in the next section.

(ii) Axial forces

Axial forces can be applied at the reference point by means of a thread, passing horizontally over a lightweight pulley on a low-friction bearing. The calibration method is similar to that used for the vertical suspension, the same three current signals being plotted, this time versus axial force, or drag. Care has to be taken that the

thread is accurately aligned with the horizontal, so that a pure drag force is applied.

Once again, linearity of the calibration curves at any particular pitch incidence allows the following equation to be written:

$$F_x = c_{31}e_1 + c_{32}e_2 + c_{33}e_3$$

The equations for F_z, T_α and F_x can now be combined to form the matrix equation:

$$\begin{bmatrix} F_z \\ T_\alpha \\ F_x \end{bmatrix} = \underline{C} \begin{bmatrix} e_1 \\ e_2 \\ e_3 \end{bmatrix}$$

Multiplying both sides by the inverse matrix $\underline{C}^{-1}$:

$$\begin{bmatrix} e_1 \\ e_2 \\ e_3 \end{bmatrix} = \underline{C}^{-1} \begin{bmatrix} F_z \\ T_\alpha \\ F_x \end{bmatrix}$$

It can now be seen that the coefficients of the matrix $\underline{C}^{-1}$ are the slopes of the calibration curves, e.g.:

$$e_1 = (\partial e_1/\partial F_z)F_z + (\partial e_1/\partial T_\alpha)T_\alpha + (\partial e_1/\partial F_x)F_x$$

Therefore, by forming the matrix $\underline{C}^{-1}$ from the calibration slopes and inverting, either by hand, or on a computer, the $\underline{C}$ matrix is obtained. The formation of the $\underline{C}^{-1}$ matrix is carried out at each of the pitch incidences used in calibration. For incidences inbetween, the values of the coefficients can be found by linear interpolation.

(iii) Lateral forces and moments

Calibration is somewhat simpler in the horizontal plane, as the axial current signal need not be taken into account. In addition, calibration at one yaw incidence is usually sufficient, as the effect of yaw on the coefficients is small, again owing to the symmetry of the electromagnet system and to the relatively small field gradients in the horizontal direction. For the tests dealt with in this report, yaw was fixed at 0^o, so a single calibration was adequate.

Forces were applied by means of a thread, attached to a light collar which could be moved along the model, to alter the moment being applied. Two light pulleys brought the thread out of the working section and into an accessible position, where weights could be applied.

In all respects, the calibration procedure is similar to that employed for the vertical components, except that the matrix of coefficients is smaller, being only 2 x 2.

3. THE USE OF THE MAGNETIC SUSPENSION SYSTEM FOR STEADY AERODYNAMIC TESTING

3.1 Introduction

One of the uses of a magnetic suspension balance is for sting-free measurements* of steady aerodynamic coefficients. As a complement to the later Magnus force measurements, steady testing was performed on the basic model at subsonic speeds. Because of the small size of the wind-tunnel test section, the length-based Reynolds numbers were low ($< 10^6$). Comparison was made with the results of tests on a similar model at approximately twice the Reynolds number and with a sting support[19].

3.2 The Test Model

The model used in all the measurements described in this thesis was the 7-calibre Army-Navy spinner, the outline of which is shown in Fig. 3.1. The scale of the model was chosen to be small enough to keep the wind tunnel blockage small (ratio of cross sectional area of model to cross sectional area of tunnel $\sim 1\%$), while large enough to allow a permanent magnet of sufficient length and diameter for adequate control by the suspension system. A diameter of 22 mm was selected, giving a model length of 154 mm. An Alcomax III magnet (see also section 6.2.2) with a length of 101 mm and a diameter of 15.9 mm was used.

The model was constructed in brass and aluminium. The magnet was inserted from the tail end and held in place by a threaded base section. It was also possible to unscrew the nose for replacement in the event of damage.

For tests with the boundary layer tripped, a hoop of 0.25 mm diameter wire was fixed in place at the shoulder, i.e. where the nose and cylindrical portions meet. (The position of the roughness band detailed in Fig. 3.1. applies only to the Magnus force tests.) The diameter of this wire was large enough to produce a turbulent boundary layer with its starting point at the shoulder. (See also section 6.6.5.)

---

* An investigation of the effect of sting supports of various diameters on the subsonic drag coefficient of an axisymmetric body can be found in Appendix B.

3.3 System Modifications

During the course of this work, large parts of the established electronics of the control system were rebuilt using dual operational amplifiers (Type 810 CE, Souriau Inc.). The whole of the suspension system electronics, with the exception of the stabilised power supplies, was housed in one 19 inch (483 mm) by 38 inch (965 mm) rack cabinet. Feedback circuits and operational amplifiers were wired on separate plug-in "Veroboard" modules. This allowed easy replacement of a failed operational amplifier and maximised the number of contacts available at the rear of the unit for interstage wiring. All permanent connections were made to coaxial sockets on the side panel of the unit, while the inputs and outputs of each stage were brought out to 'wander' sockets on the front panel.

The ten-turn position control potentiometers, integrator switches and milliameters monitoring model position were housed in a separate unit. Connection between the two units was made through coaxial cables.

The rearrangement of the electronics had the advantage of greater accessibility and interchangeability of feedback and amplifying sub-units, and the improved reliability afforded by integrated circuit operational amplifiers.

3.4 Preliminary adjustments

3.4.1 Position sensor alignment

Each particular model geometry tested in the magnetic suspension balance requires its own arrangement of optical position sensors. In the present case of a slender body of revolution, four diagonal light beams (see section 2.2.3) were the most suitable for sensing position in the horizontal and vertical planes. A beam reflected vertically downwards from the roof of the working section and into a sensor beneath the tail of the model was used to detect axial position.

The procedure for setting up the optical position sensors was as follows:

(i) The optical surfaces, including lenses, light bulbs, and the glass floor of the working section, were cleaned.

(ii) The voltages applied to the bulbs were then set equal to the

level to be used in calibration and all subsequent aerodynamic tests. This was usually 5.00 volts ± 0.01 volts for the bulbs rated at 6 volts, 6 watts, as running the lamps below their normal rated voltage increased their lifetime and reduced the likelihood of failure during the series of tests. Stabilised supplies were used for all the light sources.

(iii) The response of each of the position sensors was adjusted such that their output voltage changed linearly with the movement of the shadow edge across the sensor. This required adjustment of the light source to produce a defocussed image of the bulb filament across the slot aperture in front of the position sensor. When a sufficiently uniform illumination had been achieved, the light sources and photocells were clamped in position.

3.4.2 Combiner adjustments

The adjustment of the 'combiners' followed the position sensor adjustments of section 3.4.1. The object was to produce an independent signal from each of the five circuits proportional to displacement in one degree of freedom only. This entailed the adjustment of the gains of eight summing amplifiers. The first four stages produced signals proportional to vertical and horizontal displacements of the nose and tail of the model. The final four stages added and subtracted these voltages in the correct proportions, giving outputs dependent on vertical and horizontal heave, and pitch and yaw.

To aid in this adjustment, a jig was used which moved the model in purely vertical or horizontal directions. The summing amplifier gains were set such that the heaving motions of the model produced minimum variation in the pitch and yaw position signals over the range of movement expected for the model. As the model was to be held in a nominally constant position throughout the tests, excepting for deliberate changes in pitch attitude, the range of movement in heave was relatively small (±2 mm), and the gains were therefore easily optimised.

For the adjustment of the pitch combiners, the model was fitted into a jig allowing only pitching motion. The same jig could be rotated through 90° about the wind tunnel axis for adjustments to the yaw combiner. Gains were optimised such that changes in the pitch and yaw position signals over the expected range (-2° to $+15^{\circ}$ for pitch, $\pm 2^{\circ}$ for yaw) caused minimum changes in the heave position signals.

3.4.3 Compensation adjustments

Before suspending the model, the zero adjustment of the final amplifiers feeding the thyristor power supplies had to be set such that, with zero position signals, the vertical suspension currents were close to the levels needed to support the model in its nominal zero position. Similarly, the standing level of the lateral control currents required to be set nearly equal to the bias current with zero horizontal position signals.

In addition, the integrators for each degree of freedom were zeroed by placing the model (without permanent magnetic core) in the working section at its nominal zero position and switching on the suspension currents. The integrator zero adjust potentiometer was then turned until the currents remained at a steady value when the integrator switch was opened.

The loop gain of each of the five servo channels was then optimised for best stability of the model at zero incidence. The axial control system was rendered inoperative while the horizontal and vertical control loops were adjusted. The model would remain stable in axial position at zero incidence in the absence of axial feedback control owing to the tendency of the magnetic core to hang directly beneath the poles of the vertical suspension coils. (See footnote under section 6.1.) Axial damping in this situation was, however, almost zero.

With the model sufficiently stable at zero incidence, the axial control could be brought in and adjusted in the same way. Control of axial position allowed the pitch incidence to be altered without loss of the model from suspension. The loop gains of the vertical heave and pitch circuits could then be re-adjusted for best mean stability over the full range of incidence.

Finally, the integrators were switched in. This usually had the effect of degrading the stability (see section 2.2.6), but only to a small extent, as the time-constant of the integrators was chosen to be long in comparison with the response time of the control circuits.

When setting up the system for a new model, adjustment of the gains of the control loops was occasionally insufficient, and the values of the fixed capacitors in the phase-advance stages required changing. This was carried out on a semi-empirical basis.

3.5 Calibration

3.5.1 Pitch incidence calibration

A series of simple aluminium jigs were used to hold the model in fixed pitch incidences of 0^{o}, 5^{o}, 10^{o}, 15^{o} and 20^{o} with respect to the tunnel floor, and at nominal zero position in other degrees of freedom. The model was placed such that the axial position indicator showed nominal zero position. A digital voltmeter was used to set the pitch position signal to 0.0 volts at nominal zero incidence, and to measure the output voltage at each of the other incidences.
A graph of position signal versus incidence was plotted.

3.5.2 Force and moment calibration

The principle of the method of calibration has been dealt with in section 2.2.7. A number of brass and aluminium collars were produced which could be slid over the model and clamped in position by nylon screws. The weights of the collars ranged from approximately 10 grams to 100 grams.

Force calibration in the vertical plane was carried out by placing each of the weights in turn with its centre of mass at the chosen reference point for moment measurements (in this case the centre of the cylindrical afterbody) and noting down the outputs of the current signal amplifiers. This was repeated at each of the pitch incidences provided by the pitch calibration jigs, and plots were made of the current signals versus applied force. Forward and rear vertical suspension current signals and axial current signals were plotted.

The calibration matrix '$\underline{C}^{-1}$', relating applied forces and moments to the changes in the current signals (see section 2.2.7, part (iii)) was formed for each pitch incidence. Using a FORTRAN program on the University ICL 1907 computer, the inverse matrices were produced. The variation of each matrix element with incidence was then fitted to a straight line by the method of least squares. The value of each element at zero incidence was placed in matrix '$\underline{A}$', and the slope of the fitted straight line was placed in the corresponding position in matrix '$\underline{B}$'. Thus

$$\underline{C} = \underline{A} + \alpha \underline{B},$$

where α is the pitch incidence. Using numerical values derived in this way, the equation relating forces and moments to the measured current signals becomes

$$\begin{bmatrix} F_Z \\ T \\ F_x \end{bmatrix} = \begin{bmatrix} -0.24 & 12.2 & 2.5 \\ 10.6 & -10.2 & -0.52 \\ 1.2 & -3.48 & -24.57 \end{bmatrix} \begin{bmatrix} e_1 \\ e_2 \\ e_3 \end{bmatrix} + \alpha \begin{bmatrix} -0.08 & 0.12 & -0.336 \\ -0.05 & 0.17 & 0.202 \\ -0.32 & -0.04 & -0.207 \end{bmatrix} \begin{bmatrix} e_1 \\ e_2 \\ e_3 \end{bmatrix} \quad . \quad (3.1)$$

3.6 Measurement of Forces and Moments

The essence of the measurement procedure was to record the changes in the three significant current signals (forward and aft vertical signals, and the axial current signal) when the tunnel was run up to the testing speed. The tunnel would be run for approximately one minute at a selected dynamic head while the output voltages of the three current signal amplifiers were written down. Digital voltmeters were used for accuracy and convenience. The 'wind off' readings were taken both before and after the 'wind on' tests and the values averaged (small drifts usually occurred during a test run, partly as a result of dust deposition on the glass floor of the tunnel).

The mean readings of a number of tests at the same pitch incidence were finally input as data to a FORTRAN program which evaluated equation 3.1.

4. STEADY FORCE AND MOMENT DATA FROM THE 7-CALIBRE ARMY-NAVY SPINNER

This short chapter presents the results of the series of steady aerodynamic tests on the basic spinner, using the magnetic suspension system and the technique described in Chapter 3. The results represent the mean of a large number of separate measurements made in the range 35 - 70 metres/sec ($Re_L = 0.38 - 0.75 \times 10^6$). A boundary layer trip, in the form of a hoop of 0.010-inch (0.25 mm) diameter wire attached at the shoulder, was used throughout the measurements.

4.1 Normal force coefficient

The normal force coefficient is here defined as

$$C_Z = C_L \cos\alpha + C_D \sin\alpha,$$

where C_L, C_D are the lift and drag coefficients, and α is the pitch angle. C_Z is plotted against α in Fig. 4.1. Data from reference 19 is included on the diagram for comparison. The latter was obtained from a 7-calibre model with a tangent ogive nose (the nose of the 7-calibre AN spinner does not meet the afterbody at a tangent), a sting support was used, and the length-based Reynolds number was approximately double that of the present data.

4.2 Moment coefficient

Here, the moment coefficient is defined

$$C_M = M/qSD,$$

where M = pitching moment, q = dynamic head, S = cross-sectional area of model, and D = diameter of model. The moment measurements were referred to the tail of the model, to allow comparison with the Australian data of Fletcher[19]. C_M is plotted against pitch angle in Fig. 4.2.

4.3 Drag Coefficient

Fig. 4.3 shows the approximately parabolic form of the $C_D - \alpha$ curve. The values of C_D and C_L^2 at corresponding pitch incidences are also shown in Fig. 4.4. The latter indicates that the 'parabola of the induced drag' is not a true parabola in the present case.

5. THE MAGNUS EFFECT

5.1 Introduction

The rotation of a body of revolution about its axis of symmetry gives rise to a number of aerodynamic effects, the most important of which occurs when the body is placed at incidence to a uniform flow. The resulting component of aerodynamic force generated normal to the plane containing the flow vector and axis of rotation is termed the Magnus force, in honour of Gustav Magnus, who first demonstrated the effect of spin on the flight paths of cannon balls. Classically, the rotation of a cylinder in flow perpendicular to its axis is regarded as a doublet-plus-vortex in uniform flow, and the lift is given by the Kutta-Joukowski equation:

$$L = \rho V \Gamma \ell,$$

where ρ = fluid density, V = free stream velocity, Γ = circulation, and ℓ = length of cylinder. This simple potential flow model has a critical state when the front and rear stagnation points coalesce as shown in Fig. 5.1.

This picture is unfortunately of little use in predicting the Magnus forces on spinning projectiles under real flow conditions, since viscous and three- dimensional effects must be taken into account. The real flow depends very strongly on the state of the boundary layer on the body, which in turn, is influenced by Reynolds number, surface conditions, pressure gradients and spin. There is generally flow separation on the lee side of a projectile at incidences greater than a few degrees, and the positions of the separation lines are also greatly influenced by the above effects, as are the strengths of the vortex sheets. For these reasons, a fairly detailed examination of the flow field around a spinning body of revolution is needed in order to comprehend the Magnus mechanism, especially in cases where the boundary layer undergoes transition from laminar to turbulent flow.

5.2 Observed flow patterns

The earliest studies of the effect of spin on the flow past a 2-dimensional cylinder, made by Lafay[2], revealed the existence of a negative Magnus force (i.e. one of opposite sign to that predicted classically), which has now been shown to be the result of boundary layer transition[3,4]. As shown in Fig. 5.2, the flow velocity relative to the surface of the upper part of the cylinder is lower than that relative to the lower part. In the critical Reynolds number regime this can lead to laminar separation on the upper half and turbulent separation on the lower (in practice , a 'bubble' forms ahead of the true turbulent separation point, as a result of initial laminar separation and subsequent turbulent reattachment). The effect[4] of this on the Magnus force coefficient can be seen in Fig. 5.3.

In the 3-dimensional case of a cylindrical body at incidence to the flow, the separating flow generates a pair of vortex sheets on the lee side whose development along the length of the cylinder is analogous to the development of vortices with time behind an impulsively started 2-dimensional cylinder. The effect of spin on the development of these vortices is complicated by the additional effect of boundary layer transition, which can alter the location of the separation lines. At low angles of incidence the vortex sheets can remain embedded within the developing boundary layer. Smoke flow visualisation experiments have been carried out by a number of workers at the University of Notre Dame[5,6,7].

The effect of spin on the location of the laminar-turbulent transition line on a yawed cylinder has been investigated both experimentally and theoretically by Jacobsen and Morton[8,9], who deduce that the transition line becomes skewed in the direction of rotation. The situation is probably more complicated with increasing angle of attack because of flow separation along the lee side.

The form taken by the flow field is a strong function of the state of the boundary layer conditions, so that anything which has an effect on the boundary layer is likely to affect the Magnus characteristics of a projectile. Effects include Reynolds number, surface roughness, pressure gradients arising from the geometry of the body and flow unsteadiness.

5.3 Some theoretical predictions

Theoretical approaches to the prediction of the Magnus force on spinning shapes will not be discussed in detail here, but some of the results of theoretical investigations will be presented.

The semi-infinite yawed cylinder was considered by Martin[10], whose basic boundary layer work is now regarded as something of a classic in the field. Using small perturbations in angle of incidence and spin rate, he predicted the laminar boundary layer velocity profiles and the variation of displacement thickness as a function of the azimuthal angle around the cylinder. Considering the potential flow around the 'new' body, bounded by the displacement thickness, he computed the side force F_Y and moment M_Y, as follows:

$$F_Y = 13.15\ (Re_L)^{-\frac{1}{2}}(2L/D)^2\ (pD/2V)q\ S\alpha$$

$$M_Y = 7.89\ (Re_L)^{-\frac{1}{2}}\ (2L/D)^2\ (pD/2V)q\ SL\alpha$$

The force and moment is reduced to coefficient form in the following manner

$$C_f = \frac{F_Y}{qS}$$

$$C_T = \frac{M_Y}{qSD}$$

and sign conventions are defined on Figure 5-4 but may be summarised as:-

Pitch positive nose-up
Rotation positive clockwise when viewed from the rear.
Force positive to the left when viewed from the rear.
Moment positive counterclockwise when viewed from above.

These results were for a laminar boundary layer and therefore have limited application. The same approach was used by Kelly and Thacker[11], who introduced higher-order approximations and arrived at a similar result for low spin rates, but a quadratic form of the C_f - pD/2V curve at higher spin rates. In fact, they appear to predict a sign change in the Magnus force at approximately pD/2V = 0.1. Extensions of this kind of solution were pursued by Sedney[12], for the compressible case, and Jacobsen, Vollmer and Morton[13] for the incompressible flow over a cone. In these boundary layer theories with no allowance for separation the Magnus force varies linearly with incidence.

The large angle of attack case has been tackled by Power and Iversen[14], who have taken into account the circulation due to lee-side boundary layer separation by adding it to the potential flow field. Centrifugal force in the boundary layer and skin friction has also been covered in their treatment, which predicts a Magnus force which varies non-linearly with angle of attack even at low angles, in the manner of the data shown by Green[15]. All these theories have as their basis some simple assumption of the way in which the boundary layer develops along the body length. No account is taken of the effect of the base shape, which, as will be shown in the data below, plays a large part in the production of the Magnus force.

5.4 A BRIEF REVIEW OF CONVENTIONAL MEASUREMENT TECHNIQUES

The main source of Magnus data is from wind tunnel facilities. The most frequently used method of force measurement is the strain-gauge balance, which is usually fitted within the body of the model to be tested, at the end of the sting support. An air bearing and air turbine are usually combined inside the base end of the model to provide the rotation. Although the mass flow rate used by these air turbines is quite small, one cannot rule out the possibility that flow interference might result from the ejection of air at the base. The effect of the sting itself cannot, of course, be removed. Normally, to prevent excessive vibration, the sting diameter is at least 20% of the diameter of the base. For large models, dynamic balancing is important.

The second source of data is from the free-flight techniques, such as range firings. Here, the Magnus forces are estimated from the data after this has been fitted to a quasi-linear mathematical model of the motion, along with the other aerodynamic coefficients. Errors are usually large because of the lack of data points, and the interdependence of the aerodynamic forces. In addition, the validity of the assumed aerodynamic characteristics applies over only a limited range of angles of attack, etc., and the projectile normally executes oscillatory and coning motions through a wide range of angles.

A method used with some success by Nicolaides, et al[7] employs a single point suspension for the model, which is flown in a wind tunnel normally with small canted fins at the nose or base to impart spin. The measurement of the Magnus force is indirect, and follows a similar pattern to the analysis of firing-range data. This naturally suffers from the limitations imposed by the assumptions made for the aerodynamic characteristics, as with the spark-range methods,

Magnetic suspension, however, provides a near free-flight situation but with the advantages of direct measurement, and would thus appear to be the ideal system for Magnus testing. The particular balance used had the single drawback of providing a relatively low Reynolds number owing to the small size of the test section and hence model.

6. DEVELOPMENT OF EQUIPMENT FOR THE MAGNUS MEASUREMENTS

6.1 Introduction

Two different methods for the measurement of Magnus forces on the 7-calibre body of revolution were considered: (i) to maintain the position and attitude of the spinning model fixed, and deduce forces and moments from the variations in the electromagnet control currents (ii) to generate a very low suspension stiffness in the horizontal plane, and allow the model to move under the action of the Magnus force, calculating the magnitude of this force from the lateral displacement. The first method is the one normally employed for steady aerodynamic testing, as discussed in Chapter 3, and was the one eventually used to produce the Magnus data presented in this report. Method (ii), however, was worthy of consideration because of the need for high sensitivity, the estimated size of the Magnus forces being of the order of a few grams at the air speeds and spin rates considered feasible. A circuit was developed which provided a high damping ratio for lateral heaving motions of the model, but very low stiffness, the intention being to utilise for stability the small positive stiffness in the horizontal plane generated by the combined fields of the vertical and lateral coils*. The idea was dropped for a number of reasons: the lateral stiffness was a function of the lift, drag and pitching moment in the vertical plane, thus these forces would have to enter into the calculation of Magnus force; Magnus moment could not be measured; the yaw angle of the model would have to be maintained zero when heave movement is present, requiring the use of position-sensors with a very high linearity.

Various devices were developed for imparting spin to the model. In all cases the method was aerodynamic, although there is no reason, in principle, why an electromagnet method should not be used, as in the tests conducted by Haldeman, Coffin, et al at M.I.T.[16].

---

*From Maxwell's equations: div $\underline{B} = 0$, therefore the sum of the magnetic field gradients in a horizontal plane beneath one of the vertical suspension pole faces is equal and opposite to the vertical field gradient existing perpendicular to that plane. Thus, the negative stiffness in the vertical direction must be complemented by a positive stiffness in the lateral and/or axial directions. In practice both are positive. The magnitude of the gradients are dependent on the strength of the vertical field, and thus on the lift forces exerted on the suspended model. However, the lateral stiffness may be reduced to a small positive value by suitably strong fields generated by the lateral coils.

Initially, a rig using a turbine driven by the tunnel flow was constructed, utilising a support built for earlier sting-interference tests.[1] A small eight-blade turbine was brought into contact with the base of the model by a pneumatic piston. A spigot located the base centrally, and a rubber ring provided the required friction between the two. The force of attraction and hence the friction between model and turbine could be varied by changing the current through a small coil behind the turbine. With the tunnel flow started and the model spinning, the pneumatic cylinder could be actuated to retract the turbine to a distance of 15 cm from the model base. Spin-up had to be carried out at a zero pitch incidence and therefore an electronic circuit was developed to sweep the incidence automatically to a preset value, where secondary position sensors took control.

The mechanical constraint imposed by this particular rig on the motion of the base end of the model limited the spin rate that could be achieved to 5,500 r.p.m. Beyond this spin rate, instability usually resulted in loss of control, and the model came out of suspension. The spin rate available from the turbine was proportional to tunnel air speed, with a constant of proportionality of 250 r.p.m. per metre/second.

A second device, used for the tests previously reported[17] comprised two small air jets, one on each side of the model, each directing a jet of compressed air along a tangent to the surface. The aperture of each jet measured 3 mm x 0.7 mm and each was set 0.75 mm away from the surface of the model. Both jets were fed through flexible tubing from a nominal 75 p.s.i., compressed air line, the same air line which was used to operate the pneumatic retraction mechanism. With this device, the model could be spun at incidence without difficulty, and without the need for running the tunnel. The problems of unsteadiness arising from the mechanical connection of the first device were eliminated entirely; in fact, wobbling at the base end of the model amounting to ± 0.75 mm in the lateral direction and ± 2.5 mm in the vertical direction could be tolerated during the spin-up period. This device proved capable of imparting rotational speeds of up to 400 revolutions/second (24,000 r.p.m.) to the model. The air jets were retractable to a position 70 mm from the rear end of the model, the pneumatic retraction cylinder being the same as that used with the turbine rig. The direction of rotation was clockwise, looking upstream.

Exactly the same principle was used in the final design for the spinner described in this report, the only differences being in the construction of the retraction mechanism, in the provision of an extra pair of jets to enable spinning in both directions and a slight increase in jet size.

It must be noted that in all cases the function of the spinning device was to drive the model to as high a rotational velocity as possible before the measurements were begun. The natural decay of the spin rate under the influence of skin frictional forces and eddy-current braking was exploited to provide continuous Magnus data versus spin rate.

For the measurement of the spin rate of the model, an optical system was devised. The original version[17] has been improved as discussed in section 6.5 of this chapter.

Side force can have two components, the Magnus force and a force due to yaw angle. On the asusmption that these forces are additive they can be separated because the Magnus component is a function of spin rate whereas the other is not. The Magnus force is therefore taken to be that side force component which varies with spin rate. In order to minimise any error due to the assumption, an accuracy of 0.1^{o} in set yaw angle was aimed at, with a maximum variation of $\pm\ 0.02^{o}$ in this angle over the period of a test run.

6.2 Precision optical position sensing

To satisfy the above-mentioned need for accuracy in yaw angle, a secondary optical position-sensing system was developed for the lateral control circuits, using improved light sources and miniature photovoltaic cells. Figures 6.1 and 6.2 show the arrangements for detecting the position of each end of the body of revolution.

The light sources developed for this application used a linear filament 10-watt bulb (General Electric, type GE-1922) at the focus of a 2-element achromatic objective (Dallmeyer, type A). The normal operating voltage of the bulbs is 4.0 volts, but in order to increase their lifetime and reliability they were fed with 3.0V, stabilised at the bulb by feedback to the power supply. The supply voltage was maintained

within ± 0.1% to 3.00 volts. The light sources were mounted so that, when in use, the filaments of the bulbs were parallel to the centre line of the wind tunnel, and thus parallel to the edge of the cylindrical portion of the test model. In this way, sharp shadows could be produced for use with the miniature photocells.

Because of the deployment of the electromagnet array around the working section, it was necessary to mount sources and photocells beneath the lower glass wall of the tunnel. A system of vertical beams was chosen because of the need for constant yaw angle over a range of pitch incidences. There was also the need to provide a main sensor for axial motions of the model. The base of the body, often used in the past, was not a feasible reference edge because of the obstruction caused by the spin-up device, and because several different base geometries were to be tested.

The solution, shown in Figs. 6.1 and 6.2, employed a pair of front surfaced mirrors canted at 4.5° in an aluminium housing in the roof of the test section. A piece of 6mm thick toughened glass preserved the flatness of the roof and protected the surfaces of the mirrors from dust. The beams from the light sources, mounted on the base-plate at an angle of 9.0°, were reflected vertically downwards one across the nose and one near to the rear of the model. The rear sensor was a 1mm x 2mm silicon photovoltaic cell mounted on a vernier, whose position could be read to ± 0.1 mm. At the nose a main sensor, of the kind used for coarse detection of the lateral and vertical position of the body, was mounted with the slot (3mm x 30mm) transverse to the tunnel axis. Two 1mm x 2mm sensors were used, one monitoring each side of the shadow of the nose. Unlike the rear sensor, they were clamped in position. The distance from the rear cell to the centre of the nose sensor was 125 mm, thus a movement of 1 mm of the rear coil vernier was equivalent to a change of 0.46° in yaw. The variation in output voltage of the rear cell (amplifier) as the cell was tracked across the shadow edge is shown in Fig. 6.3. The slope where the cell is 50% illuminated is 0.27 volts/mm, i.e. 0.59 volts/degree of yaw. Thus to satisfy the $\pm 0.02^{\circ}$ requirement for yaw accuracy a drift of 12 mV in the output can be tolerated. In practice, this is fairly easy to attain over a short period (1-2 hours) with low-cost amplifiers. Occasional day-to-day drifts

of 50 mV could occur, but this represented a change in absolute yaw angle of only 0.085^{o}, which was still within the specifications. A summary of the accuracy of position control in the lateral plane is given in Table 6.1.

As discussed in Chapter 2, the purpose of the secondary position sensors is to feed integrators whose outputs are added into the main control loops. The circuit diagrams for one of the integral controls are shown in Fig. 6.4. The integral of the signal representing lateral motions of the nose, i.e. the difference between the outputs of the two nose sensors, is added at the input of the amplifier driving the forward lateral thyristor supply. The integral of the rear position signal is added at the input of the aft lateral power supply. Therefore, the effect is to maintain both yaw and lateral position to a high precision.

TABLE 6.1

Maximum errors in attitude and position of the model owing to drift and noise in the lateral control loops

	Drift		Noise
	Long-term	Short-term	
Lateral position	± 0.2 mm	± 0.04 mm	± 0.02 mm
Yaw	$\pm 0.1^{o}$	$\pm 0.02^{o}$	$\pm 0.02^{o}$

6.3 Measurement of the pitch angle

For the measurement of pitch, the main optical position sensors were found to be adequate. Integrators for the vertical heave and pitch control loops were both fed from the main sensor position signals. This was adequate because the accuracy requirements for the vertical degrees of freedom were less severe. The effect on the side force of altering the pitch angle by, say, 1^{o} is more than one order of magnitude less than the effect of a similar change in the yaw angle, owing to the relative sizes of the Magnus and lift force coefficients.

Pitch angles could be set to an accuracy of 0.1^{o}, and the estimated drift over the period of one test run was less than 0.05^{o}. During the spin down of the model, small amplitude fluctuations of pitch angle and vertical position were observed as a result of the interaction between the off-axis components of magnetisation in the model magnet, and the suspension fields (described more fully in section 6.6.2). The maximum deviation from the mean angle of pitch, which was maintained within 0.05^{o} of its preset value by the integral feedback, amounted to $\pm 0.2^{o}$ at worst, and over the greater part of the test run was less than $\pm 0.1^{o}$. Steadiness in pitch angle and vertical position at zero spin rate was limited only by noise in the control circuits. Values measured with the aid of a travelling microscope were: $\pm$ 0.05 mm for the vertical position and $\pm 0.05^{o}$ for the pitch angle.

Calibration of the pitch position signal against the true angle was accomplished using a specially designed rig.* The model was held in a vee-block of brass which was pivoted inside an aluminium frame to allow only pitching motion. The frame could be slid inside the working section of the tunnel and fixed by bolts at a set position. A small front-surfaced mirror was fitted to the vee-block so that its reflecting surface was touching the line joining the pivots. A beam of light from a 1mW laser was directed onto the mirror by a second mirror fixed outside the working section. (The portion of the wind tunnel between the working section and the injector was removed to carry out the calibration.) The reflected beam produced a spot of light on a vertical scale, calibrated in half-degree intervals from -3^{o} to $+ 18^{o}$. The position of the graduations was calculated from the geometry and dimensions of the arrangement. The position of the zero was adjustable over a small range by adjusting the scale up or down over a few centimetres.

Calibration was accomplished in the following way. The model was fitted in the block and the attitude set at nominal zero degrees by placing the end of a lever arm of angle aluminium (fixed to the block) a certain distance above the floor of the working section. This distance was measured with a length of brass rod machined to the required length; the precise length was calculated to be that which would set the axis of the model along the centre line of the wind tunnel

* See Fig. 6-5

and was approximately 9.14 cm. With the model set at nominal zero degrees in pitch, the zero offset potentiometers in the vertical position-sensing amplifiers were zero trimmed. The scale was then adjusted so that the light spot fell on the 0^{o} graduation. The model was pitched manually and the output of the pitch position signal plotted against the incidence shown on the scale. A typical incidence calibration is shown in Fig. 6.6 Long-term drift in calibration slopes amounted to ± 0.5% in general; drift in the zero was the aspect needing most attention. The zero setting was checked before each series of test runs.

6.4 The spinning device

As already stated in section 6.1, the spinning equipment finally used for the Magnus tests is an improved version of the air-jet rig described in a previous report[17]. Angular velocity is imparted to the model by directing a pair of air jets at a tangent to the surface of the cylindrical afterbody generating torque by the effect of skin friction. The maximum spin rate available is limited by the velocity of the air jets, the surface condition of the model where the jets impinge and the aerodynamic and electromagnetic damping existing in the system. The surface condition of the model could not be altered (i.e. roughened) to increase the torque without disturbing the Magnus characteristics of the body; however, rotational speeds in excess of 450 revolutions/second could be attained with the smooth model, which was adequate for the range of tests contemplated.

The design of the jet block is illustrated in Fig. 6.7, and it can be seen that each of the four jets is fed from a separate flexible nylon tube. The aperture of each of the jets is rectangular and measures approximately 5mm x 1.5mm. The block was machined from a single piece of stainless steel chosen for its low magnetic relative permeability, so as not exert unwanted forces on the base end of the model.

The block slides on two stainless steel rods which form the final part of the retraction mechanism. The block can be clamped on the rods in any desired vertical position by means of two brass bolts, so that all pitch incidences of the model can be accommodated.

The retraction mechanism itself was designed to fit into the confined space beneath the downstream floor of the working section. It was designed to withdraw the jet block entirely from the air stream in the working section, since there was a possibility that the original pneumatic retracter, which allowed the air jets to remain only 70 mm behind the base of the model during a test, had caused flow interference. The retracter was required to pass through an aperture in the floor of the working section, immediately downstream of the glass window. The aperture measured 92 mm in the streamwise direction. The size of the box into which the mechanism was to retract was limited to 180 x 185 x 76 mm (outside dimensions) to avoid interference with position-sensors and tunnel supports. The speed of retraction had to be as high as possible, in order to make use of the highest spin rates. A door had to be fitted that would close rapidly after the mechanism had been retracted and leave the floor of the working section flat, so as not to disturb the air flow.

To meet these requirements, the design shown in Fig. 6.8 was evolved.* The mechanism is a two-stage device operated by small pneumatic actuators. The operation of retraction and closing of the wind tunnel doors is controlled by a single valve, and takes place in approximately 2 seconds.

The upper section folds the stainless steel rods holding the jet block back through 90°. The actuator is a ½-inch (12.7 mm) bore double-acting cylinder, Schrader type S448, and is fed by ⅛-inch (3.2 mm) O.D. nylon tube through connectors in the main box. The tubes carrying compressed air to the jets are of ¼-inch (6.4 mm) O.D. PVC in this region to avoid the 'kinking' problems that would occur with nylon tubing bent through a sharp angle. The mechanism to produce a rotation from the linear motion provided by the actuator was a slot and cam arrangement.

The lower section, whose purpose was to act as a mounting for the upper section was constructed from aluminium alloy, and was pivoted about two simple brass bearings in the sides of the box a short distance below the glass window of the test section. A simple arrangement of clamps allowed adjustment and fixing of the position of the upper part relative to the lower. The actuator was a ¾-inch (19.1 mm) bore double-acting cylinder, Schrader type S.468, mounted through a hole in the upstream end of the box. Again, a slot-and-roller method was used

* Photographs of the mechanism also appear in Figs. 6.15(a) - (d).

to produce the rotary motion. Because of the weight of the mechanism the rollers for the lower section were fixed to a brass block sliding on a pair of ¼-inch (6.4 mm) stainless steel rods. The piston rod of the ¾-inch cylinder was then screwed into this, thus relieving the piston rod of most of the sideways force.

The automatic sequence was begun by a manual change-over valve connected to the main ¾-inch cylinder.* As soon as the lower section began to retract, a micro-switch was operated which cut off the current supply to a solenoid valve. This operated a change-over valve feeding the small cylinder on the upper section, and folded back the jet block. The speed of retraction of each cylinder could be adjusted by means of restrictors fitted to each change-over valve, and the upper cylinder was set to fold down as quickly as possible so that the device could clear the door opening. When fully retracted, a bracket attached to the piston of the ¾-inch cylinder actuated a plunger-operated poppet valve. This, in turn, switched on a pilot-operated change-over valve connected to a small ½-inch cylinder which closed the doors.

The compressed air to the jets was supplied from feed-through connectors on the aluminium box to the lower part of the retracter via nylon tubing. The tubing required replacing occasionally, as it was difficult to avoid kinks in the tubes. The external selection of the pair of jets required for clockwise or anti-clockwise rotation was by means of a manual 3-way valve. The feed to the valve was through ⅜-inch (9.5 mm) O.D. nylon tubing from the 75 p.s.i. supply line. The alternate of a change-over valve was not chosen as a selector because of the extra resistance it offered to the air flow; maximum velocity at the jets was required in order to gain maximum spin rate of the model.

The highest spin rate normally attained was 420 revolutions/second (25,200 r.p.m.). The spin-up time from rest was usually 2-3 minutes. The shape of the base did not significantly affect the maximum speed, 400 r.p.m. being attainable with the 10-degree 1-calibre boattail base and cavity bases despite the increased distance between the jets and the point of impingement. Slightly higher spin rates were attainable at 0° pitch incidence than at the highest incidence used, i.e. 7.0°.

* A schematic diagram of the pneumatic circuit is shown in Fig. 6-9.

6.5 The Tachometer

Two versions will be described. The first was used for the preliminary Magnus measurements[17]; the second for the more comprehensive measurements on the 9 base configurations [22]. An optical method was chosen, as the use of a magnetic system would have required the model to possess an additional magnetic moment aligned perpendicular to its rotation axis. Off-axis components of magnetisation were undesirable, as they appear to be responsible for the reduction in stability of the model at certain spin rates (see section 6.6.2).

6.5.1 Preliminary Version

The first tachometer was based on a 'Radiospares' light-actuated switch, type LAS 15, incorporating photodiode and switching circuit on one integrated circuit (IC). The output of the device was compatible with general-purpose 5 volt transistor-transistor logic (TTL). The IC was placed at the focus of a simple lens of 20 mm aperture and located beneath the lower glass wall of the test section. Light reflected from the model was directed into the sensor by a small plane mirror, whose angle could be manually adjusted. The model was illuminated from below by a light source, fed from a variable voltage supply.

One half of the test model was sprayed with matt black paint. The other side was left unpainted. It was found in practice that an unpainted perspex model containing a ground Alcomax magnet reflected more light than one with a white surface.

At an early stage, the LAS 15 was found to be sluggish in response to light fluctuations at frequencies above approximately 100 Hz, even with the highest available illumination of the model. It was therefore replaced by a BPX 25 phototransistor and amplifier.

The amplitude-limited pulses from the amplifier were applied to two SN7490's in series. The circuit therefore made available pulses occurring every 1, 10, or 100 rotations of the model. Spin rate information was recorded on one channel of a 4-channel chart recorder during test runs, the other channels carrying force and moment information. The spin rate of the model at any point on the recording was calculated by counting the number of pulses in a known time at the point.

6.5.2 Final Version

The rotational speed measuring equipment was built in two units: the optical sensor and pulse amplifier; and the frequency-to-voltage converter. To sense the rotation a spot on the lower side of the model was illuminated by a beam from a light source consisting of a 6V 6W bulb and 25 mm f2 lens. The receiver consisted of a 20 mm f3 lens and phototransistor (BPX 25). Both were mounted below the glass window forming the floor of the working section and were adjustable.

The whole of the model was sprayed with matt black paint, with the exception of the central part of the body, where five segments were left clear at 72° intervals around the model. Both the inside and the outside of the perspex were polished at this point to allow reflection from the Alcomax magnet (see section 6.6). One rotation of the model therefore produced five flashes of light at the receiver.

There were two reasons for choosing more than one clear segment on the model for the detection of rotation. The first was that a single flash of light per rotation might give rise to interference in the control loops in the form of synchronous pulses, since it proved difficult to prevent the reflected light from reaching the position sensors. The second was that a higher frequency pulse train would be easier to 'smooth out' in the frequency-to-voltage converter. Five segments was the practical maximum number, each segment being 7mm wide, approximately the same as the width of the light spot.

The pulse amplifier is shown in Fig. 6.10 A general-purpose operational amplifier acts as an amplifier/limiter and delivers a train of square wave pulses to the base of TR2. It also provides an output for monitoring on an oscilloscope, and drives TTL dividers (not shown) which can be used to produce one pulse per 5, 10, or 100 input pulses. TR2 produces sharper-edged pulses for differentiation by the 820 pF capacitor and 39k resistor. The pulses are amplified and inverted by TR3. The final output is a train of negative pulses of approximately 50μs duration and -15 volts amplitude.

The frequency-voltage converter is contained in a separate unit and is a high-performance monostable multivibrator followed by an integration network. The monostable is built around three operational amplifiers and provides a wide range of pulse width adjustment and

very flat, well-controlled output pulses. The pulse width is adjustable from 30-150μs, and the rise time, limited by the slew rate of the 741 operational amplifiers, is 20μs. During the pulses, the output drops from + 8 volts to -8 volts.

A simple averaging filter forms the final stage of the unit. The time constant chosen (0.47 sec) is a compromise between speed of response and percentage ripple reduction. The output is linear with frequency over the range required, to better than 0.5%

The unit was normally run with a digital frequency meter connected to the output of amplifier A1, so that a continuous check was available on the calibration. The pulse width adjustment on the converter was set so that a frequency of 1kHz produced an output voltage of 1.00 volts. The actual spin rate of the model is, of course, 200 r.p.s. at this frequency.

Setting up the tachometer involved adjusting the brightness of the light-source and the setting of the zero adjust potentiometer VR1 to produce good square waves at the monitoring point. Readjustment was normally necessary for each pitch incidence of the model, as this affected the intensity of the reflected light.

6.6 Model development

6.6.1 Mass and moments of inertia

Static aerodynamic tests are normally carried out on aluminium models, with perhaps some of the internal parts manufactured in a heavier material, such as brass. The overall mass of a model of the 7-calibre AN spinner constructed in this way was typically 250 grams. There are two effects of the mass on the suspension system; firstly, the electromagnet currents required to hold the model in suspension are directly proportional to the weight. Therefore the power dissipation in the vertical coils is increased as the square of the mass. Secondly, the dynamics of the suspension are altered, usually improving with increase of the mass.

The moment of inertia perpendicular to the axis of the model influences the dynamics in the pitching mode of control, and it has been found that an increase in moment of inertia results in a greater margin of stability.

In addition, in order to prolong the spin-down time in the Magnus tests, the principal moment of inertia should be as high as possible. In fact, these considerations were secondary in importance to the requirement for low electromagnetic damping, which was the factor influencing the choice of material for the model (see Section 6.6.3).

6.6.2 Magnetic properties

The choice of magnet material for the core was straightforward. The standard material used with the University of Southampton Magnetic Suspension system is Alcomax III, which has the properties shown in Table 6.2.

TABLE 6.2

Magnetic properties of Alcomax III

Remanence B_r	Maximum energy-product $(BH)_{max}$	Coercivity H_c	Density ρ
1.26 Tesla	43 kJ/m^3	52 kA/m	7.35 g/cm^3

The material is an anisotropic alloy which is cast in standard sizes, and is machinable only by grinding. The size used for the test model was nominally 4-inches x 0.625 inches diameter (actual measurements 101 mm x 15.9 mm dia.).

The material is produced with its preferred axis of magnetisation aligned with the geometrical axis, or nearly so. There always exist small magnetic moments perpendicular to the axis, however, and measurements of the variation of pole strength around the ends of the magnet made with a Hall-effect probe bear this out. In static testing, the effect of these off-axis components is to cause the model to hold, or execute lightly damped oscillations about, a preferred roll orientation. This can be an advantage in static testing, in that rolling of the model is prevented; but in Magnus measurements, the interaction between these components of magnetisation and the field gradients can lead to instability.

Considering one end of the magnet, any dipole moment existing perpendicular to the axis will cause a force to be exerted in the direction of the magnetic field gradient at the pole, its amplitude depending on the angle. The force vector is given by

$$\underline{F} = \underline{\nabla}(\underline{m}.\underline{B}) = (\underline{m}.\underline{\nabla})\underline{B} = m \frac{\partial B}{\partial z} \cos \gamma,$$

if the field gradient is assumed to lie in the z direction. A similar situation will exist at the other pole of the magnet, but the directions of the dipole moments will not necessarily be parallel at each end. The reuslt, as the model rotates, will be fluctuating force in the lift direction, and a fluctuating pitching moment, both in synchronisation with the rotation of the model.

With a steady magnetic field, the effect would add a small perturbation to the model which would become less obvious as the spin rate was increased. However, the coils of the suspension system are driven by thyristor amplifiers, which produce only a quasi-DC current. The time-constant of the coil system is high enough to allow a significant AC component at the fundamental 150 Hz to pass. Other frequency components also exist in the system because of imperfections in the thyristor supplies, i.e. 50 Hz, 100 Hz, 150 Hz, 300 Hz. As the spin rate of the model passes through one of these frequencies, a resonance effect is produced. At rotational rates exactly equal to the frequency of the field fluctuations, the force and torque assume steady values, producing a noticeable shift in the position of the model. Strong gyroscopic effects exist with the spinning model, which may have affected stability through coupling.

Elimination of this effect could be achieved in two ways: by using a magnet with a truly axial magnetisation; and by replacing the thyristor supplies with transistor DC amplifiers. A batch of similar magnets exhibited the same asymmetry in magnetic properties. The situation had therefore to be tolerated, as the wobbling did not have a greatly detrimental effect on the Magnus data. The small fluctuation in the Magnus force coefficient at 150 Hz can just be seen in some of the test records.

It is worth noting that similar problems have been found with the system at Massachusetts Institute of Technology[16], where the magnetic core is a ferromagnetic material.

6.6.3 Electromagnetic spin damping

At an early stage it was decided to use Perspex acrylic plastic as the main material for the model envelope. Tests with an all-Aluminium model using the earliest spinning device gave deceleration rates of approximately 3.5 revs sec^{-2} at 2600 r,p.m. By making the cylindrical portion of the body of the Perspex non-conducting material the figure was redcued to 0.9 revs sec^{-2}. For earlier tests[17], the base of the model was of brass, but the remainder, excluding the magnet, was of Perspex. The further reduction in deceleration allowed meaningful measurements to be carried out.

A cross-section through the model is shown in Fig. 6.11. The design of the rear allows simple changes of base shape. The permanent magnet provided the only conducting part of the model, and thus the only part contributing to the eddy-current damping. The resistivity of Alcomax III was measured to be $\sim 4 \times 10^{-7}$ metre-ohms. This is usefully higher than that of aluminium (0.28×10^{-7}) and brass (0.71×10^{-7}).

An appropriate equation for the torque acting on a spinning cylinder in a uniform magnetic field can be written:

$$T = \tfrac{1}{4}\pi B^2 \ell^2 r^4 p\sigma$$

where B = magnetic induction, ℓ = length of cylinder, r = radius of cylinder, σ = conductivity of cylinder (σ = 1/resistivity), p = angular velocity. The acceleration is

$$\dot{p} = -T/I_3$$

where I_3 = principal moment of inertia of the cylinder. Therefore the spin rate decays exponentially with a time constant

$$\tau = I_3/(\tfrac{1}{4}\pi B^2 \ell^2 r^4 \sigma)$$

Considering the magnet alone, the principal moment of inertia is

$$I_3 = \tfrac{1}{2}\pi r^4 \ell \rho$$

where ρ = the density of Alcomax III. The decay time constant therefore becomes

$$\tau = 2\rho/B^2 \ell \sigma$$

For a given magnet material, the magnetisation will be proportional to the volume, as will be the weight of the magnet. The field strength required to suspend the magnet alone is therefore independent of the radius; B can thus be considered roughly constant in the above equation. The decay time constant is therefore independent of the magnet radius, and can only be increased by increasing the part of the moment of inertia due to the outer Perspex shell. Perspex, is a low density material, but has the advantage of being easy to machine. The time constant with this combination of materials in practice proved long enough for measurements to be taken by the rapid method of FM tape-recording (see Chapter 7). Therefore other shell materials were not sought.

6.6.4 Interchangeable bases

For simplicity, the design of the rear end of the Perspex model was made to accommodate the 9 separate case configurations demanded by the contract. The overall length of the model (7 calibres) was constant in all cases. Sections through the bases are illustrated in Fig. 6.12, and a photograph of the model and bases is shown in Fig. 6.16.

6.6.5 Boundary layer tripping

Flow conditions were required to be close to those of free-flight. In the normal free flight testing (range-firing) of ballistic shapes the Reynolds number is sufficiently high to produce a turbulent boundary layer over the greater part of the projectile. A laminar boundary layer probably persists over the front section of the nose. For the 22mm diameter model used for this wind tunnel testing, the length-based Reynolds number is related to the free stream velocity in the following way:

$$Re_L = 0.0107V \times 10^6,$$

when V is given in metres per second. In the present series of tests the flow velocity has been within the range 50-75 metres/sec. The lower velocities were employed for the measurements with a smooth model. Because transition Reynolds numbers can range up to 2×10^6 depending on surface and flow conditions, it can be seen that with no roughness elements the boundary layer could remain laminar over most of the length of the model. For this reason, boundary layer tripping was used to induce transition near the nose.

The material for the roughness elements was silicon carbide grit (Carborundum) , which was available in a range of sizes and for which data on grain size distribution existed. The grains were held in place at 1.5 calibres from the apex of the nose by a water-based adhesive ('Polaroid' fixer was found to be eminently suitable) which was applied in a band approximately 5mm wide (0.25 calibres). To distribute the grains in an even manner over the band, they were first spread uniformly on a sheet of card; the model could then be rolled over the card with slight pressure to fix the particles in place. This method was probably selective, in that large grains were more likely to adhere to the model.

Calculation of the roughness size was based on results obtained by Fage and Preston and quoted by Schlichting[18], The minimum height k_{cr} for which transition occurs at the roughness element itself can be found from the relation

$$u_\tau k_{cr}/\nu = 20$$

where $u_\tau = \sqrt{\tau_w/\rho}$ is the friction velocity, and τ_w is the wall shear stress at the wall in the laminar boundary layer at the position of the roughness element. The wall shear stress for the laminar boundary layer on a flat plate at a distance x from the leading edge is

$$\tau_w(x) = 0.332\ \rho V^2/Re_x^{\frac{1}{2}}$$

and can be expected to exceed this value for the same point on the ogive nose of the model owing to the positive pressure gradient, which will reduce the displacement thickness. With these substitutions the expression for k_{cr} can be written:

$$k_{cr} \leq 35.0 \times Re_x^{-0.75}$$

Using a typical value for the Reynolds number 1.5 calibres from the nose, viz 1.6×10^5, the roughness height becomes

$$k_{cr} = 0.14 \text{ mm}$$

TABLE 6.3

Percentage of size 100 carborundum grains greater than specified diameter

percent	diam. (mm)
0%	0.211
15%	0.150
40%	0.124
65%	0.104
97%	0.074

The grit size chosen was number 100. Details of the size distribution are given in Table 6.3. If the selective properties of the application method are taken into account, the mean size of the particles adhering to the model will lie in the range 0.12 - 0.15mm.

To establish that size 100 grit at 1.5 calibres from the apex was effective in producing a turbulent boundary layer, measurements of the drag coefficient of the 7-calibre basic spinner were performed over a range of Reynolds numbers with, and without, the roughness band. The results are exhibited in Fig. 6.13. The progression of the drag coefficient of the 'clean' model from $\sim$ 0.2 at $Re_L = 3 \times 10^5$ to 0.23 at $Re_L = 7 \times 10^5$ indicates the movement of the transition line upstream from the base. Even at the highest Reynolds numbers the value is noticeably less than that of the 'roughened' model, so that it is likely that the boundary layer remains laminar along some of the cylindrical body. In contrast, the drag of the 'tripped' model undergoes a fairly rapid increase around $Re = 3.5 \times 10^5$ and remains substantially constant from 4×10^5 to 7×10^5 at approximately 0.25 but with indications that it would begin to fall with further increase in Reynolds number. A good indication that the grit has negligible pressure drag is the agreement between drag coefficients with and without grit at low Reynolds number.

Finally, calculation of the boundary layer displacement thickness δ^* for a flat plate at 1.5 calibres (33 mm) from the leading edge and a Reynolds number of 1.6×10^5 gives

$$\delta^* = 0.142 \text{ mm.}$$

which is very close to the value for the required roughness size. The true displacement thickness is somewhat less than this, because of

the pressure gradient existing over the nose, so that the roughness size probably exceeds δ^*. There is good reason to believe that any further increase in roughness size is unnecessary, as data compiled by Dryden (also quoted in Schlichting[18]) indicates that the point of transition has moved up to the roughness element when the grit size equals δ^*. This confirms the previously quoted criterion due to Fage and Preston.

6.7 Current signal amplification and filtering

The measurement of force and moment in the horizontal plane relies upon the accurate measurement of the currents flowing in the lateral electromagnets. The normal practice is to amplify the voltages across the meter shunt resistors to a level where detection of small changes becomes possible with a digital voltmeter. The value of the shunt resistances is approximately 0.004 ohms, and in order to detect the required changes in the suspension currents, of the order of 0.1 amps, considerable amplification is needed.

The side force produced by the lateral electromagnets is a function of 3 separate power supplies, as indicated in figure 2.1. During early Magnus force tests, it was found that erratic step-like variations were occurring in the lateral control currents. The source of these 'jumps' was traced to spurious changed in the lateral bias current of the order of 0.1 amps. With integral feedback in operation, changes in bias current level did not affect the model position, except for a transient motion in yaw, since the lateral control circuits adjusted the control currents to compensate. As bias and control windings of the lateral suspension coils were similar, changes in bias current produced nearly equal complementary changes in the fore and aft control currents.

It was therefore decided to subtract a signal proportional to bias current from the lateral current signals, and thus eliminate the effect. This was accomplished by incorporating a summing amplifier in the current signal amplification circuits, one of which is shown in Fig. 6-14.

Despite the relatively long time-constant of the magnet coil - load resistor combination (approximately 0.03 sec) an unacceptable proportion of AC ripple remains on the current signal at the meter shunt. Filtering was essential for an adequate signal-to-noise ratio, and since the frequency range of interest for the Magnus force measurements was quite low, heavy low-pass filtering was introduced. The choice of the dominant time-constant of the amplifier was influenced by the time-constant of the spin decay (>30 seconds); it was decided to limit to 1% the error due to the time-lag of the filter during the spin rate decay. It was also preferable to make the time constants of the tachometer and current signal amplifiers approximately the same, to minimise errors due to group delay differences between the spin rate and current signal channels. These considerations led to the selection of 0.33 sec as the filter time constant.

7. MAGNUS DATA ACQUISITION AND ANALYSIS

7.1 Introduction

This chapter will describe the methods by which the Magnus force and moment data were acquired from the suspension system. The greater part of the chapter will be devoted to the method finally developed and used for the 9 base configurations of the 7-calibre AN spinner. This technique, described in section 7.3, yielded the largest quantity of data, and represented a refinement of the method of section 7.2.

7.2 First Technique

7.2.1 Experimental Arrangement

The first method of Magnus force and moment measurement was used in conjunction with the first air-jet spinning device[17](see section 6.1). The current signal amplification circuits have been described in section 6.7. The amplified signals were applied directly to the inputs of a 4-channel chart recorder having a rapid response time. Pulses from the tachometer described in section 6.5.1 were applied to a third channel. The chart speed was chosen such that individual tachometer pulses were distinguishable at the maximum spin rate. Usually, the tachometer output giving one pulse per 10 revolutions of the model was employed, although for low chart speeds the 'divide by 100' output could be used.

7.2.2 Test Procedure

Each test run was preceded by two setting-up operations: one to adjust the tachometer, which required re-setting each time the pitch incidence was changed; and one to set the zero level of the current signal amplifiers. The model was set at nominal zero incidence in the horizontal plane, but in practice possessed a residual yaw angle, giving rise to a small side force with wind on. The tunnel was therefore run with the model stationary at the air speed to be used in the ensuing Magnus force test. Zero adjustments were then made to bring the penrecorder traces on to the chart.

The test sequence was as follows:

(i) Model placed in magnetic suspension. Attitude set. Integral feedback switched in.

(ii) Position of air jets adjusted manually until approximately equidistant from surface and on diametrically opposed sides of the model. Axial position of jets approximately 5 mm upstream of the base.

(iii) Compressed air turned on. Rotational speed of model allowed to increase to 400 revolutions/sec. Tachometer zero-adjust set (see Fig. 6.10) so that a stable square wave output was obtained, as displayed on an oscilloscope.

(iv) With the model at rest and the air-jet spinner retracted, the tunnel was run at testing speed and penrecorder adjustments carried out to bring the traces on to the chart.

(v) Air-jets set close to the base as before and turned on. Spin rate allowed to rise to 400 revs/sec.

(vi) Chart recorder started with a chart speed of 5 or 2.5 cm/sec. Air jets retracted. Tunnel flow brought up to testing speed. These operations were carried out as quickly as possible, so as to make full use of the highest spin rates.

(vii) Air speed maintained at a constant level until the spin rate decayed to below 10 revs/sec.

(viii) Penrecorder stopped, and chart removed for analysis.

7.2.3 Data Analysis

Reduction of the recordings to forces and moments was accomplished by taking about 10 points from each record and using the matrix equation described in section 2.2.7. The matrix coefficients were determined by applying known forces and moments to the model at several different angles of pitch incidence and plotting current signals against force (or moment).

It was found that when the rotational speed of the model had decayed to only a few revolutions per second, the lateral current signals oscillated in synchronisation with an amplitude of approximately ± 2 gm-cm. This was probably the result of i) misalignment of the axis of magnetisation

with the axis of rotation, and (ii) a non-uniform distribution of mass about the rotation axis. (See also section 6.6.2.) The low-pass filtering of the current signals removed this effect from the recordings at the higher spin rates, and there was a lowest speed at which a steady trace could be obtained. This speed was used as the datum for the recording, and was subtracted from the true spin rate at all the points selected for measurement. Correspondingly, the current signal levels at the datum spin rate were subtracted from the values at the points selected for measurement. Data gathered therefore represented the difference in side force at two spin rates, one of which was very low. (The spin rate datum was usually 8 or 10 revs/second in practice.) It was felt that this approach was justified by the approximate linearity of the Magnus force with spin rate at the incidences used for the tests.

Measurement of the spin rate at the selected points on the recording was carried out by counting the number of tachometer pulses in a known distance at the points. A knowledge of the chart speed then gave the rate of rotation. (See also section 6.5.1.)

7.3 Final Technique

7.3.1 Introduction

In essence, the method of force and moment measurement entailed the tape-recording of three signals during the spin-down of the model: the tachometer signal and the two lateral current signals. Reduction of the data was performed off line on a small computer, which produced plots of side force coefficient and yawing-moment coefficient versus spin ratio. For any one base shape, recordings were taken at several incidences in pitch, normally $-\frac{1}{2}^{o}$, 0^{o}, $+\frac{1}{2}^{o}$, 1^{o}, 2^{o}, 3^{o}, 4^{o}, 5^{o}, 6^{o} and 7^{o}. For most of the tests the roughness band described in section 6.6.5 was applied 1.5 body diameters from the nose. The flow velocity varied from test to test, but an average of 65 metres/second (Reynolds number 0.7×10^{6}, based on model length) was employed.

Following development of the technique it was chosen to tape record the data and to delay computer analysis until the end of the programme, allowing the maximum number of test runs to be carried out in the available tunnel occupancy time. A typical run would take approximately 10 minutes to record, and about the same period to analyse. In all, 9 individual base geometries were tested with the roughness band applied, and 2 with the model in the 'clean' condition. A total recording time of approximately 12 hours was needed to acquire the data, and approximately 20 hours of computer time to perform the analyses.

7.3.2 Experimental Arrangement

The experimental arrangement is shown in block diagram form in Fig. 7.1. Some features of this equipment have been described in section 6.7. There was provision for zero adjustment of the current signal amplifiers, and the output voltages were set so that a near-zero output was obtained with no side force. It was not possible to set zero precisely because of the variation in the control currents with roll angle of the model; this was a further effect of the asymmetry of the magnetisation of the core. At near zero spin rates, current fluctuations could be observed arising from this effect, but at spin rates above 20 revolutions per second the fluctuations were not apparent because of the filtering. At spin rates in the range of interest, i.e. 20 -400 revs/second, the low-pass characteristics of the suspension coils themselves also attenuate any such current oscillations.

The pulse amplifier and tachometer were monitored by an oscilloscope, counter-timer and digital voltmeter as shown in Fig. 7.1. As described in Chapter 6, the frequency indicated by the counter-timer was 5 times the spin-rate of the model. The output of the tachometer was set at 2.00 volts for 400 revs/sec.

A monostable with a pulse width of 15 seconds was incorporated into the main cabinet of the suspension control system. This had two functions. The first was to generate a reference pulse to signify the start of a record: this was recorded on a separate channel of the tape recorder and used in the computer analysis. The second was as a calibration voltage source. At the end of a recording session, a pulse of measured amplitude was recorded on all channels, followed by 15 seconds at earth potential. This was used in the computer analysis as a reference voltage, against which the signals were compared in order to recover their original absolute values. This was necessary because the tape recorder could not be relied upon to maintain exactly unity gain.

In addition to the equipment used in the recording of data, two operational amplifier summing circuits were used to provide 'running' values of the force and moment acting on the model for display on an oscilloscope. The circuits performed the simple operations.

$$e_f = ae_1 + be_2$$

$$e_m = ce_1 - de_2$$

where e_1, e_2 are the forward and aft lateral current signals, and a to d are calibration coefficients, the values of which were selected using ten-turn potentimeters. e_{of}, e_{om} are the output voltages proportional to force and moment in the lateral plane. The circuits were useful in setting up the angle of yaw of the model. This was accomplished by rotating the model slowly (at less than 10 revs/sec.) in suspension and turning on the tunnel air flow. Any change in the outputs indicated a non-zero yaw angle with respect to the flow, and this could be trimmed out by adjusting the positon of the rear secondary sensor (see section 6.2). The slow rotation of the model was necessary to eliminate any asymmetry of the aerodynamics of the model, and to allow for the fluctuations of magnetic origin described in section 6.6.2.

The data was recorded on Ampex FR1300 and FR1300A FM tape recorders.* The recording speed was on one tape, four of the 14 available channels being used at one time.

7.3.3 Typical Acquisition Sequences

The initial preparations for a series of test runs were as follows:

(a) Switch on the electronics of the suspension system and allow approximately one hour's warm-up time. Connect up tape recorder and switch on, also allowing an hour for the internal electronics to settle.
(b) Clean all optical surfaces used in position-sensing, especially the window forming the floor of the working section.
(c) Set supply voltages to the lamps at the value used in calibration (5.00 volts for the sources of the diagonal beams, 3.00 volts for the two light sources mounted on the baseplate).
(d) Insert pitch indidence calibration rig into the working section and set the model at nominal zero incidence. Adjust outputs of the position signal amplifiers to zero. Check that integrators are correctly zeroed. If required, carry out incidence calibration with laser optical lever system.

The tests proper were then carried out as follows:

(i) Replace removable section of wind tunnel and suspend the model manually through the access window downstream of the working section.
(ii) Switch on the integrators and adjust the attitude of the model as required.
(iii) Bring up the pneumatic spinning device to the base of the model, adjusting the position of the jet block manually, to give equal clearance on each side.
(iv) Close Perspex access window.
(v) Make tachometer adjustments to produce best waveform on monitor oscilloscope.
(vii) Allow spin rate to increase to maximum ($\sim$ 420 r.p.s.)
(viii) Switch tape recorder to "RECORD".
(ix) Turn off air supply to jets and operate retraction mechanism.
(x) Turn on the injectors and hold the tunnel air speed at a steady value.

---

* It was necessary to use the same type of tape recorder for both recording and reproduction.

(xi) Press button to initiate pulse on fourth channel of recording, start stop-watch.

(xii) After ∿ 130 seconds of recording, stop tape recorder.

(xiii) Turn off tunnel air supply.

(iv) Note initial and final spin rates, dynamic head used, record time.

7.3.4 Data Analysis

Reduction of the data on tape was accomplished using the Marconi Myriad Mk.2 computer of the Data Analysis Centre of the Institute of Sound and Vibration Research, which is equipped with an analogue-to-digital converter, and which is particularly suitable for the processing of tape recorded signals. The Ampex tape recorder was used in reproduce mode with a tape speed of 60 inches/second, i.e. 4 times the speed used during recording. Acquisition of the data by the computer therefore took approximately 30 seconds per test run.

The first program to be run during a computer session was used to acquire the calibration signal (recorded at the end of each group of test runs) and to print out the zero shift and gain of each of the three data channels. The six numbers obtained from this program were then used to correct the reproduced test signals to recover their original recorded levels. A second program stage, 'MAGI', acquired the test data, one channel at a time, smoothed the signals and performed the corrections. The three resulting files of data, containing the forward and aft lateral current signals and the tachometer signal, were plotted out in graphical form at the end of the program. An example is shown in Fig. 7.2. Any obvious errors in the data could be spotted at this stage, and acquisition repeated. A sampling rate of 125 per second was used. With an acquisition time of 32 seconds, this produced data files of 4000 samples.

Having obtained satisfactory plots from the output of 'MAGI', the final program 'MAG2' would be run. This program performed the arithmetic necessary to extract the Magnus force and moment coefficients from the two current signals, and plotted the two coefficients against the spin ratio. Three input numbers were required by the program: the values, D/2V, qS and qSD, where D = the model diameter, V = the air speed,

q = the dynamic head at the model, corrected for tunnel blockage, and S = the cross-sectional area of the model. The values of D/2V, qS and qSD were computed and tabulated against the observed dynamic head for use with this program. Listings of the programs are shown in figures 7.3 and 7.4.

7.3.5 Derivation of the Calibration Constants

The values of the coefficients used in the reduction of the current signal data to Magnus forces and moments were derived in the following way.

Side forces were applied to the suspended model at a measured distance from the reference point, using a thread passing over a pair of low friction pulleys. The reference point in the present case was the centre of the cylindrical section of the 7-calibre AN spinner. The fore and aft lateral current signals were then plotted against applied force. This was repeated with the thread attached at a different point, as far as possible from the first.

If the slopes of the graphs of current signal versus applied force are $m_{1,2}$ for the forward current signal (e_1) and $n_{1,2}$ for the rear (e_2), and the subscript indicates that the point of application was at x_1, x_2, then the following equation can be written for the forces, F, and moments, M:

$$\begin{bmatrix} F \\ M \end{bmatrix} = \frac{1}{m_2 n_1 - m_1 n_2} \begin{bmatrix} n_1 - n_2 & m_2 - m_1 \\ x_2 n_1 - x_1 n_2 & x_1 m_2 - x_2 m_1 \end{bmatrix} \begin{bmatrix} e_1 \\ e_2 \end{bmatrix}.$$

Figs 7.5.and 7.6 show the calibration graphs used in the evaluation of the coefficients. The values of $m_{1,2}$, $n_{1,2}$, and $x_{1,2}$ are listed below.

$$\left.\begin{aligned} m_1 &= 0.0249 \\ n_1 &= -0.144 \\ m_2 &= 0.115 \\ n_2 &= -0.0534 \end{aligned}\right\} \text{volts/gram}$$

$$\begin{aligned} x_1 &= -26.3 \text{ mm} \\ x_2 &= 22.4 \text{ mm} \end{aligned}$$

Using these values, the expression for side force and moment becomes

$$\begin{bmatrix} F \\ M \end{bmatrix} = \begin{bmatrix} 5.96 & -5.93 \\ 30.5 & 23.6 \end{bmatrix} \begin{bmatrix} e_1 \\ e_2 \end{bmatrix} .$$

The numerical values of the matrix elements are entered as data in the program 'MAG2' under variable names 'V1' and 'V2' (see Fig. 7.4).

7.3.5 Computer output

The collected plots of C_f and C_T as functions of spin ratio are shown in Appendix A. Two points need to be made concerning the presentation of data. Firstly, the origin of the 'Y' scale does not necessarily represent zero side force or moment. In fact, the position of the zero is arbitrary, although the calibration of the X and Y scales is correct. This is because the outputs of the current signal amplifiers were not adjusted to give zero output for zero side force, as explained in section 7.3.2. Note that C_f is plotted positive downwards in figures A1 to A23.

8. DISCUSSION OF RESULTS

8.1 Test Conditions

The purpose of this chapter is to discuss the general appearance of the Magnus results for the 7-calibre AN spinner, and to make some comparison with published data. No attempt is made at a theoretical explanation of the detailed form of the curves of the experimental data.

The graphs produced by the incremental plotter of the computer are collected and displayed as 65% photoreductions in Appendix A. The plots of C_f or C_T for one particular base are shown together on one page wherever possible, with the pitch incidence (α) as parameter. The range of spin ratio ($pD/2V$) is normally from 0 - 0.35, the maximum attainable spin rate at the time of the test run and the flow velocity, determining the precise maximum value. The flow velocity could not be kept the same for all test runs, although it was held constant to ± 1% throughout any one particular test. However, velocities were kept within the range 64-71 metres per second for test runs with the roughness band applied, and at 57 metres/sec for tests on the 'clean' model. The mean Reynolds numbers for the measurements on the 9 base shapes are listed in Table 8.1. Tunnel model blockage and lift corrections were less than 2% throughout and were not significant as this is within other experimental errors.

In addition to the graphs of the force and moment coefficients, it is instructive to examine the printout of the current signals themselves, i.e. the output of 'MAG1'. The current signals can be interpreted as measurements of the side forces acting on the nose and tail of the model. If the equations relating the applied force and moment to the values of the current signals are considered, it is possible to find a position x measured upstream from the reference point for the centre of action of the force which will produce no output in one or other of the current amplifiers. The basic equation is

$$F_Y \begin{bmatrix} 1 \\ x' \end{bmatrix} = \begin{bmatrix} a_{11} & a_{12} \\ a_{21} & a_{22} \end{bmatrix} \begin{bmatrix} e_1 \\ e_2 \end{bmatrix}$$

If $e_2 = 0$, then $F_Y = a_{11}e_1$, $x'F_Y = a_{21}e_1$. Thus,

$$x' = a_{11}/a_{21} = 51.2 \text{ mm.}$$

Similarly, if $e_1 = 0$, the required centre of action is given by

$$x' = a_{12}/a_{22} = -39.8 \text{ mm.}$$

This means that the forward current signal e_1 will, on the whole, indicate the strength of the side force at the nose and shoulder of the body; and that the rear current signal, e_2, will indicate the force acting near the base.

A typical output from 'MAGI' is shown in Figure 7.2, where the exponential decay of the tachometer signal is accompanied by a similar decay of the front and rear lateral current signals. This particular recording was of the basic shape (blunt base) at an incidence of 6^o and with the roughness band applied. Both signals are of similar magnitude and investigation of the plots of C_f and C_T confirms that the centre of pressure lies near the reference centre.

The moment reference centre used throughout these measurements lies 2.50 calibres from the base of the model. All models are of the same overall length (7 calibres, 154 mm). This position coincides with the geometrical centre of the cylindrical body of the basic spinner.

TABLE 8.1

Mean Reynolds Number for Series of Tests on Each Base Shape

Case.	Base Shape	Roughness Applied V(m/s)	Re_L	Case	'Clean' Models V(m/s)	Re_L
1(a)	Basic Spinner (blunt base)	71.0	0.76×10^6	1(b)	57.0	0.61×10^6
2	0.046D radius	65.5	0.70×10^6			
3(a)	Hemisphere	66.0	0.71×10^6	3(b)	57.0	0.61×10^6
4	$5^o/\frac{1}{2}$-calibre	66.5	0.71×10^6			
5.	$10^o/\frac{1}{2}$-calibre	66.0	0.71×10^6			
6	5^o/1-calibre	66.0	0.71×10^6			
7	10^o/1-calibre, no cavity	64.5	0.69×10^6			
8	10^o/1-calibre, with 0.071D cavity	65.5	0.70×10^6			
9	10^o/1-calibre, with 0.213D cavity	65.0	0.70×10^6			

8.2 Discussion of Selected Results

The raw data for the variation of Magnus force and moment coefficients with spin ratio at various angles of attack is presented in Figures A1 to A23 associated with Appendix A. Some detailed discussion is included in Appendix A of some of the features and trends of the curves. In this Section, an attempt is made to bring forward some of the more significant results in a distilled form and to indicate some of the major effects of parameters such as base shape.

There are at least four distinct mechanisms associated with the development of Magnus force on axi-symmetric bodies. These are:

1. Non axi-symmetric growth of boundary layer and displacement thickness.
2. Full flow separation leading to the formation of asymmetric standing vortices.
3. Laminar separation and turbulent reattachment resulting in a standing bubble but no vortices.
4. Effect of shape on base flow.

The relative contributions and centres of action of these components will be a function of boundary layer state, spin ratio and incidence. It may be anticipated that the results will be sensitive to Reynolds number and model surface roughness. All the above sources may be present in the incidence range tested (up to about 6°) whereas at higher incidences the standing vortices tend to dominate. The results obtained here only indicate the total force and centre of action[†] so that it is not possible to determine which is the dominant source, if any.

The data displayed in the following figures was obtained by smoothing the time history records of the raw signals shown in Figures A1 to A23. Magnus force coefficients for the basic blunt base body are shown in Fig. 8.1(a) and for the hemispherical base in Fig. 8.1(b), in both cases with roughness applied to the model. Both exhibit negative values at low incidence ($<3^{\circ}$ approximately); this tends to disappear with increasing spin ratio. At incidences above 3°, C_f increases monotonically and almost linearly with spin ratio for the blunt base. For the hemispherical base, however, there are still significant changes in the flow picture taking

---

[†]The "centre of action" is the centre of pressure for the Magnus force but the term is retained to distinguish it from the lift centre of pressure.

place as spin ratio and incidence increase, almost certainly due to the base effect.

The effect of adding roughness to the model is illustrated in Figs. 8.2(a) and 8.2(b). For the blunt base model, large differences can occur particulary at the higher incidences. These differences are even more pronounced for the hemispherical base in Fig. 8.2(b), arising from the large variation in location of separation lines possible with such a geometry. Large unsteady forces are also present for the smooth model caused by movements in separation position. Since the test Reynolds numbers were low, it was decided in running and in presenting results to concentrate on models with applied roughness, as being more representative of behaviour at Reynolds numbers of interest to the contract supporting organisation.

The variations of C_f with spin ratio are highly non-linear at some incidences and with some base shapes. Whilst the forms of the graphs vary systematically, it is not possible to produce simple analytic relationships with empirical coefficients valid over a wide range of incidence, spin ratio and Reynolds number values. However, the rate of change of Magnus force coefficient with spin ratio as spin ratio tends to zero is a useful indicator of the presence of the negative Magnus force. When the derivative is negative and the incidence positive there will be a negative C_f. The derivative is plotted as a function of incidence for various base shapes in Figures 8.3(a) and 8.3(b). Except for very low incidence there is a roughly linear variation and, although omitted in most cases for clarity, all the curves pass through the origin and are anti-symmetric with respect ot the vertical axis. The change in derivative value as each curve passes through the origin is very rapid. Above a particular incidence which depends on base shape, the negative Magnus force will not occur at any spin ratio. All the base shapes but one exhibit a negative C_f. The exception is the 1 calibre 10° boattail base with the deeper 0.231 D cavity shown in Figure 8.3(b). The effect of the cavity was generally to make the aerodynamic force and moment behaviour more ordered and to reduce the unsteady components.

A summary of the effect of base shape on the variation of Magnus force coefficient with spin ratio is presented in Figure 8.4 for the upper incidence tested (6°). The irregular behaviour of the hemispherical

base is emphasised. Putting a small corner radius on the basic blunt base model has a significant effect which is neither that of boattailing nor of an initial step towards a fully hemispherical base. Boattailing causes a systematic increase in C_f over the whole spin ratio range. At 6^o incidence, the base cavities have only small effects on C_f.

Raw Magnus moment data is included in Figs. A1 to A23 and features of high (6^o) and low (2^o) incidence behaviour are summarised in Figs. 8.5(a) & (b) in the form of effective centres of action of the Magnus force. These should be considered in conjunction with the corresponding variations in magnitude and sign of the Magnus force. The curves in Fig. 8.5(a) at 2^o incidence fall into two sets. At low spin ratios, the centre of action lies outside and behind the base of the model and the Magnus force coefficient is negative. As the negative Magnus force reduces to zero with increase in spin ratio, the centre of action retreats further behind the base indicating the presence of a moment resulting from a positive Magnus force on the main body and a negative base Magnus force of approximately equal magnitude. With further increase of spin ratio, the net Magnus force becomes positive and its centre of action moves rearwards from in front of the nose and has the appearance of settling down in the region of the reference centre at high spin ratio. The interpretation placed on this result is as follows:

1. The Magnus force developed on the main body is distributed with an effective centre of action mid-way along the body. The force increases steadily with spin ratio and its centre of action remains fixed.
2. The local base flow results in a base region contribution to Magnus force which initially increases in a negative sense with spin ratio until it dominates, but then reduces and eventually becomes small in magnitude when compared with the body contribution at high spin ratios.

The detailed balance between components (1) and (2) depends very much on detailed base shape. In the case of the base with the deeper (0.213 D) cavity, the probable establishment of a circulating flow in the cavity stabilises the base flow and no significant negative force is created.

The concept of a distributed body component and a local base component of Magnus force can also be used to interpret Fig. 8.5(b) for the 6^{o} incidence case. However, at this incidence the body component dominates at all spin ratios except for the hemi-spherical base. It increases monotonically with spin ratio whilst its centre of action does not move significantly. The effect of adding boattail is to move the centre of action rearwards systemmatically e.g. ½ calibre boattail moves the centre ½ calibre back. Again the presence of a small corner radius does not result in a behaviour intermediate between the blunt and hemi-spherical bases. In the case of the hemi-spherical base, for spin ratios below 0.2 the Magnus force is positive and increasing with spin ratio, and arises largely from the main body. Above about 0.2 the force falls although it never becomes zero or negative. This is accompanied by a rapid forward movement of the centre of action, indicative of the presence of a negative base force component.

8.3 Comparison with Existing Data

The detection of the small, but significant, negative Magnus force at low incidences ($<3^{o}$) confirms the results of Haldeman et al[16] who found a similar effect in the 0.to 0.15 spin ratio range with a 5 calibre AN spinner. In the latter tests Reynolds numbers based on length ranges from 7.7×10^{5} to 12.6×10^{5} but no boundary layer trip was used. In the present tests the negative force persisted even with added roughness although the ranges of incidence and spin ratio for its presence were modified. No other experiments appear to have explored the low incidence region so thoroughly but have concentrated on incidence greater than 5^{o}. (For example, Green[15] and Fletcher[19,20]). Negative Magnus forces do occur[20] at large incidence ($>15^{o}$) but apparently only at low Reynolds numbers[19] (4×10^{5} and less). For the low incidence occurrence, the negative coefficient is still present at $R_{e_L} = 12.6 \times 10^{5}$ and with the model having applied roughness. The possibility therefore exists of two distinct mechanisms, one at high incidence and low Reynolds numbers associated with laminar separation and turbulent reattachment[21] and the other at low incidence involving much smaller cross-flow components and sensitive to base shape.

At high incidences and high Reynolds numbers, the contribution from the standing vortices will dominate the Magnus force. In order to avoid this, and the low incidence negative force, a mid range of angles of attack (5^{o} to 15^{o}) was chosen in an attempt to correlate some of the available results with the simple laminar boundary layer theory of Martin[10]. His relationship for Magnus force as set out in section 5.3 was used as the basis for the correlating factor shown in Fig. 8.6. Whilst there is a broad measure of agreement, such a factor does not appear to be satisfactory for the prediction of accurate values of Magnus force. It should be noted that differences exist between test conditions other than those accounted for in the correlating factor, e.g. sting presence or absence, applied roughness, tunnel flow turbulence level, nose geometry, etc. These differences may well be very important because the test Reynolds numbers were all in the critical region for boundary layer transition.

8.4 Skin frictional torque

In addition to producing plots of the three data signals, the Myriad computer program 'MAG1' included an option allowing a graph of the natural logarithm of the tachometer voltage (e_3) to be output. (See Fig. 7.3 for a print-out of the program.) A typical example is shown in Fig. 8.7. The graph follows a straight line closely, indicating an exponential decay of spin rate, until it falls below about 50 rev/sec. Coupling of the rotational mode of the model with the position and attitude control loops , resulting from magnetic asymmetries and dynamic imbalance, leads to a reduction in the decay rate at the lowest spin rates. In some circumstances, the model could remain spinning indefinitely at a spin rate in the 0 - 50 rev/sec range.

Measurements were made of the slopes of the graphs at the start of the recorded data ($t = 0$) for several different base configurations. On the assumption that the spin rate decays exponentially,

$$p = p_0 e^{\lambda t},$$

where p_0 is the spin rate at $t = 0$, and λ is the decay constant. Since the spin rate is proportional to the tachometer output voltage (e_3),

$$\lambda = \frac{d}{dt}(\log_e e_3)_{t=0}.$$

Values of λ averaged over several pitch incidences for each base shape are shown in Table 8.2. The value of λ for the basic spinner indicates the quickest rate of decay, probably as a result of the slightly higher Reynolds number used in the tests on this model. The fact that the decay constant is increased by an increase in Reynolds number is evidence that the boundary layer was partly laminar and partly turbulent along the length of the model. This can be deduced from the fact that the skin friction coefficient is greater for a turbulent boundary layer than for a laminar one, and that both laminar and turbulent skin friction coefficients fall with an incease in Reynolds number.* The similarity of the values of λ for the three bases tested at $Re_L = 0.71 \times 10^6$ appears to suggest that the base shape is not of great importance in this case.

It is not known what proportion of the decay constant resulted from the electromagnetic damping of the suspension system (see section 6.6.3), however it was probably at least of the order of the aerodynamic part. This uncertainty meant that no quantitative measurements of the skin friction coefficient could be attempted.

---

* Prandtl [23] gives the following formulae for the skin friction coefficient, c_f, on a flat plate:

$$c_f = 1.328 Re^{-\frac{1}{2}} \quad \text{(Laminar boundary layer)}$$

$$c_f = 0.074 Re^{-0.2} \quad \text{(Turbulent boundary layer).}$$

TABLE 8.2

Base shape	λ (sec^{-1})	Re_L
Basic spinner	-0.140	0.76×10^6
Hemisphere	-0.131	0.71×10^6
5^o-$\frac{1}{2}$ calibre	-0.130	"
10^o-$\frac{1}{2}$ calibre	-0.130	"

Measured values for the spin rate decay constant

9. CONCLUSIONS

This thesis has described the development of techniques of force and moment measurement for use with a magnetic suspension and balance system. Most of the work was directed towards the measurement of Magnus force and moment on the 7-calibre AN spinner, chosen because its geometry made it an easy model to suspend. Data was collected on the steady aerodynamic coefficients C_D, C_L, C_M and C_Z, mainly as a supplement to the Magnus data, but also as a validation of the basic technique of force and moment measurement.

A comprehensive set of measurements of the Magnus force and moment coefficients of the 7-calibre model with 9 different base shapes is presented in Appendix A of this thesis. The measurements are free from errors arising from sting interference. The range of angles of attack was from 0° to 7°, the spin ratio range was 0 to 0.3, the wind tunnel Mach number was typically 0.2, and the length-based Reynolds number was approximately 7×10^5.

Large variations in the Magnus force and moment were produced by changes in base geometry, and by the addition of a roughness band. Confirming the results of workers at M. I. T.[16], a negative Magnus force was found at low incidence and low spin ratio. This effect ocurred with all base shapes except one; the latter being the 1 calibre 10° boattail with base cavity of depth 0.213 calibres. The large influence of base shape implies that the presence of a sting support will modify the flow and Magnus force characteristics by a significant but unpredictable amount.

Comparison with other published results suggests that negative Magnus force is produced under two separate circumstances: one is at low incidence and low spin ratio, the other at high incidence but low Reynolds number.

Two components of the Magnus force on the 7 calibre model can be distinguished: -

1. A positive distributed force on the main body which increases monotonically, but not linearly, with spin ratio and incidence,
2. A local negative force at the base which is sensitive to base geometry, incidence, and boundary layer state.

The main advantages of the magnetic suspension system over the conventional wind tunnel balance have been shown to be:(i) absence of mechanical supports, removing the possibility of flow interference and the accompanying uncertainties in aerodynamic measurements, and (ii) the potentially high speed of data collection made possible by the electronic nature of the system. It may also be noted that the sensitivity of a magnetic balance is far greater than that of a mechanical one - for instance, in the Magnus force testing, the maximum value of the side force was approximately 6 grams. Finally, it may be said that, with the single drawback of low Reynolds number, the magnetic suspension balance is a convenient and effective tool for the evaluation of dynamic and static characteristics of aerodynamic models.

NOMENCLATURE

$\underline{A}$	Matrix of a_{ij}
$A(s)$	Laplace transform of $\alpha(t)$
a_{ij}	Matrix element
$\underline{B}$	Magnetic induction
B_r	Remanence
$(BH)_{max}$	Maximum energy product
b_{ij}	Matrix element
$\underline{C}$	Matrix of c_{ij}
C_D	Drag coefficient
C_{DB}	Base drag coefficient
C_f	Magnus force coefficient, $C_f = F_Y/qS$
C_L	Lift coefficient
C_M	Pitching moment coefficient
C_{PB}	Base pressure coefficient
C_T	Magnus moment coefficient, $C_T = M_Y/qSD$
C_Z	Normal force coefficient
C	Capacitance
$C(s)$	Transformed position signal
c_{ij}	Matrix element
c_f	Skin friction coefficient
D	Diameter of cylinder, or maximum diameter of model
D_B	Base diameter
d_{ij}	Matrix element
d	Dummy sting diameter
$E(s)$	Transformed voltage signal
$e_{1,2}$	Output voltages of current signal amplifiers
e_3	Axial current signal, or tachometer output voltage

e_i, e_o	Input and output voltage, respectively
e_f, e_m	Voltages proportional to side force and moment, respectively
$\underline{F}$, F, F_X, F_Z	Force vector, and force components
F_Y	Magnus force
g	Acceleration due to gravity
G(s), H(s)	Transfer functions
H_c	Coercivity
$\underline{H}_{1,2}$	Magnetic field vectors
H_z	z-component of magnetic field vector
H_{z0}	H_z at $z=z_0$
I(s)	Laplace transform of i(t)
I_1	Moment of inertia in pitch
I_3	Pricipal moment of inertia about roll axis
i	Current
K	D.C. gain of circuit
K_p	Loop gain
k	Gain at $s = \infty$ divided by D.C. gain
k_{cr}	Critical grain size
L	Length of body
L_c	Coil inductance
ℓ	Dipole length, or length of cylinder or dummy sting
M	Moment
M_Y	Magnus moment
$\underline{m}$	Magnetic moment vector
m	Mass of model, or magnetic moment
$m_{1,2}$	Gradients of calibration curves
$n_{1,2}$	Gradients of calibration curves

p_1	Static pressure in working section, or pole in s-plane
p_2	Static pressure 0.5 m upstream of model, or pole
p_b	Base pressure
p	Spin rate (radians per second)
p_0	Spin rate at t = 0
q	Dynamic pressure
q_1	Dynamic pressure in working section
q_2	Dynamic pressure 0.5 m upstream of model
q_m	Magnetic pole strength
R	Total circuit resistance
$R_{1,2,3}$	Resistance values
Re_D, Re_L	Reynolds number based on model diameter and length, respectively
R(s)	Transformed position demand signal
Re_x	Reynolds number at distance x from nose of model
r	Cylinder radius
S	Cross sectional area of model, $S = \pi D^2/4$
s	Laplace operator
T	Torque
T_α	Torque component about horizontal reference axis
t	Time
U	Mean flow velocity
u	Velocity fluctuations in the x - direction
u_τ	Frictional velocity
V	Free stream velocity
x	Distance down stream from model nose
x'	Distance of centre of action of Magnus force for zero change in lateral current, measured upstream of reference point.
$x_{1,2}$	Axial coordinate of point of application of side force

x,y,z,z_0	Rectangular coordinates in the balance system
$z_{1,2}$	Zeros
$Z(s)$	Laplace transform of $z(t)$
α	Pitch angle
β	Yaw angle
γ	Roll angle
δ^*	Boundary layer displacement thickness
ξ	Damping ratio
Γ	Circulation
ν	Kinematic viscosity
ρ	Density, or electrical resistivity
σ	Electrical conductivity
τ,τ_1	Time constant
τ_ω	Wall shear stress
∇	Gradient
λ	Decay constant of spin rate

REFERENCES

1. Goodyer, M.J. — Ph.D. Thesis, Southampton University, 1966.

2. Lafay — "Sur l'inversion du Phénomène de Magnus" Comptes Rendues, Vol. 151, 1910.

3. Van Aken, R.W. and Kelly, H.R. — "The Magnus force on Spinning Cylinders". NAVORD Report 5583, NOTS 1784, China Lake, California, June 1957.

4. Swanson, W.H. — "The Magnus Effect: a Summary of Investigations to Date". J. Basic Engg. Sept. 1961 p.461

5. Martin, J.M. — "An Experimental Correlation between the Flow and Magnus Characteristics of a Spinning Ogive-nose Cylinder". Ph.D. Dissertation, University of Notre Dame, Indiana, August 1971.

6. Lando, D.W. — "An Investigation to Control the Magnus Characteristics of Symmetrical Fin and Nonfin Bodies". Ph.D. Dissertation, University of Notre Dame, Indiana, May 1972.

7. Ingram, Lusardi and Nicolaides — "Effects of Rifling and N-vanes on the Magnus Characteristics of Bodies of Revolution". AIAA Ppper No. 72-790, 1972.

8. Jacobsen, I.D. — "Influence of Boundary Layer Transition on the Magnus Effect" Ph.D. Dissertation, University of Virginia, Charlottesville, June 1970.

9. Jacobsen, I.D. and Morton, J.B. — "Boundary Layer Stability on a Yawed Spinning Body of Revolution and its Effect on the Magnus Force and Moment". NASA CR - 2060, June 1972.

10. Martin, J.C. — "On Magnus Effects Caused by the Boundary Layer Displacement Thickness on Bodies of Revolution at Small Angles of Attack". J, Aeronautical Sci., June 1957.

11. Kelly, H.R. and Thacker, V.R. — "The Effect of High Spin on the Magnus Force on a Cylinder at Small Angles of Attack". NAVORD Repprt 5036, NOTS 1381, Feb. 1956.

12. Sedney, R. — "Laminar Boundary Layer on a Spinning Cone at Small Angles of Attack in Supersonic Flow". J. Aeronautical Sci., June 1957.

13. Jacobsen, I.D., Vollmer, A and Morten, J.B. — "Calculation of the Velocity Profiles of the Incompressible Boundary Layer on a Yawed, Spinning Cone and the Magnus Effect". RLES Report No. ESS-3318-104-73 University of Virginia.

14. Power and Iverson — "Magnus Effect on Spinning Bodies of Revolution". AIAA Journal, Vol. 11, No. 4, April 1973.

15. Green, J.E. — "A Summary of Experimental Magnus Characteristics of a 7- and 5-calibre Body of Revolution at Subsonic through Supersonic Speeds". NAVORD Report 6110; 1958.

16. Haldeman, C.W., Coffin, J.B., Birtwell, E. and Vlajinac M. — "Improvements in the Magnetic Balance System Required for Magnus Testing". I.C.I.A.S.F. 73 RECORD, p. 24, 1973.

17. Henderson, R.I. — "Magnus Force Measurements using a Magnetically-suspended Body of Revolution" AASU Report No. 328, Southampton University, Sept. 1973.

18. Schlichting, H. — "Boundary Layer Theory". McGraw Hill.

19. Fletcher, C.A.J. — "The Magnus Characteristics of a Spinning Inclined Ogive-cylinder Body at Sub-critical Reynolds Numbers in Incompressible Flow". Australian WRE Report 423, June 1971.

20. Fletcher, C.A.J. — "Investigation of the Magnus Characteristics of a Spinning Inclined Ogive-Cylinder Body at M = 0.2". Australian WRE Technical Note HSA 159, October 1969.

21. Fletcher, C.A.J. — "An Explanation of the Negative Magnus Side Force Experienced by a Spinning, Inclined Ogive-cylinder". Australian WRE Technical Note 489, Nov. 1971.

22. Henderson, R.I., Goodyer, M.J., and Judd, M. — "Measurements of Magnus force on a Spinning Projectile, including the influence of Base Shape". AASU Report, Southampton University, Dec. 1975.

23. Prandtl, Ludwig. — "Essentials of Fluid Dynamics". Blackie, 1952.

24. Henderson, R.I. and Abdel-Kawi, S. "Subsonic Sting Interference Measurements using a Magnetically Suspended Blunt-Based Model" AASU Report No. 320, Southampton University, 1972.

25. Pankhurst, R.C. and Holder, D.W. "Wind Tunnel Technique" Pitman, 1952.

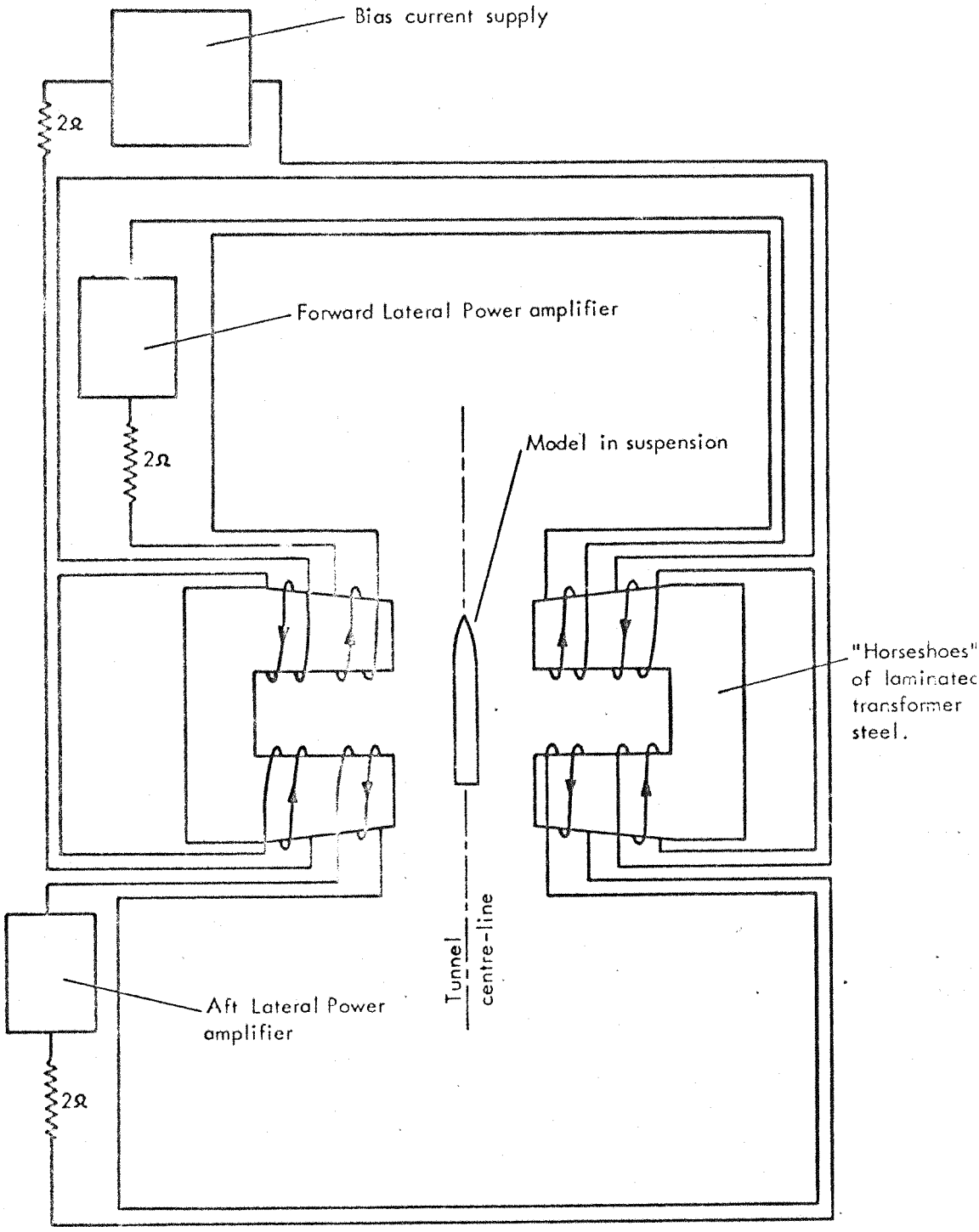

FIG.2.1. THE LATERAL ELECTROMAGNET SYSTEM VIEWED FROM ABOVE.(ROLL CONTROL CIRCUITS OMITTED).

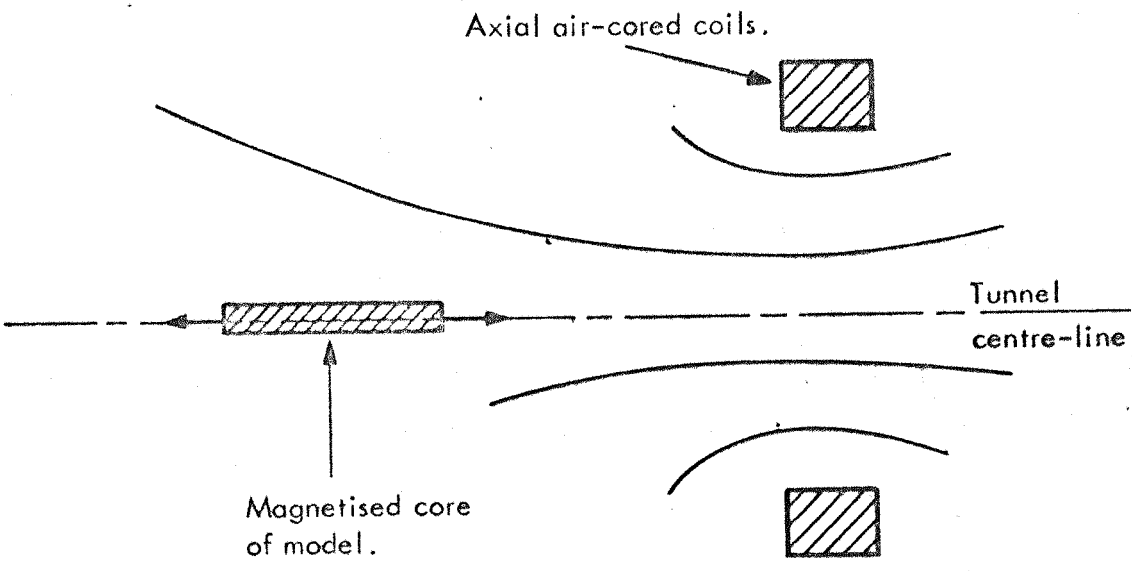

FIG. 2·2. AN ILLUSTRATION OF THE PRINCIPLE OF AXIAL FORCE GENERATION.

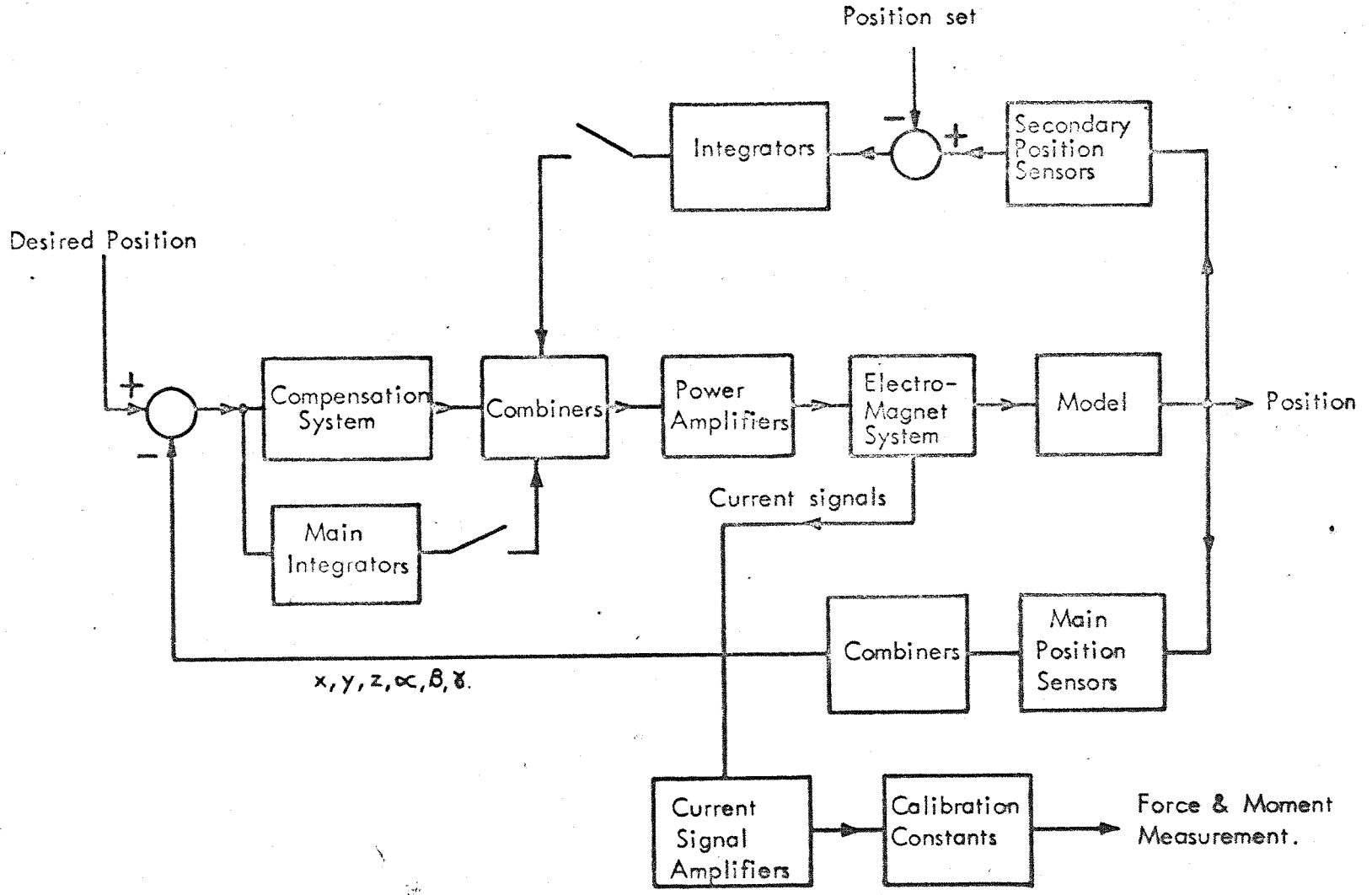

FIG 2.3. FUNCTIONAL BLOCK DIAGRAM OF COMPLETE SUSPENSION/BALANCE SYSTEM.

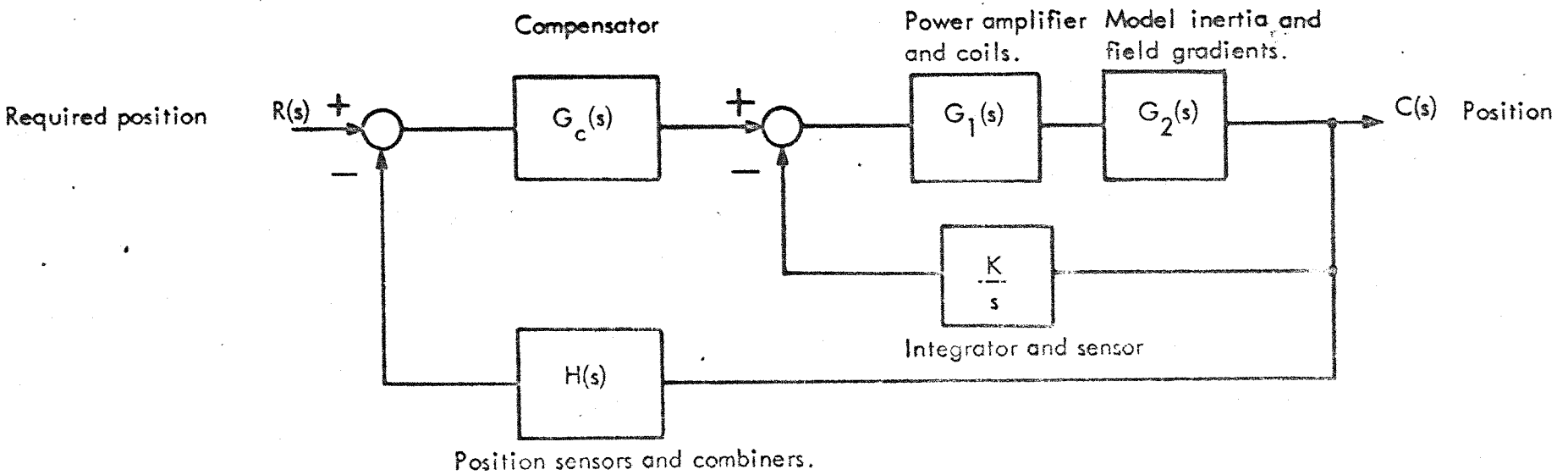

FIG. 2.4. BLOCK DIAGRAM OF FEEDBACK CONTROL SYSTEM FOR ONE DEGREE OF FREEDOM.

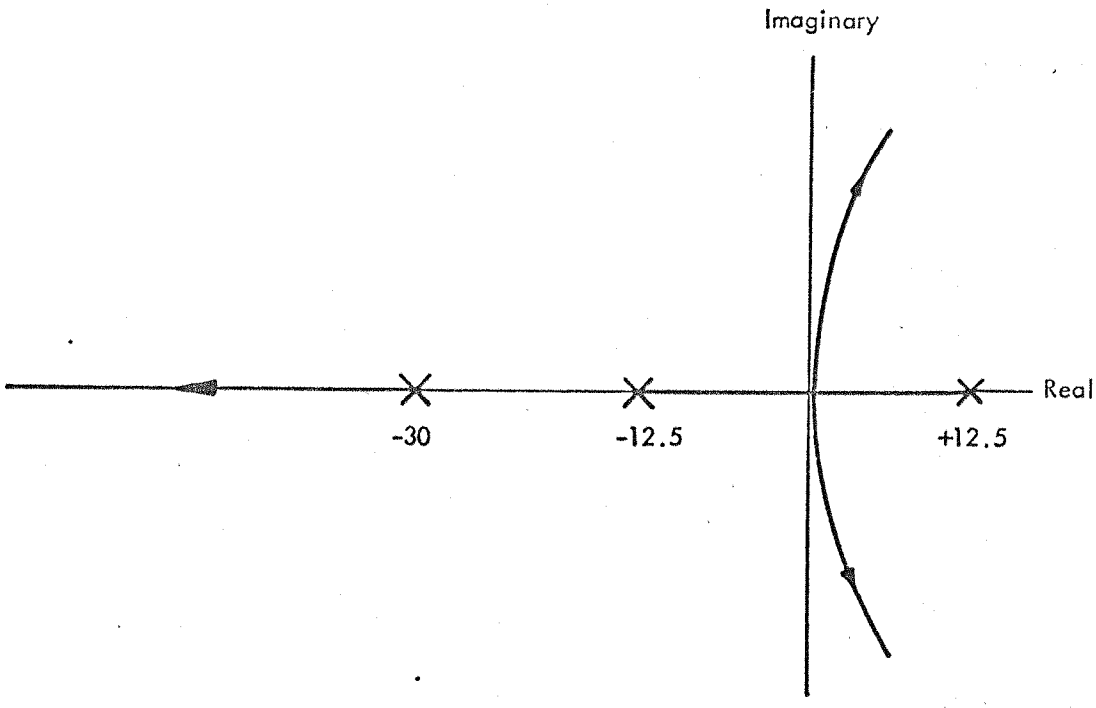

FIG. 2.5. ROOT LOCUS DIAGRAM, UNCOMPENSATED SYSTEM

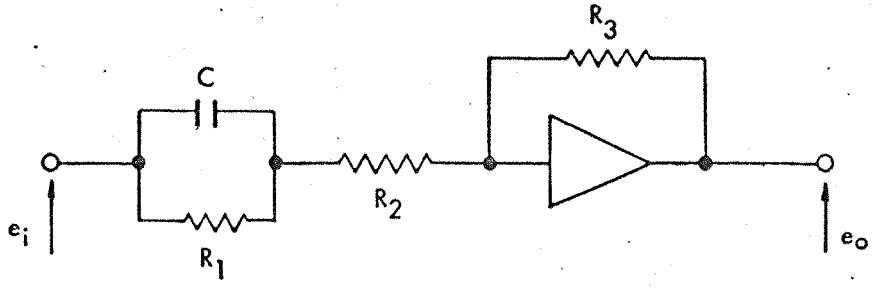

FIG 2.6. PHASE-ADVANCE STAGE USED IN THE FEEDBACK CONTROL LOOPS.

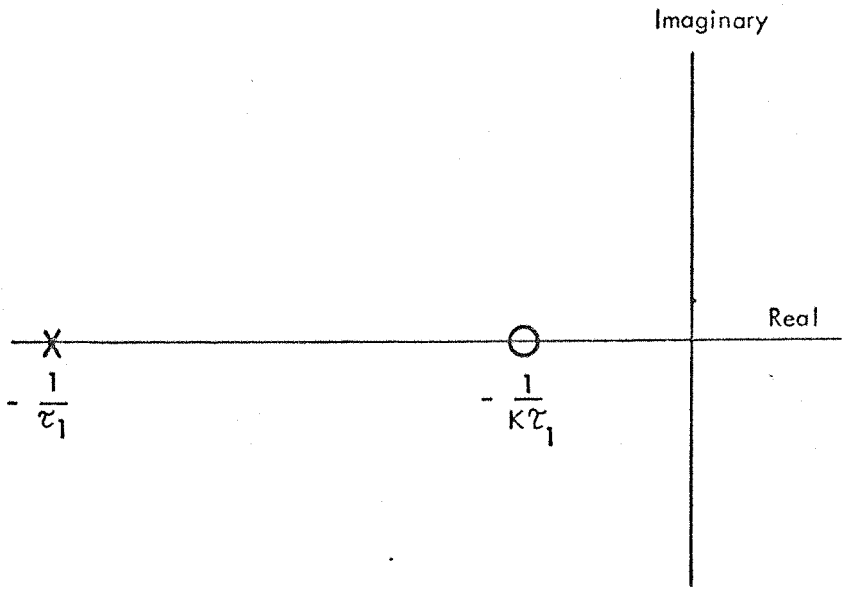

FIG. 2.7. POLE-ZERO DIAGRAM OF THE NETWORK SHOWN IN FIG. 5-6.

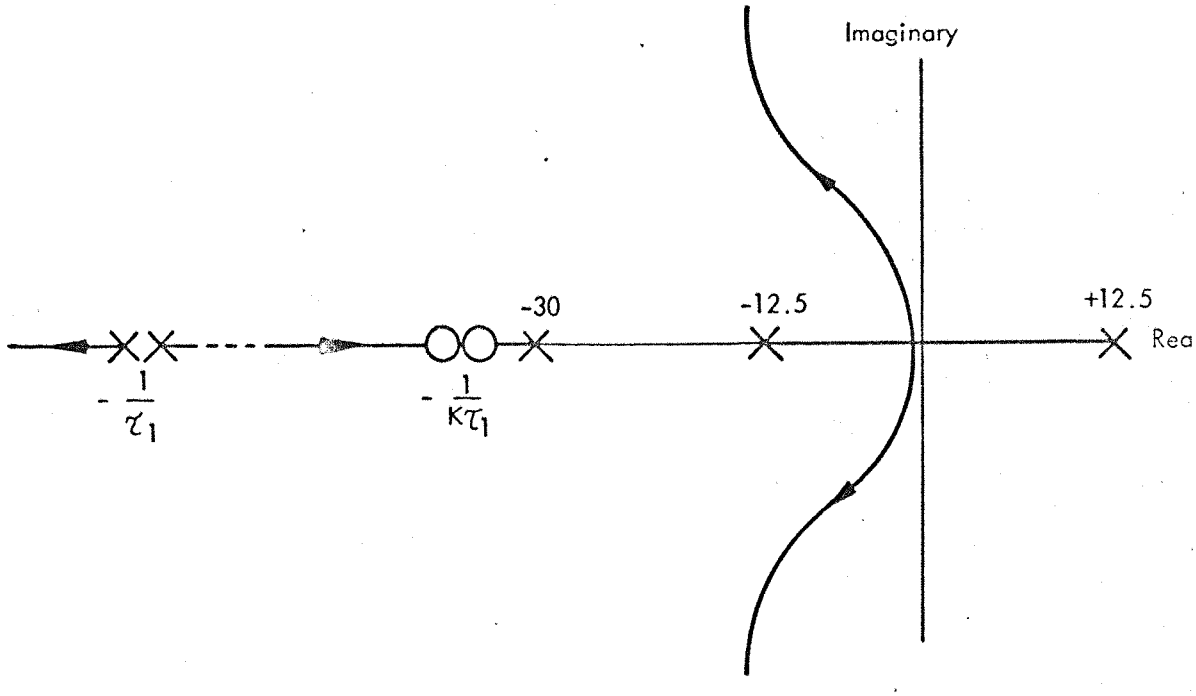

FIG. 2.8. ROOT LOCUS DIAGRAM, COMPENSATED AXIAL CONTROL SYSTEM.

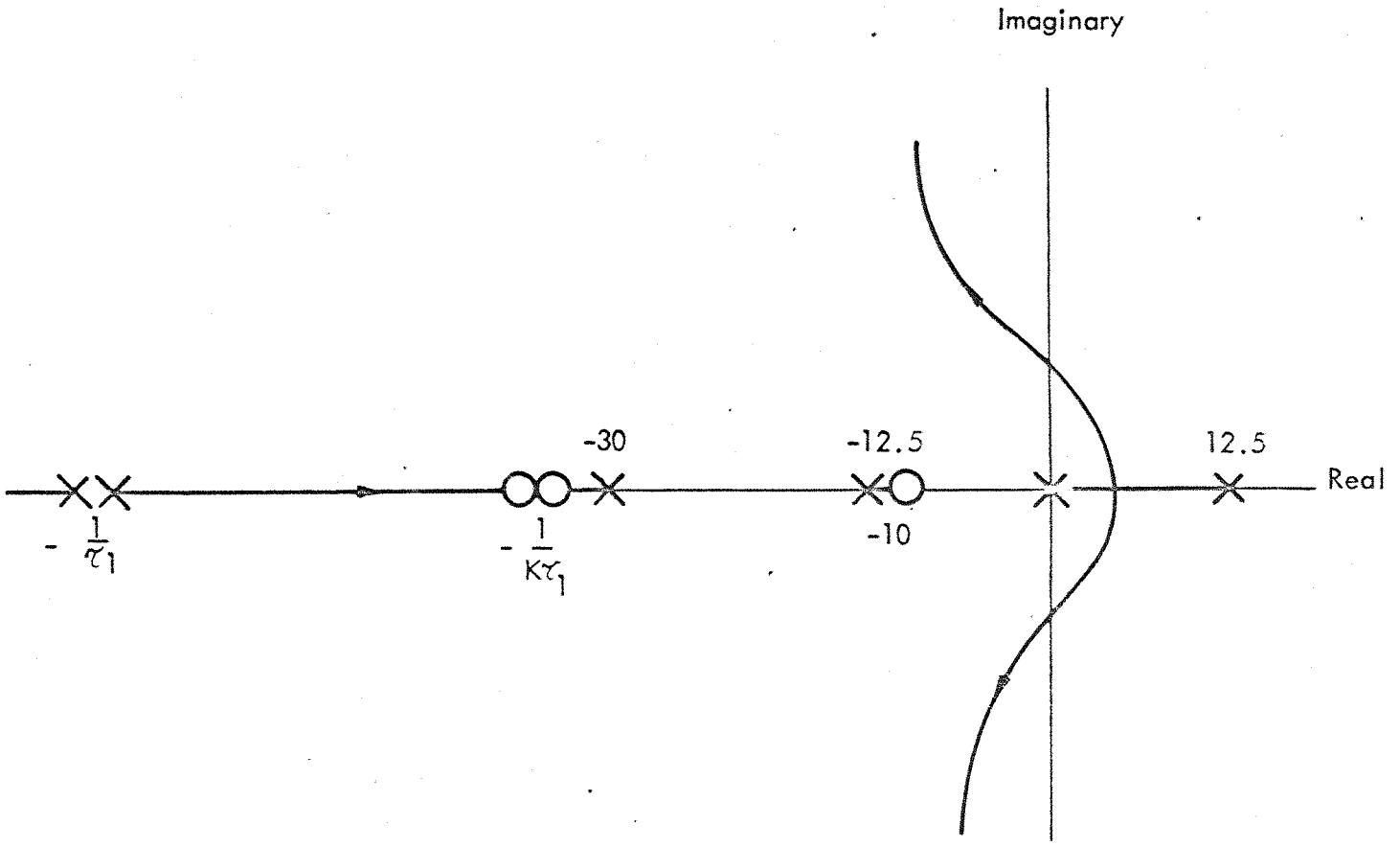

FIG. 2.9. ROOT LOCUS DIAGRAM , COMPENSATED SYSTEM WITH INTEGRAL FEEDBACK.

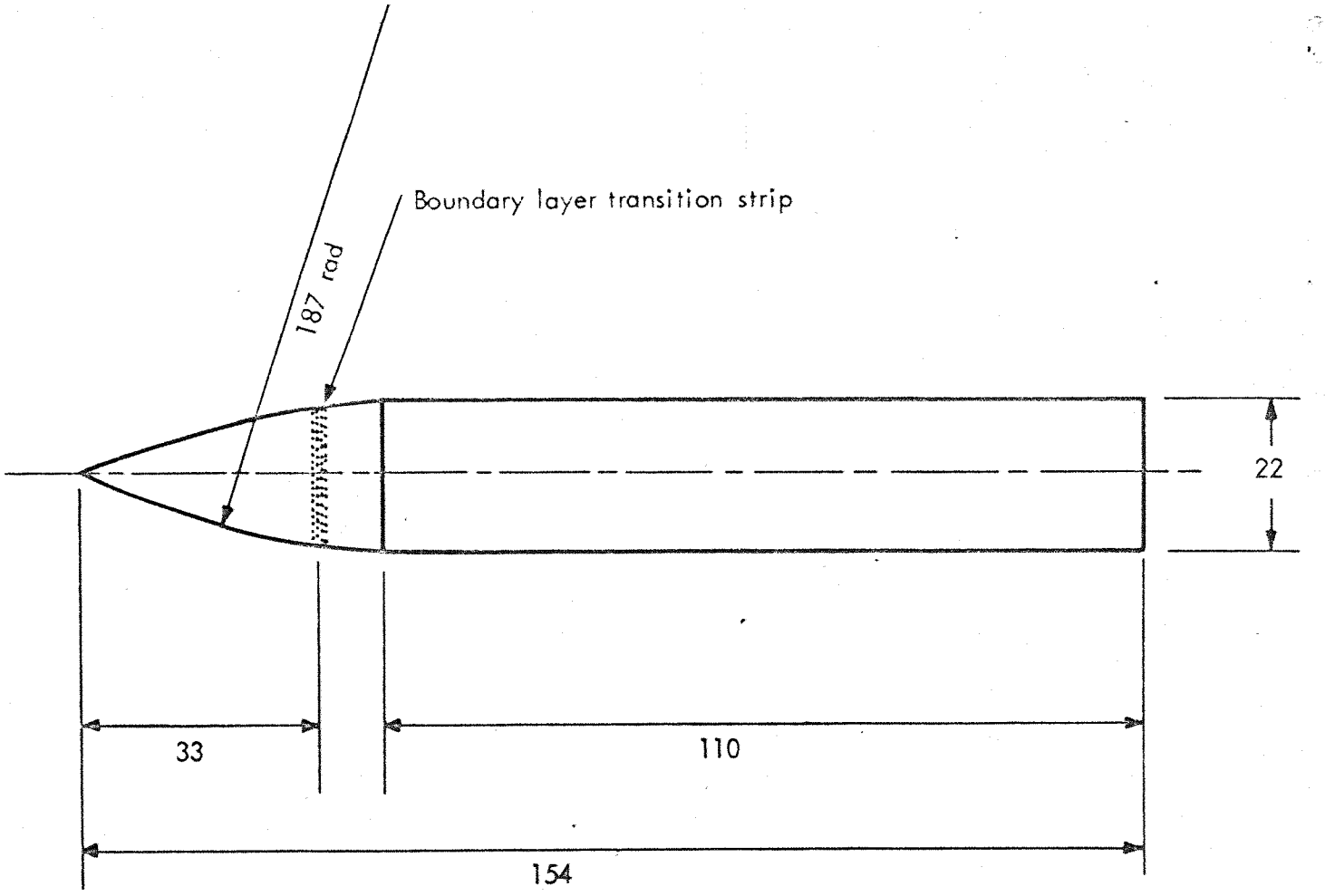

FIG.3-1. OUTLINE OF THE 7-CALIBRE A-N SPINNER. THIS IS THE BASIC MODEL, HAVING A BLUNT BASE. THE LOCATION OF THE TRANSITION BAND IS SHOWN.

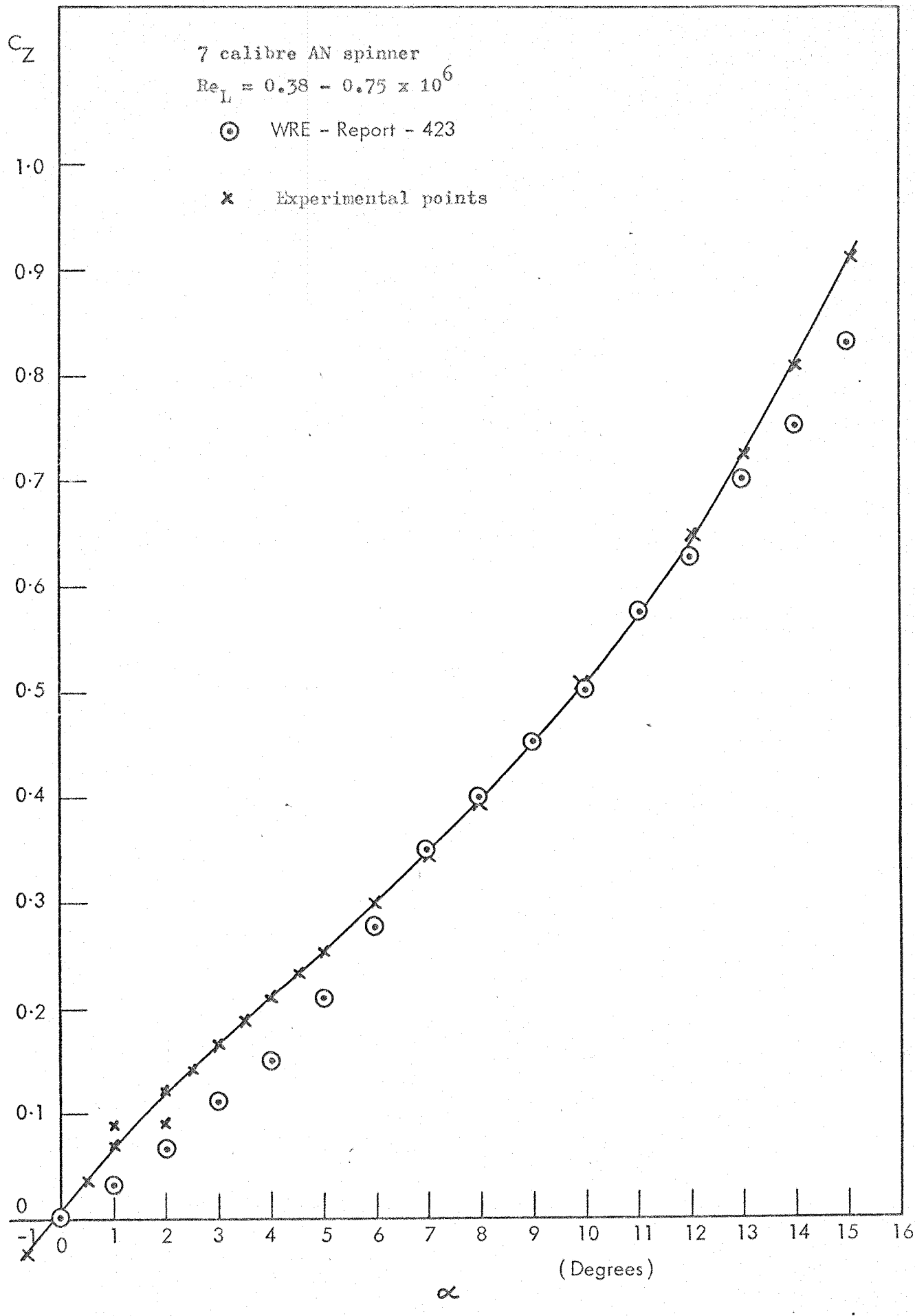

FIG 4.1 Normal force coefficient

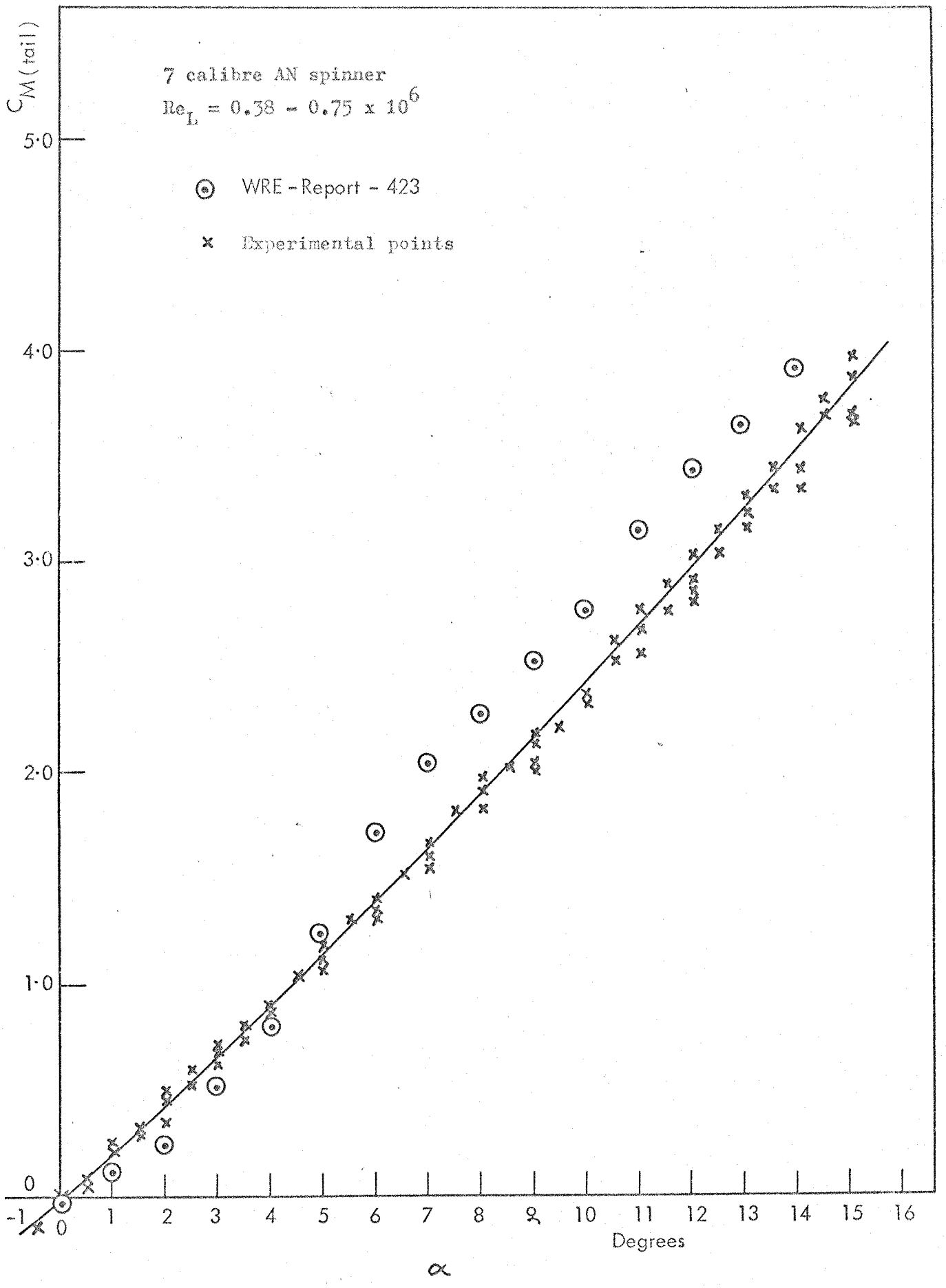

FIG 4.2 Moment coefficient referred to base

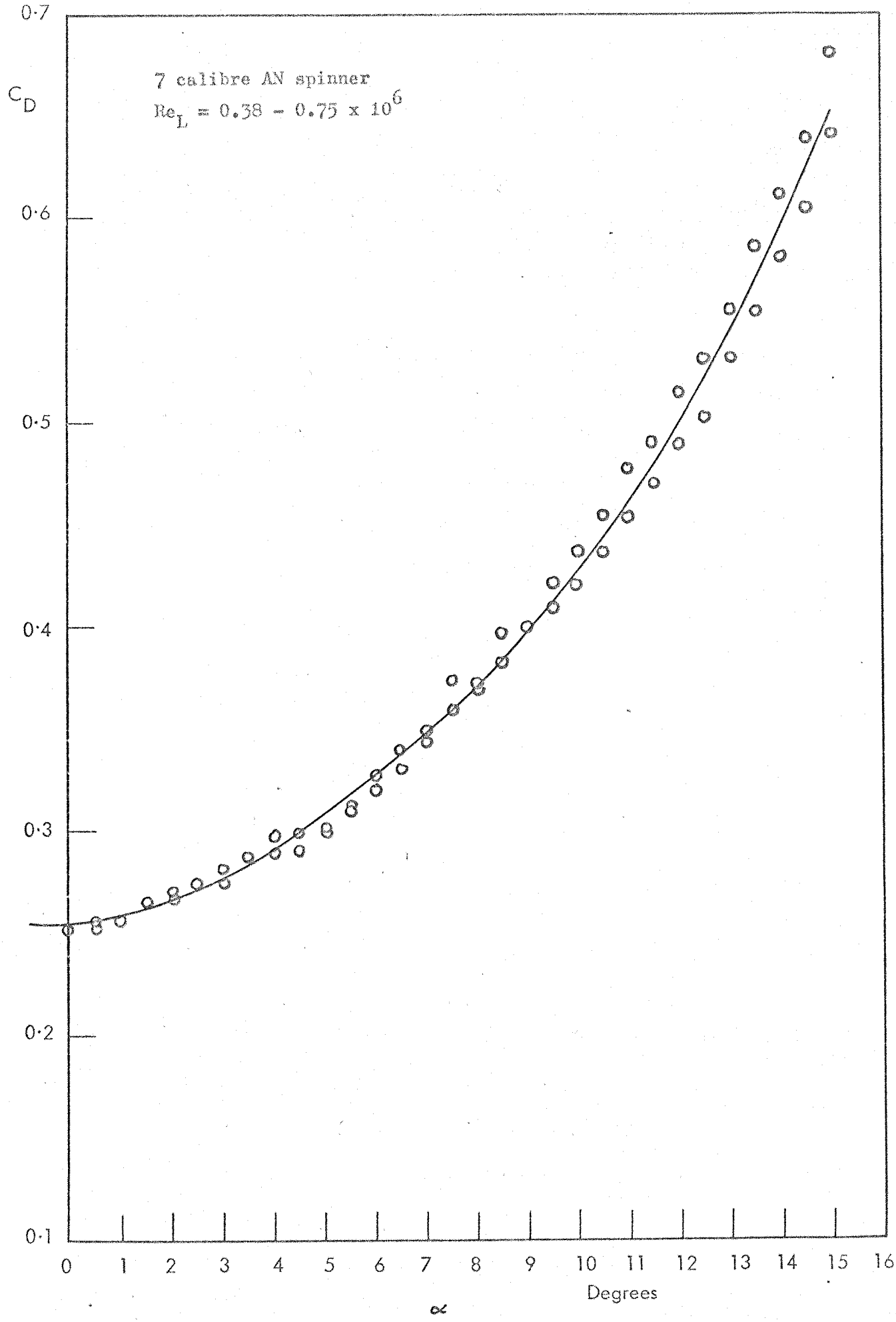

FIG 4.3 Drag coefficient vs. incidence

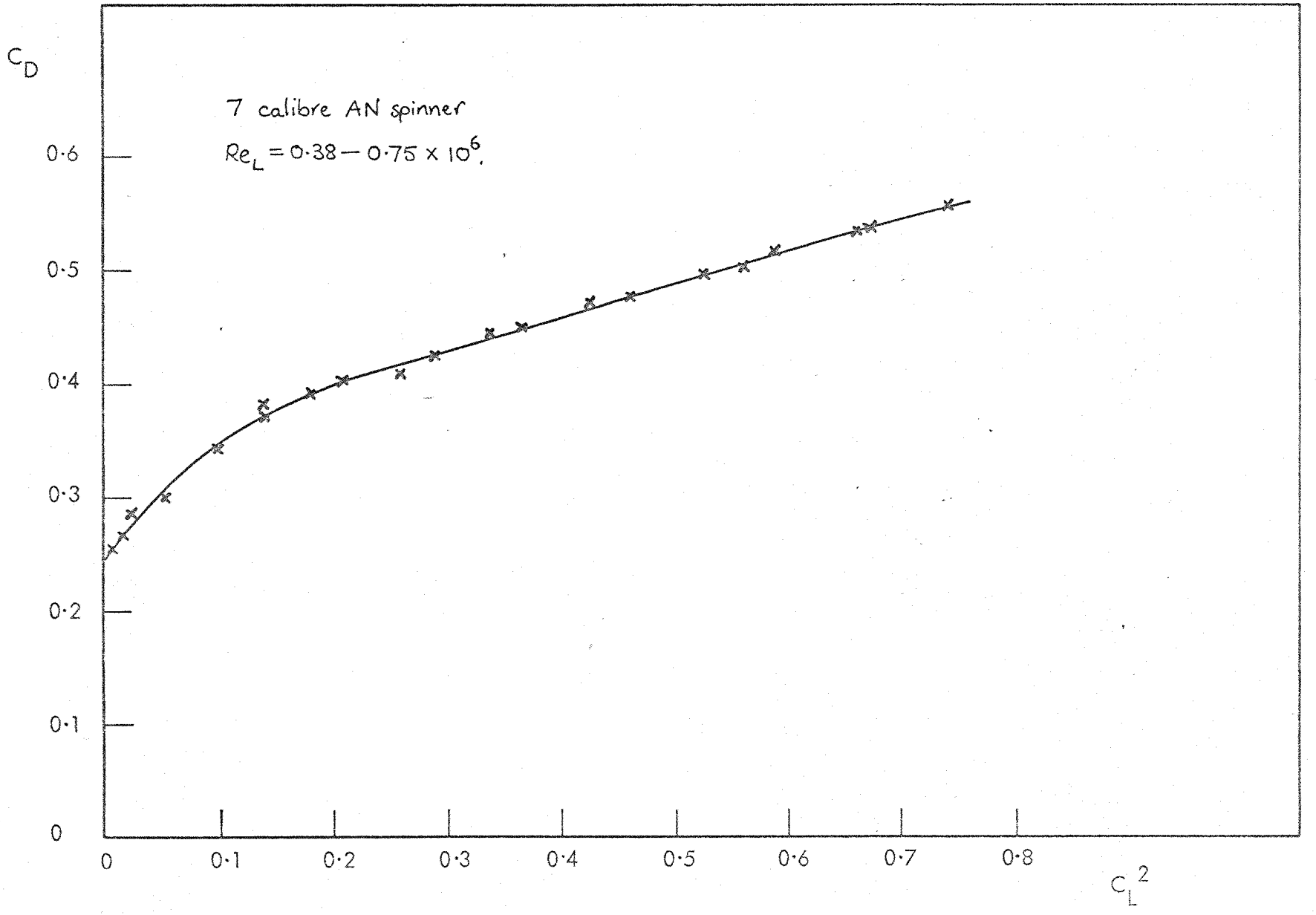

FIG 4.4 DRAG COEFFICIENT AS A FUNCTION OF THE SQUARE OF THE LIFT COEFFICIENT

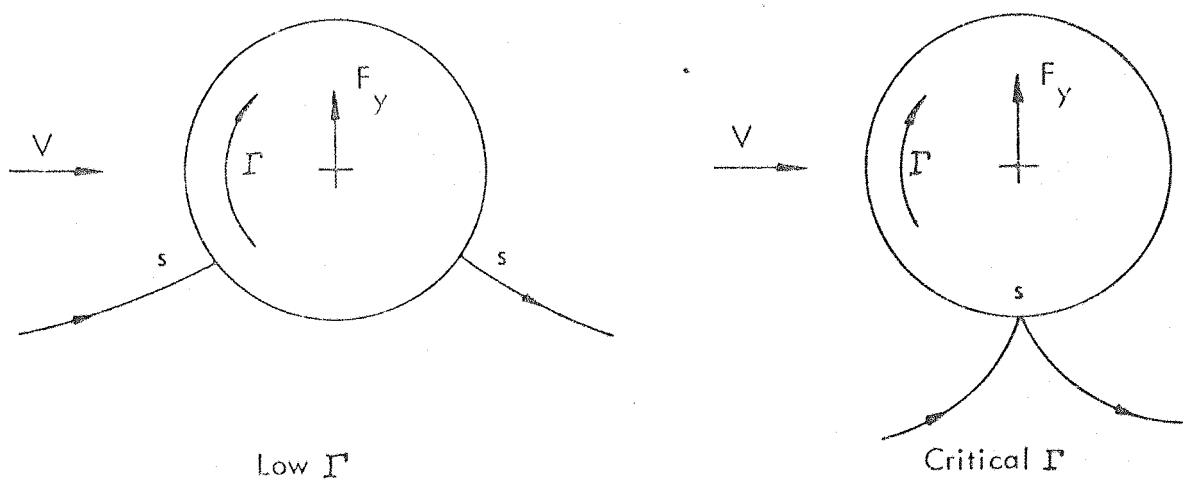

FIG. 5.1. THE EFFECT OF CIRCULATION ON THE POSITION OF THE STAGNATION POINTS ON THE 2 - DIMENSIONAL CYLINDER IN POTENTIAL FLOW.

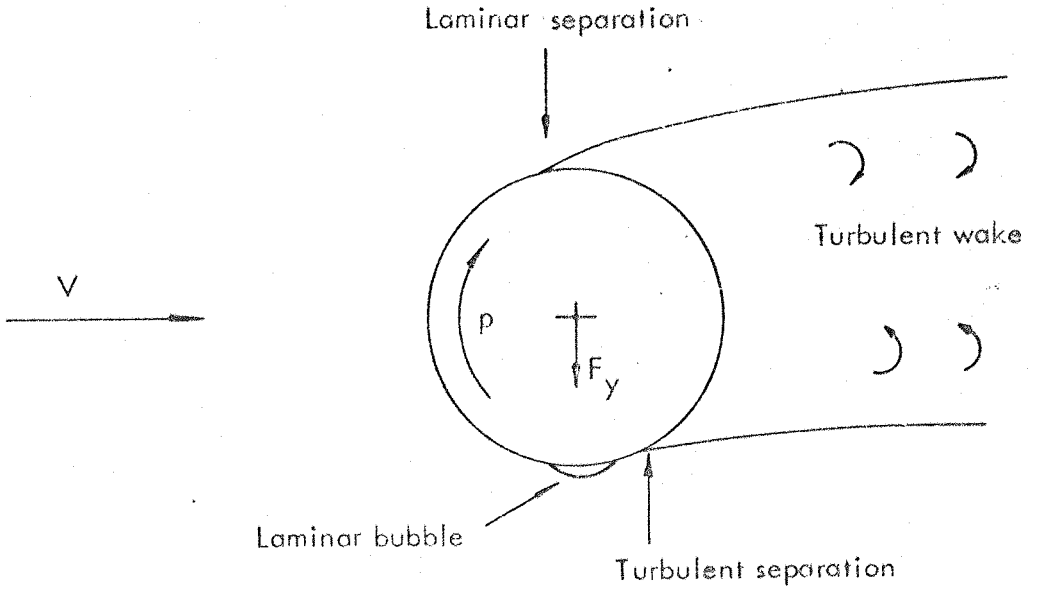

FIG. 5.2. OBSERVED FLOW PATERN AROUND A 2- DIMENSIONAL ROTATING CYLINDER FROM REFERENCE (4).

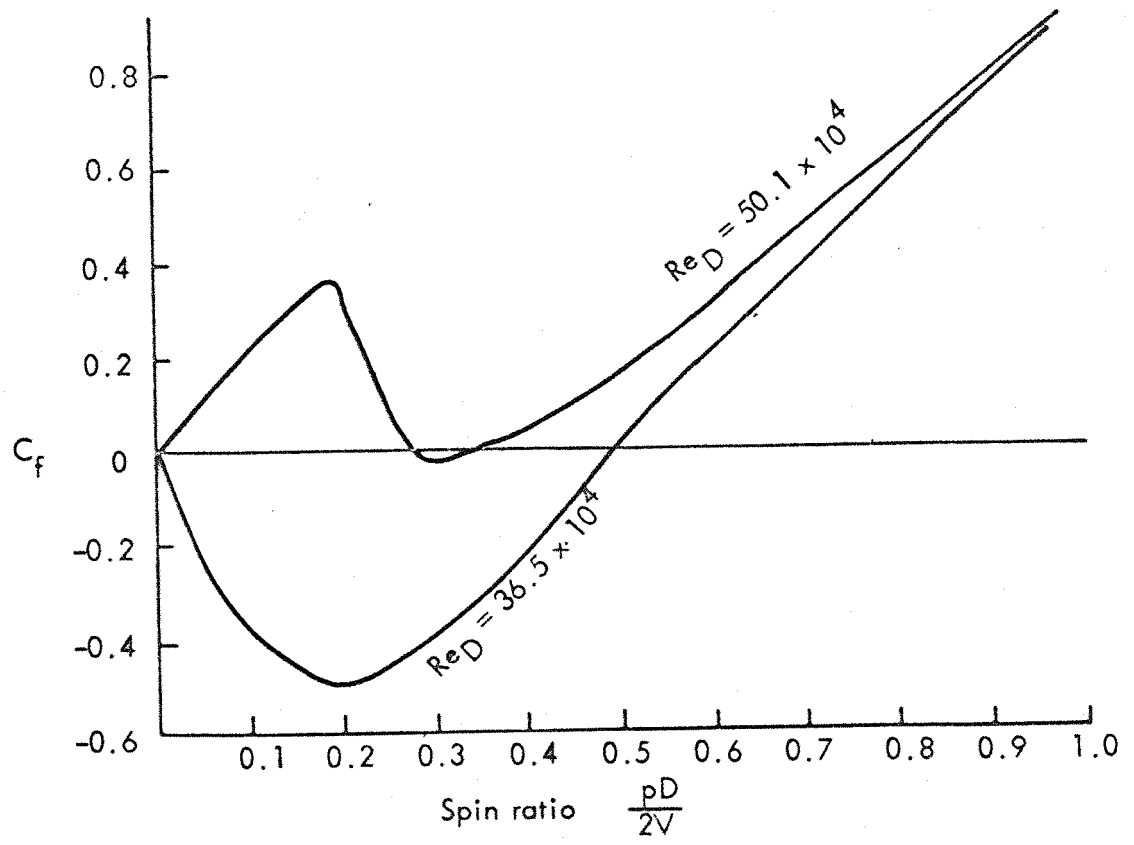

FIG. 5-3. MAGNUS LIFT ON A 2-DIMENSIONAL CYLINDER AFTER SWANSON [4].

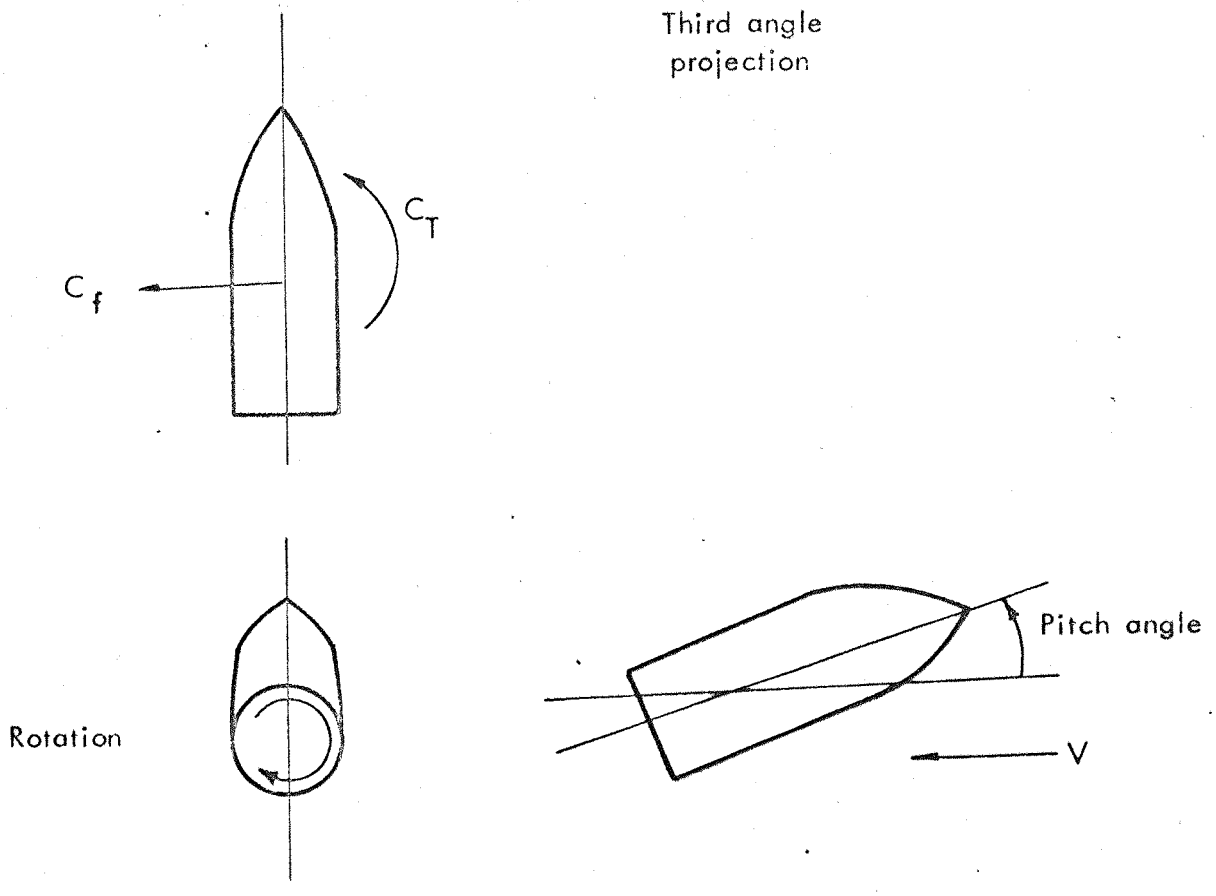

FIG. 5.4. CONVENTION FOR POSITIVE C_f AND C_T.

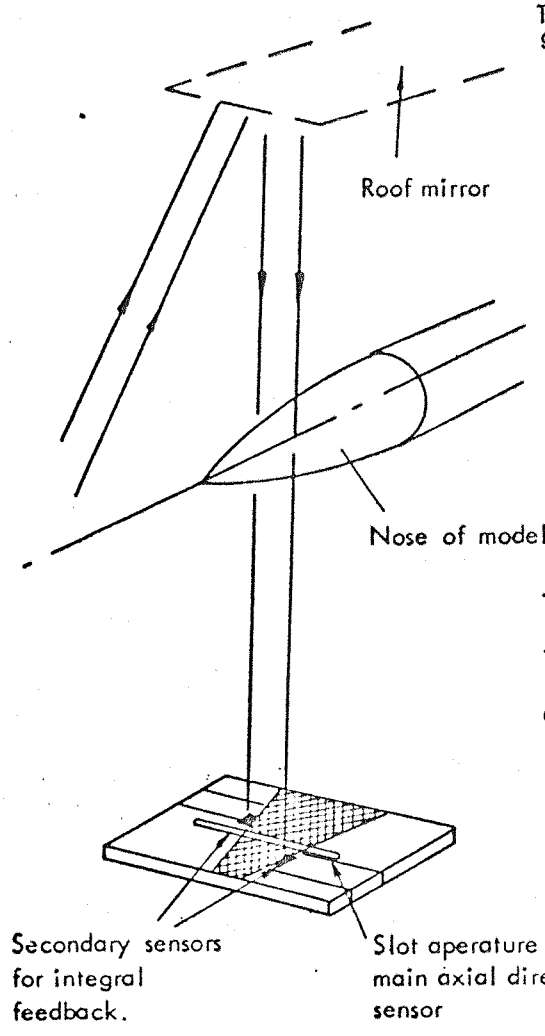

FIG. 6-1. PRECISION SENSING AT THE NOSE OF THE MODEL.

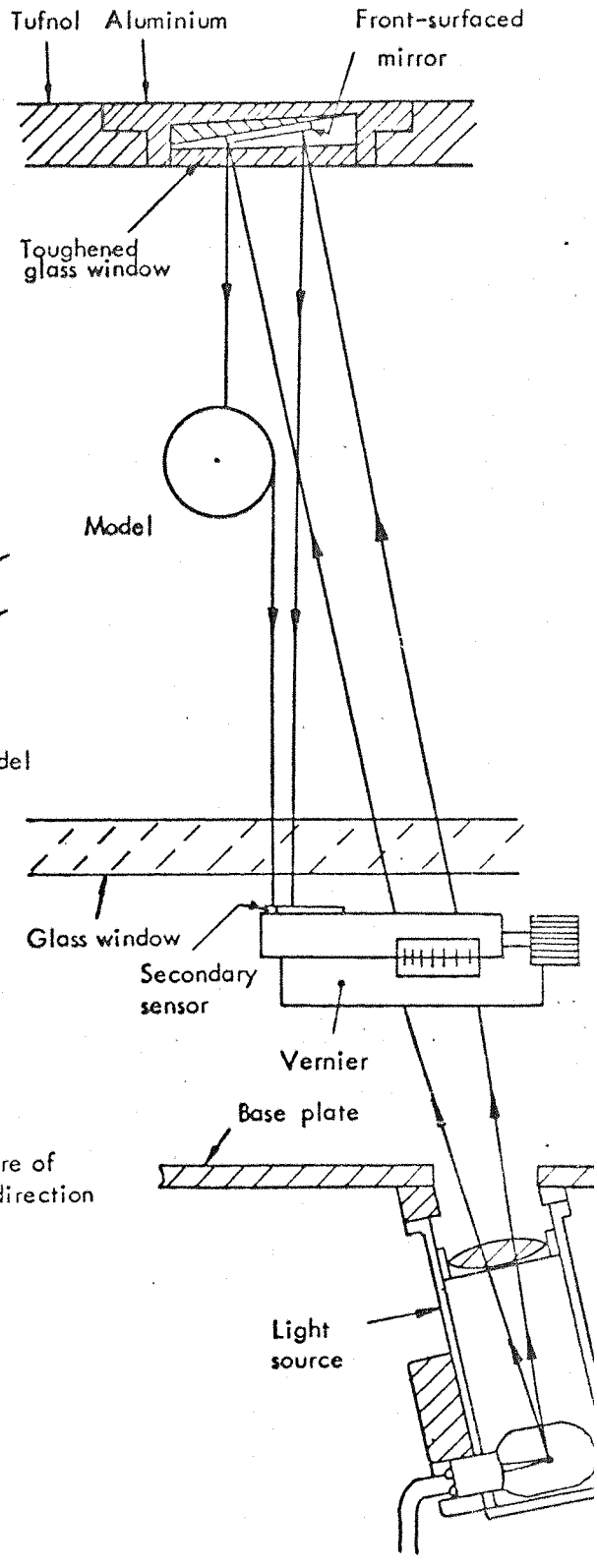

FIG. 6-2. PRECISION POSITION SENSING AT THE REAR OF THE MODEL.

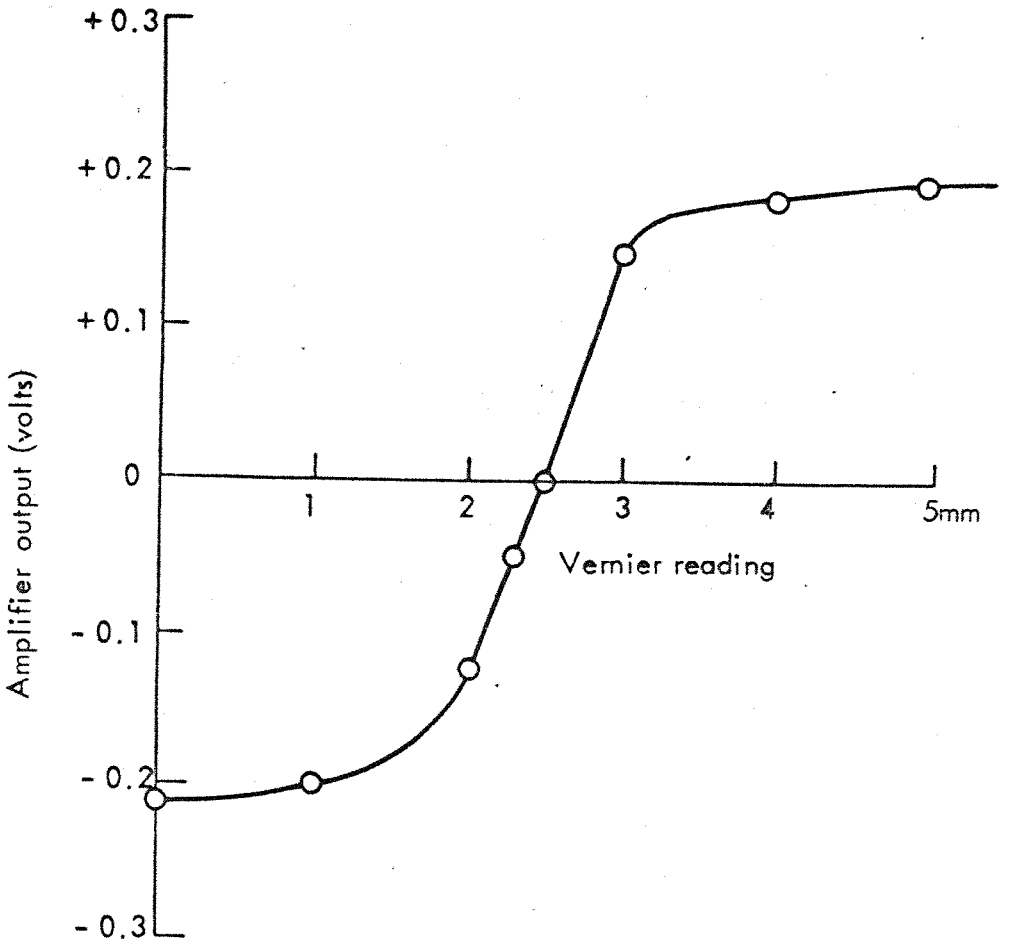

FIG. 6-3. THE VARIATION IN THE OUTPUT OF THE TAIL SECONDARY SENSOR AS A FUNCTION OF ITS LATERAL POSITION.

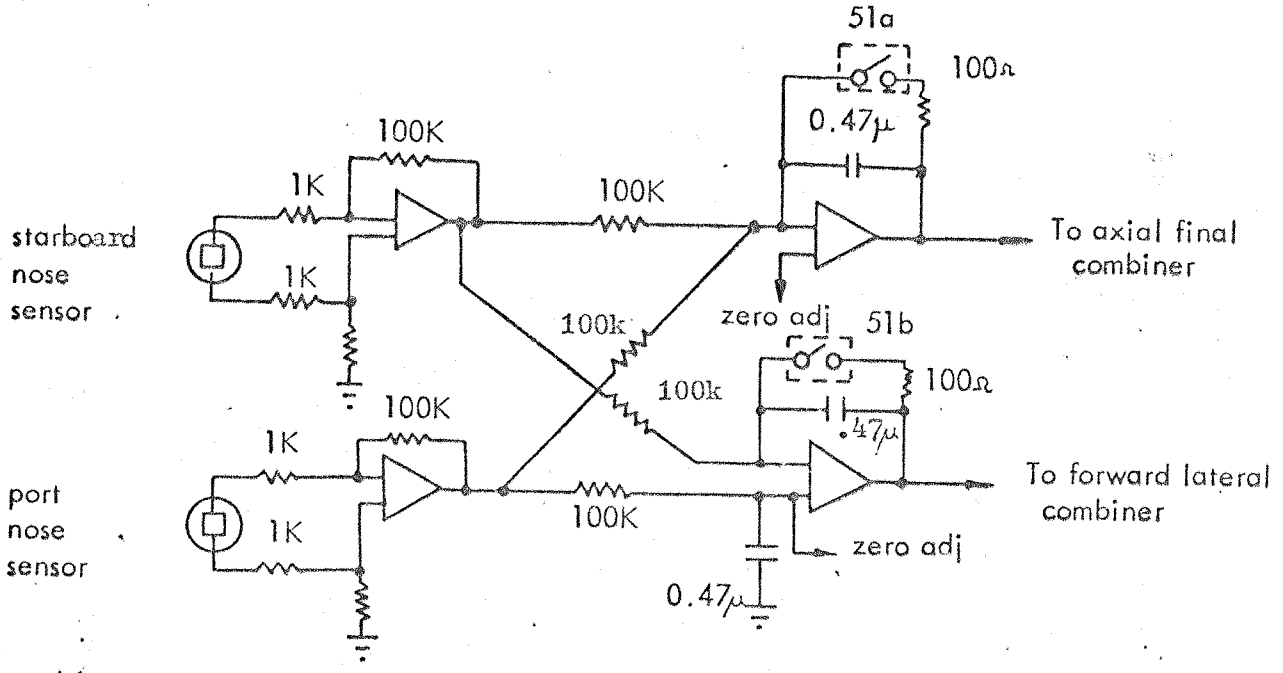

FIG.6-4. NOSE POSITION SENSORS AND INTEGRATORS.

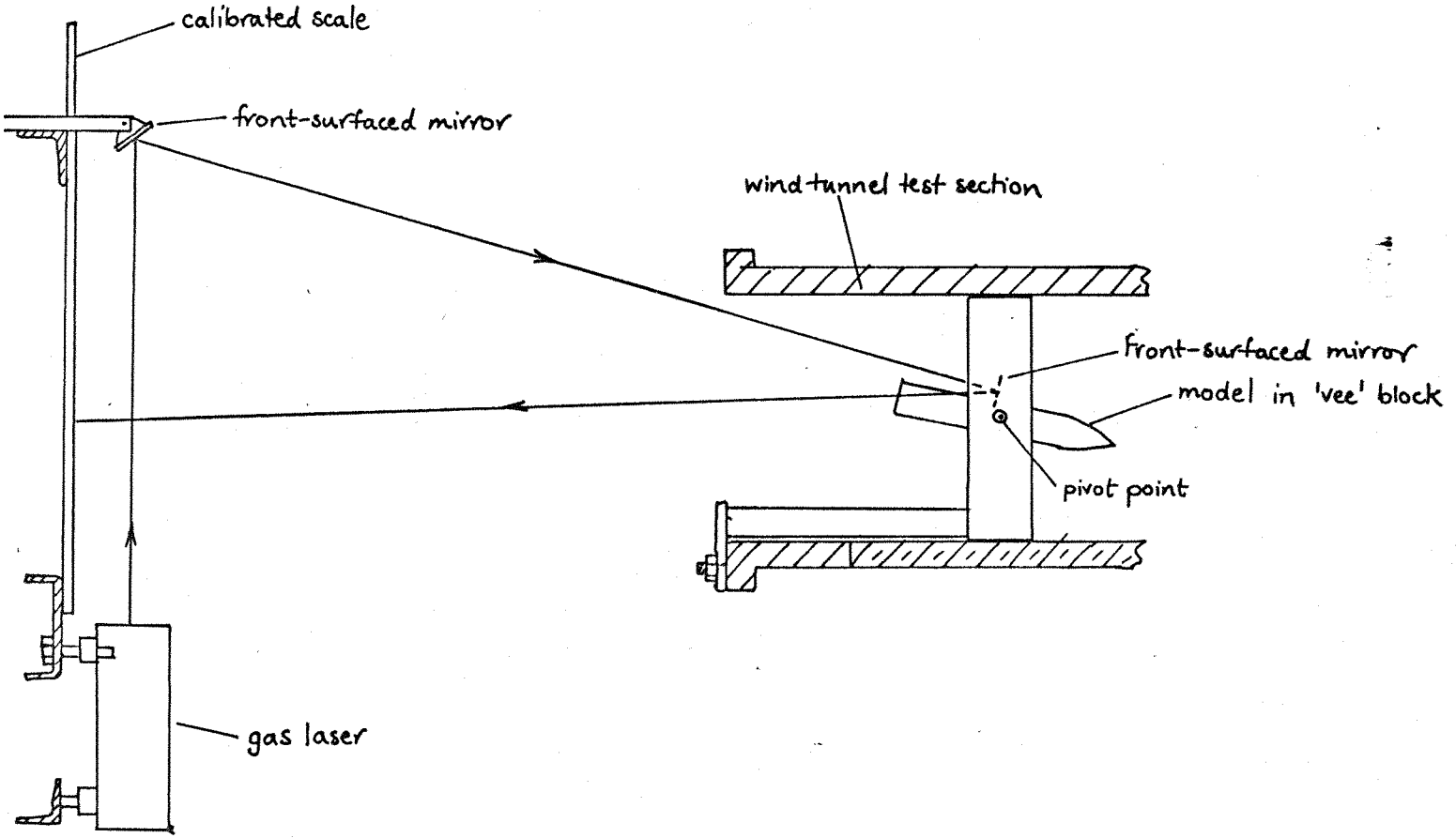

FIG. 6.5. PITCH ANGLE CALIBRATION ARRANGEMENT.

THE PORTION OF THE RETURN CIRCUIT BETWEEN TEST SECTION AND INJECTORS IS REMOVED TO ALLOW ACCESS.

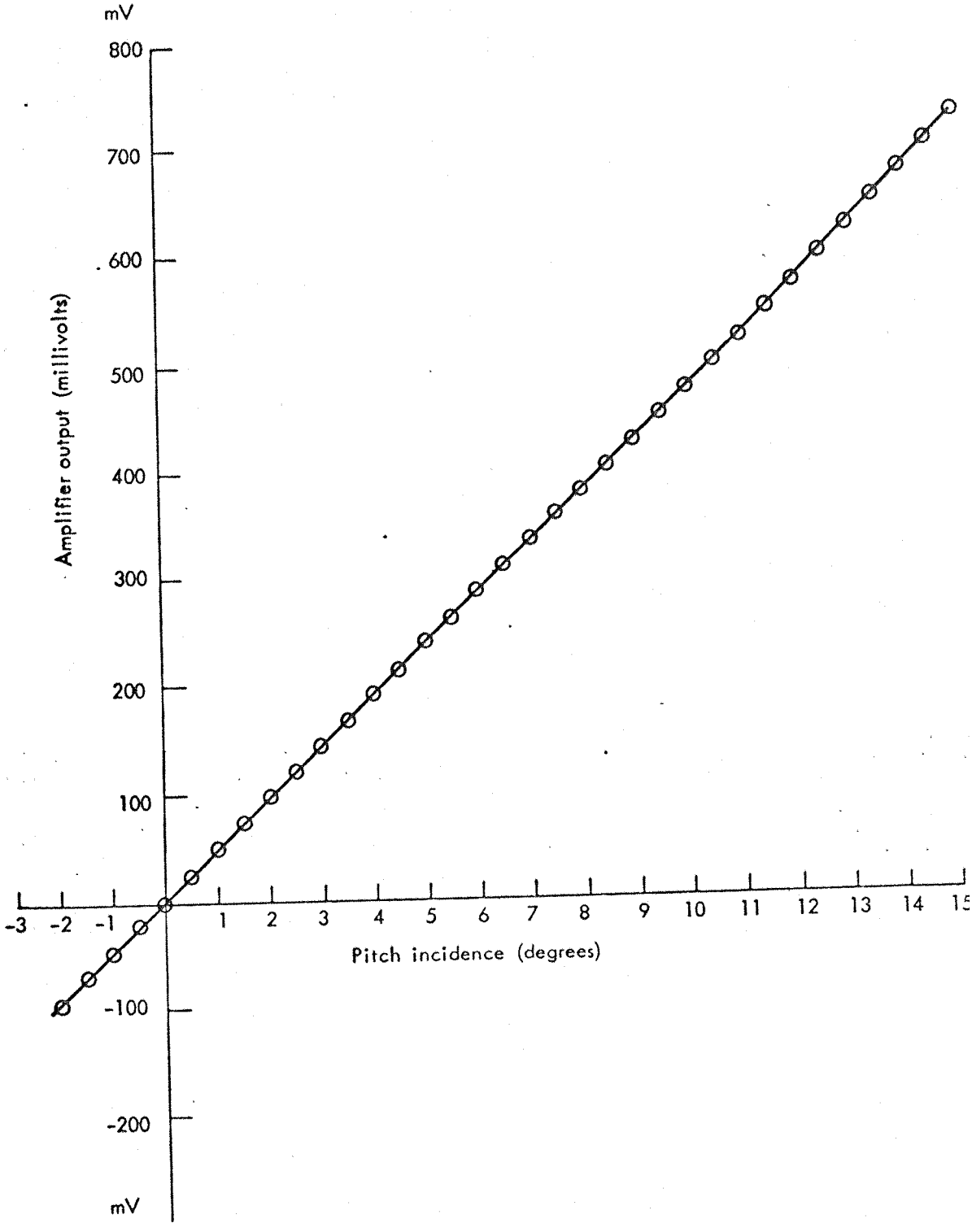

FIG. 6-6 OUTPUT OF THE PITCH SIGNAL AMPLIFIER AS A FUNCTION OF PITCH ANGLE.

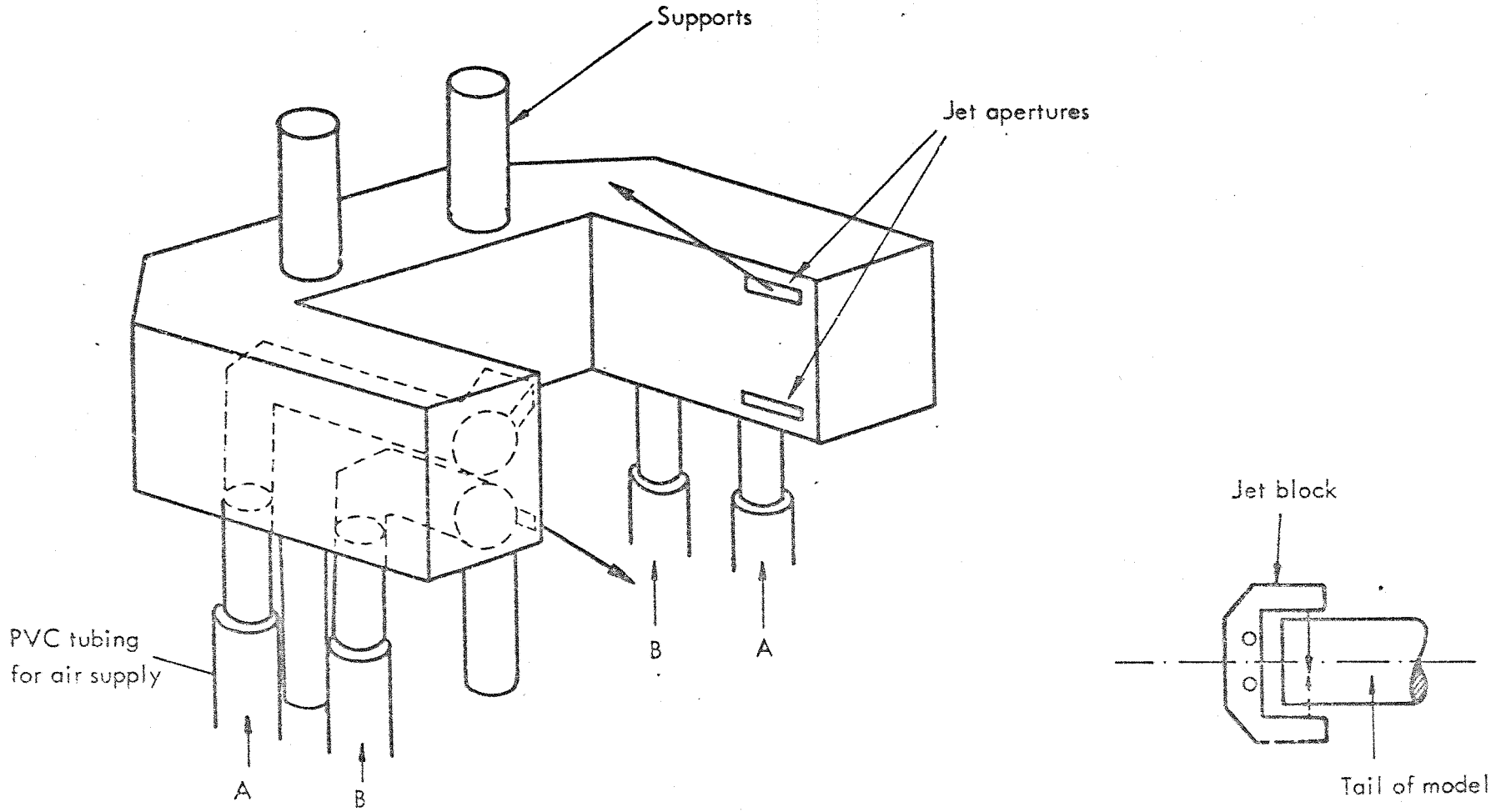

FIG. 6.7 JET BLOCK DETAILS. COMPRESSED AIR IS INTRODUCED INTO THE TUBES MARKED 'A' FOR ANTICLOCK -WISE ROTATION OF THE MODEL, AND INTO 'B' FOR CLOCKWISE ROTATION. INSET: VIEW FROM ABOVE, WITH MODEL IN POSITION.

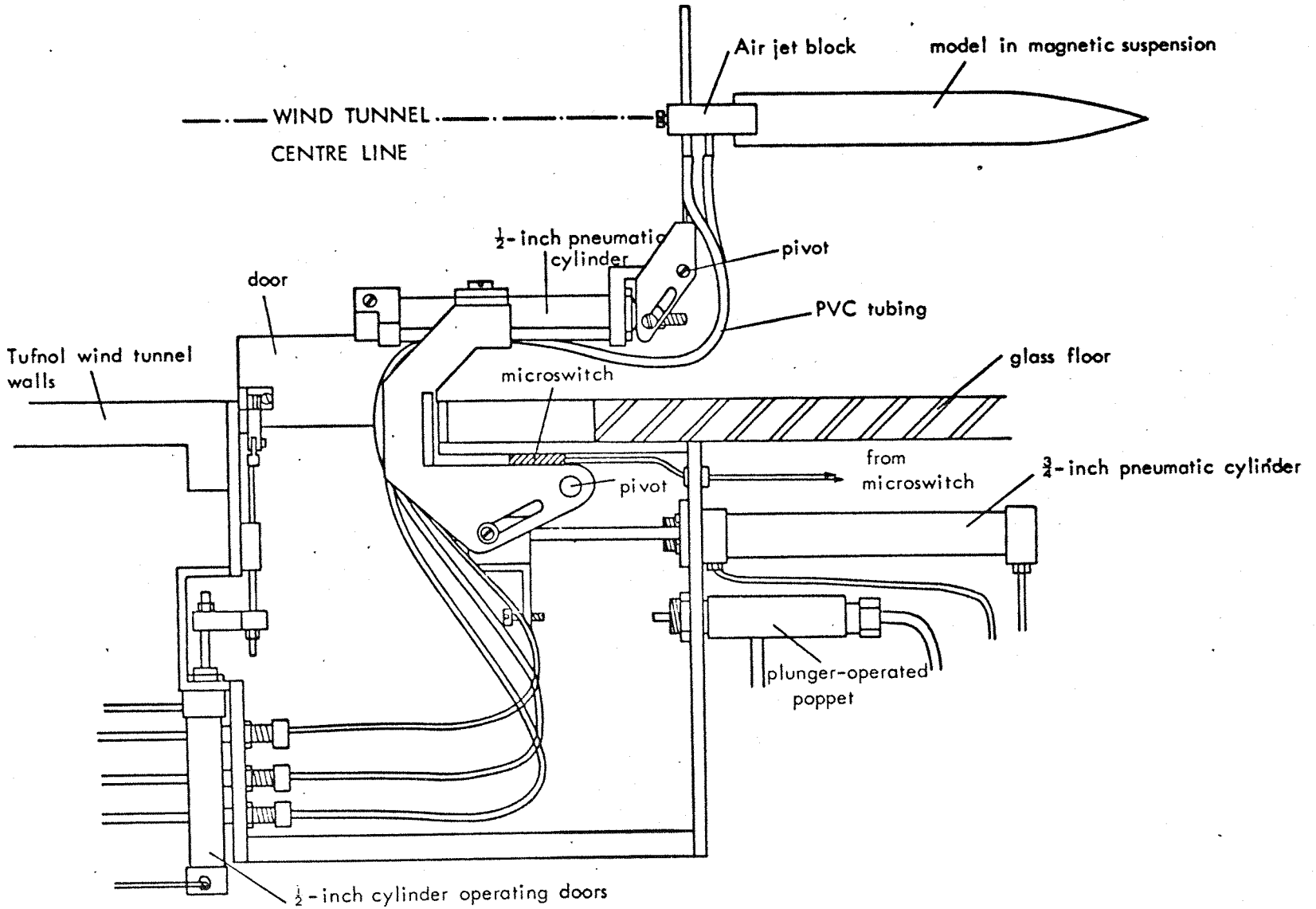

FIG 6.8 THE SPINNING MECHANISM, SHOWN WITH ONE SIDE OF THE CASE REMOVED.

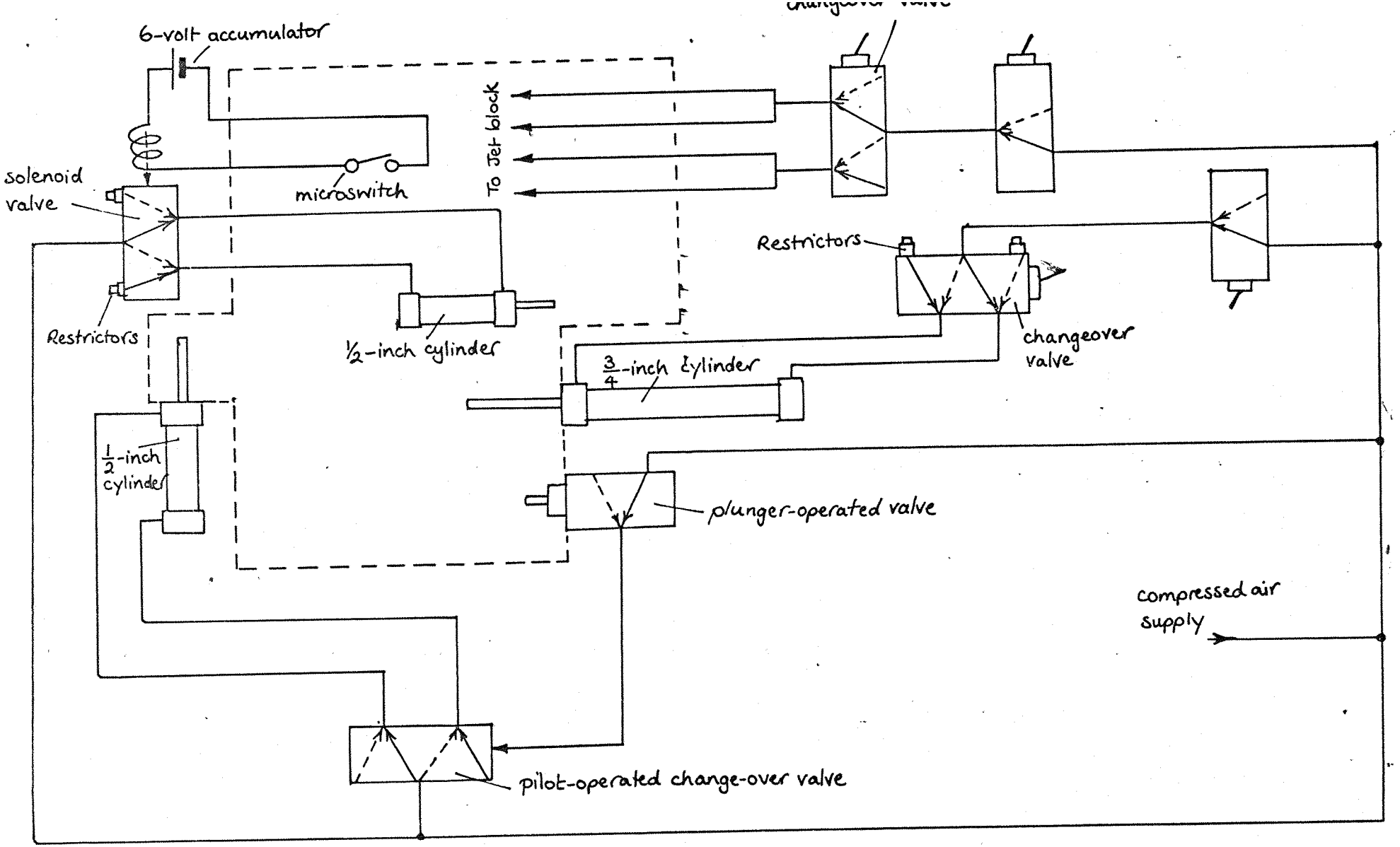

FIG 6.9 SCHEMATIC OF THE PNEUMATIC CIRCUIT USED TO OPERATE THE RETRACTION MECHANISM.

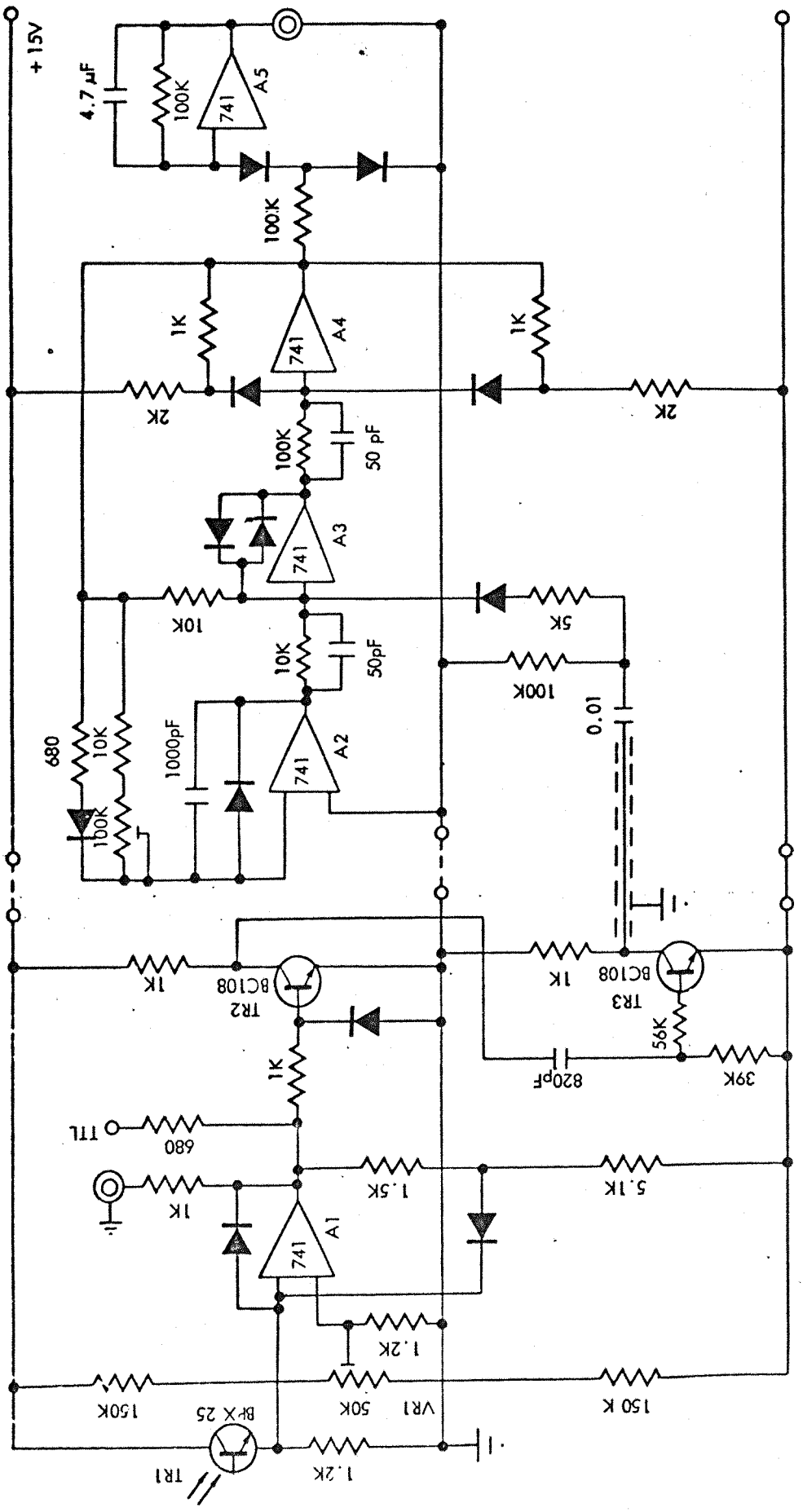

FIG.6.10 CIRCUIT DIAGRAM OF PULSE AMPLIFIER AND TACHOMETER.

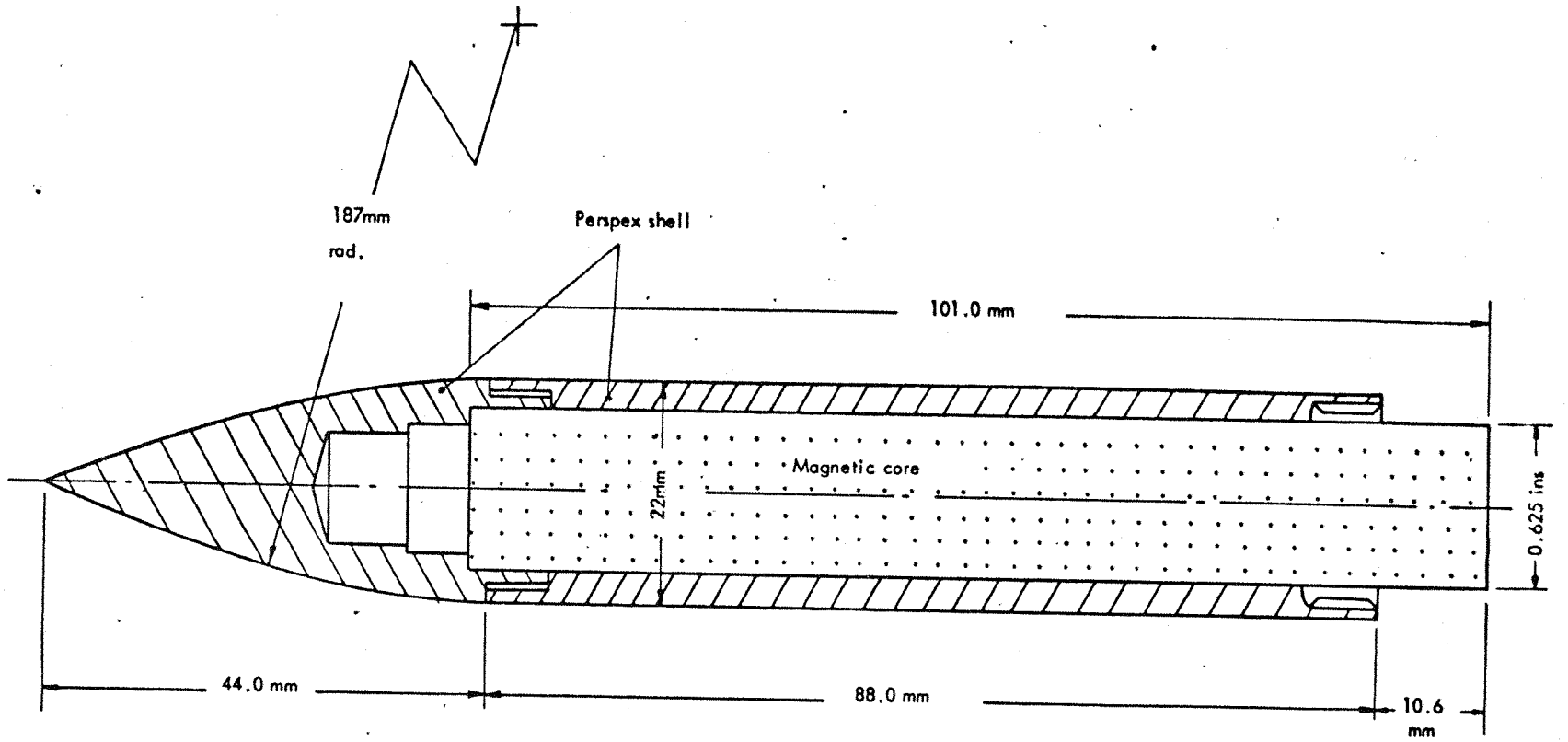

FIG 6.11 CROSS - SECTION THROUGH THE 7-CALIBRE MODEL. THE BASE IS NOT SHOWN.

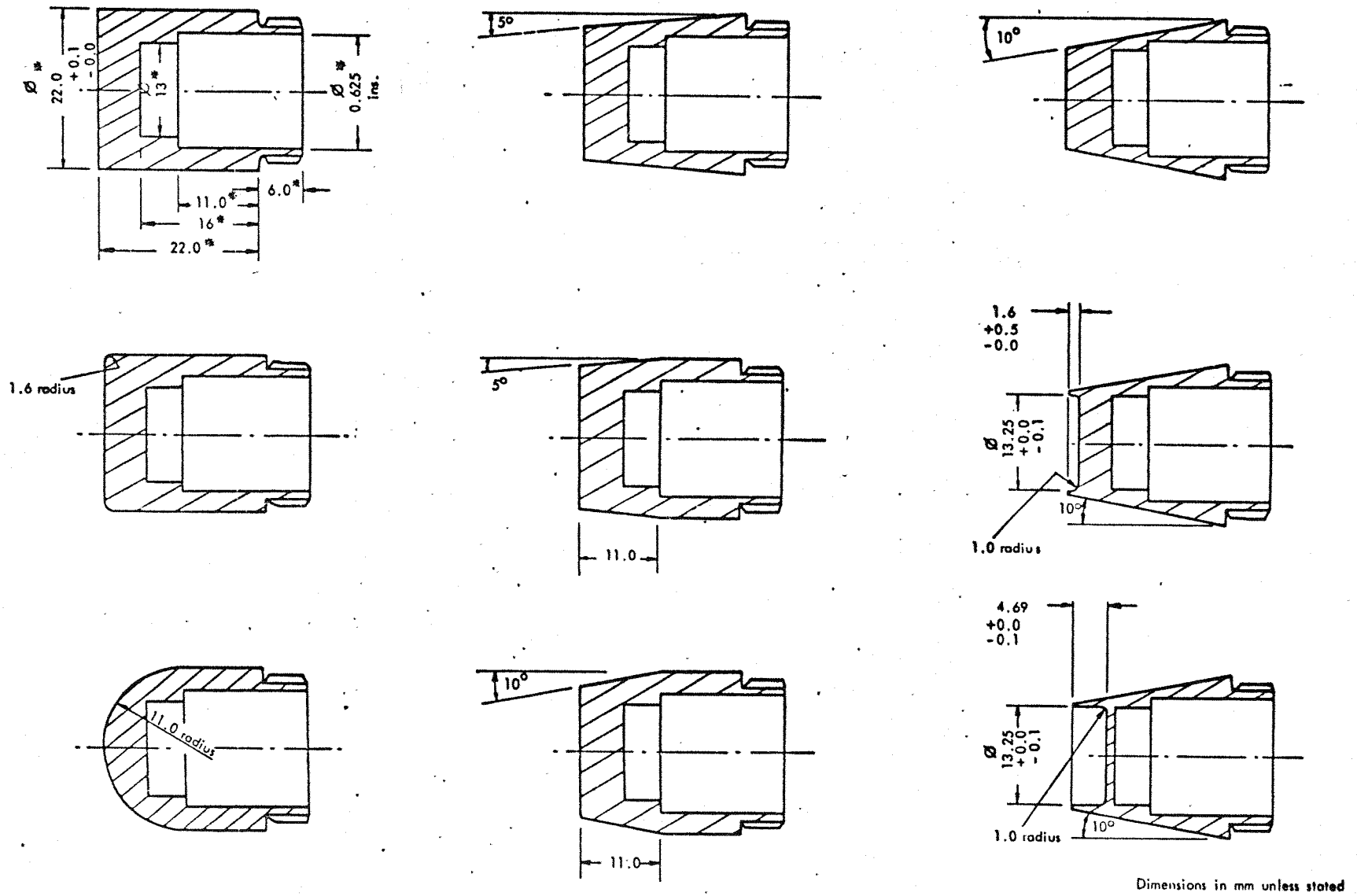

Dimensions in mm unless stated otherwise.

*: common dimension.

Fig. 6.12 .THE 9 BASE SHAPES USED IN THE MAGNUS TESTS.

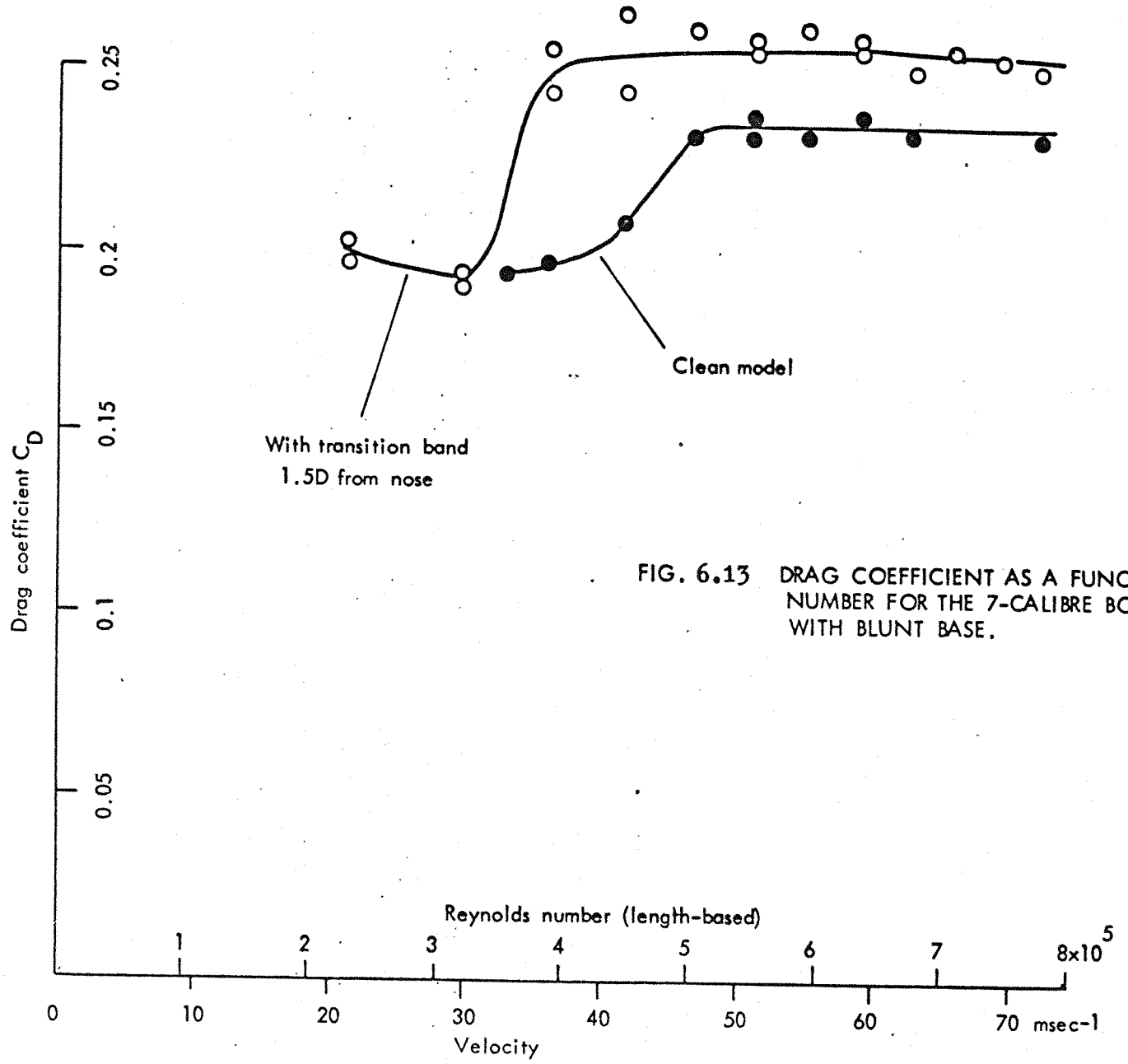

FIG. 6.13 DRAG COEFFICIENT AS A FUNCTION OF REYNOLDS NUMBER FOR THE 7-CALIBRE BODY OF REVOLUTION WITH BLUNT BASE.

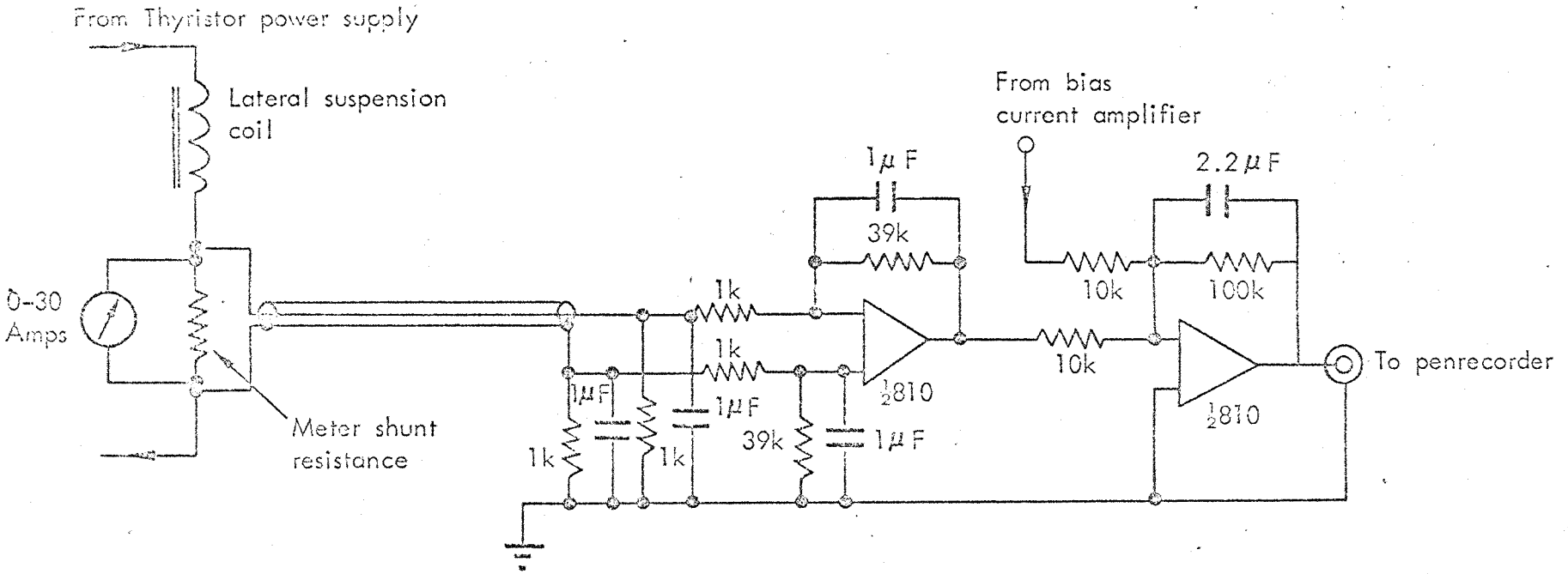

FIG. 6.14 CIRCUIT OF A TYPICAL CURRENT SIGNAL AMPLIFIER

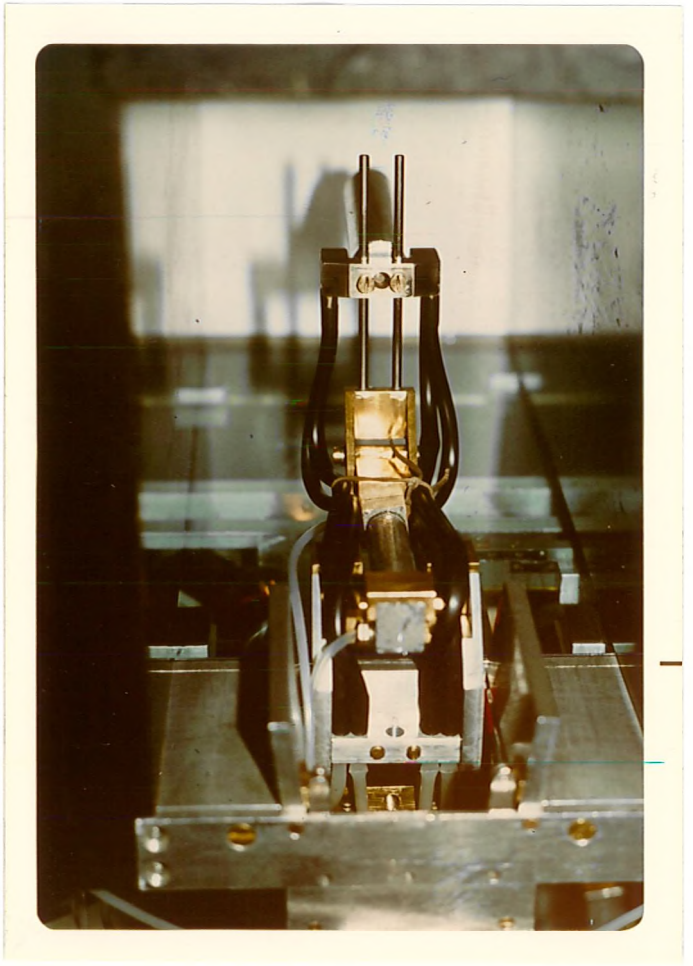

(a)

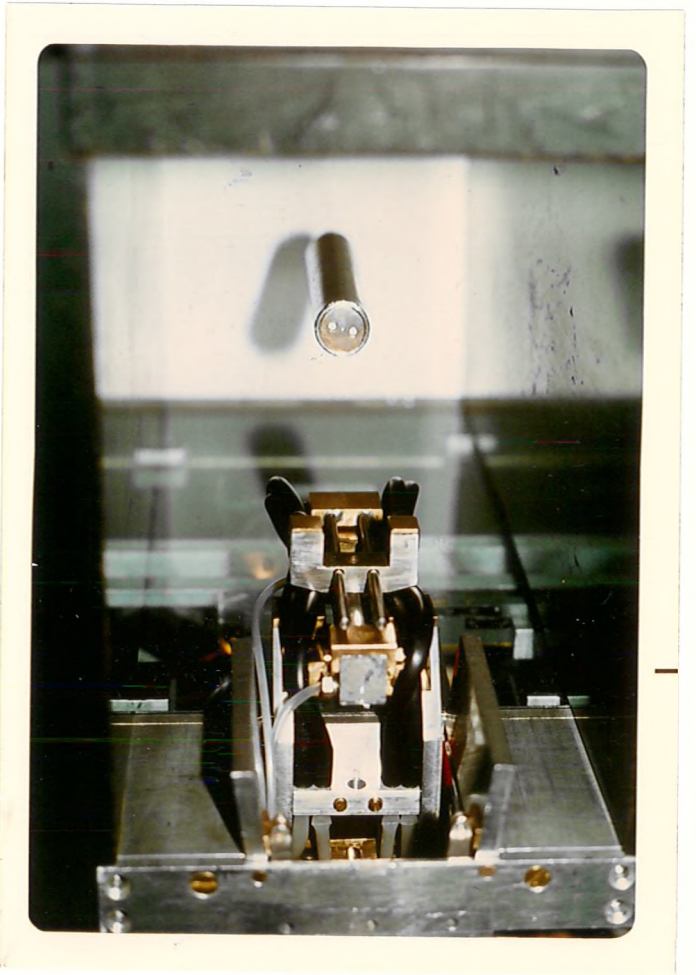

(b)

FIGURE 6.15. Photographs showing the air-jet spinning device and retraction mechanism. The model in magnetic suspension is the 7 calibre AN spinner constructed in aluminium.

(a) The position during spin-up of the model.

(b) First stage of retraction. Upper section folded down.

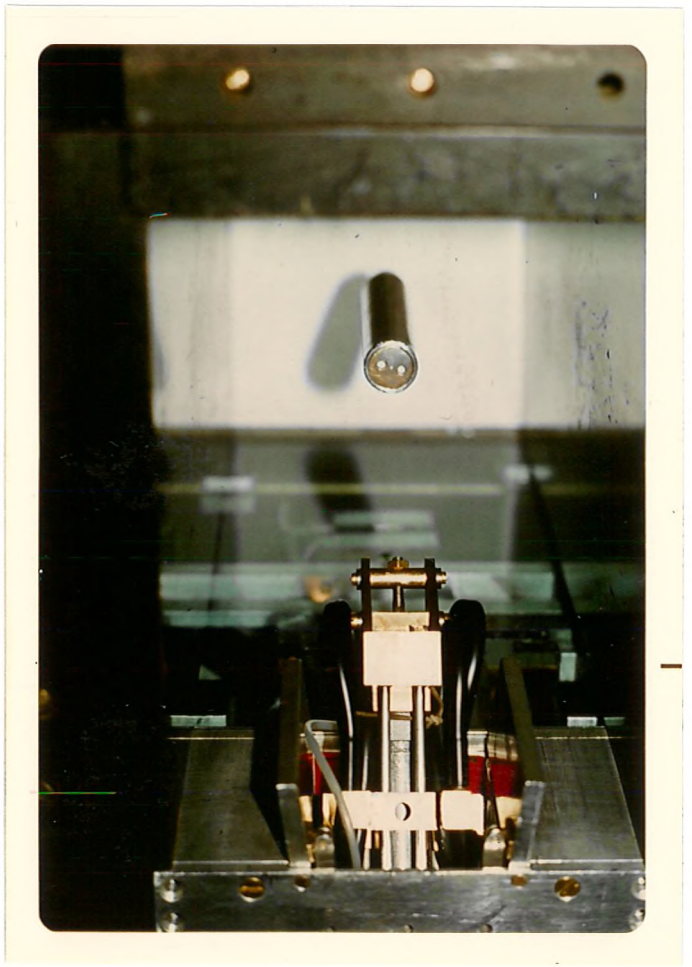

(c)

(d)

FIGURE 6.15 (continued). The air-jet spinning device and retraction mechanism.

(c) The mechanism in the process of retracting into the tunnel floor.

(d) The final appearance. The movable arm has retracted fully and caused the doors to close over the aperture in the floor.

FIGURE 6.16 (overleaf). A photograph of the model used in the Magnus force and moment measurements, with the interchangeable bases.

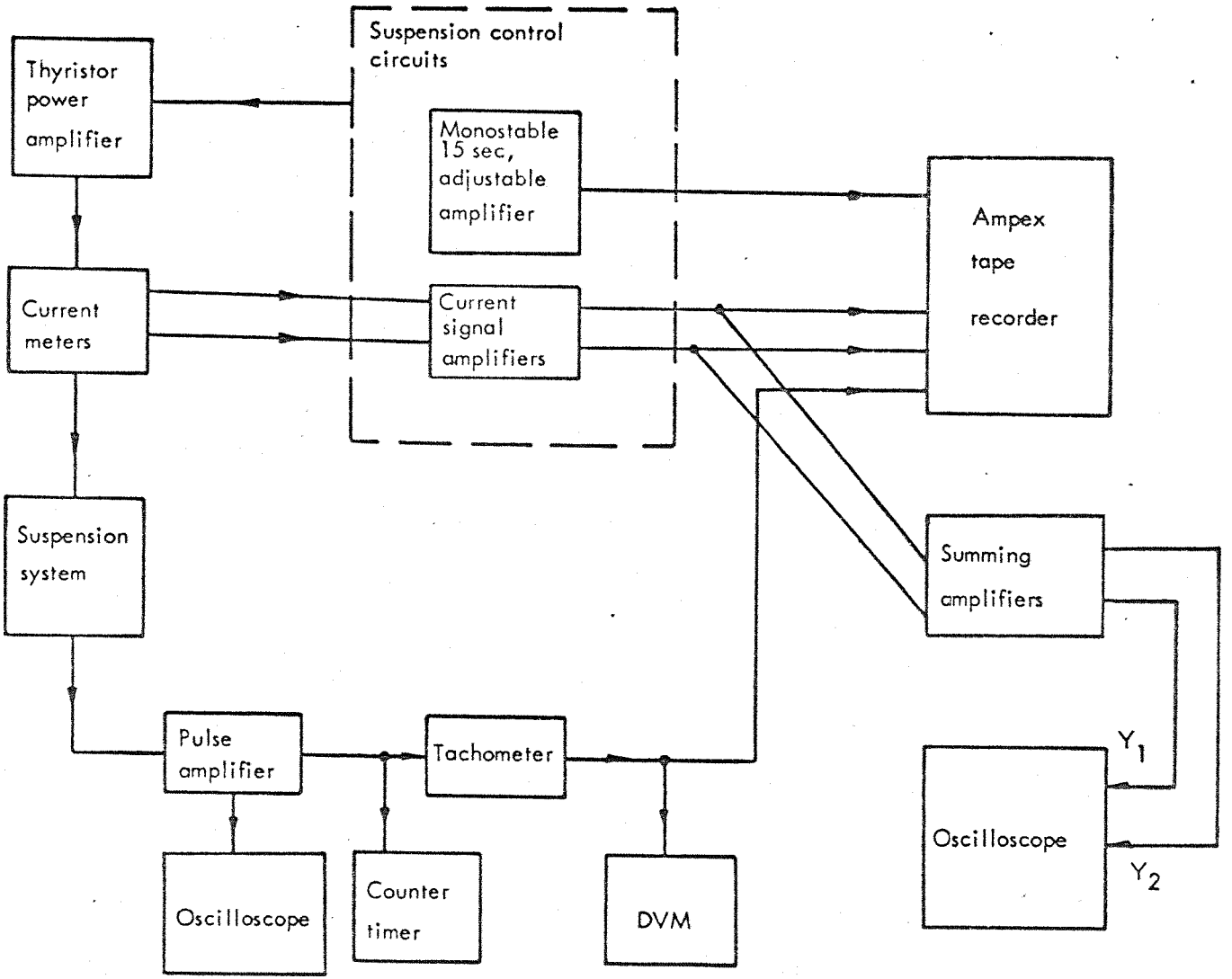

FIG. 7-1. BLOCK DIAGRAM OF DATA ACQUISITION SYSTEM.

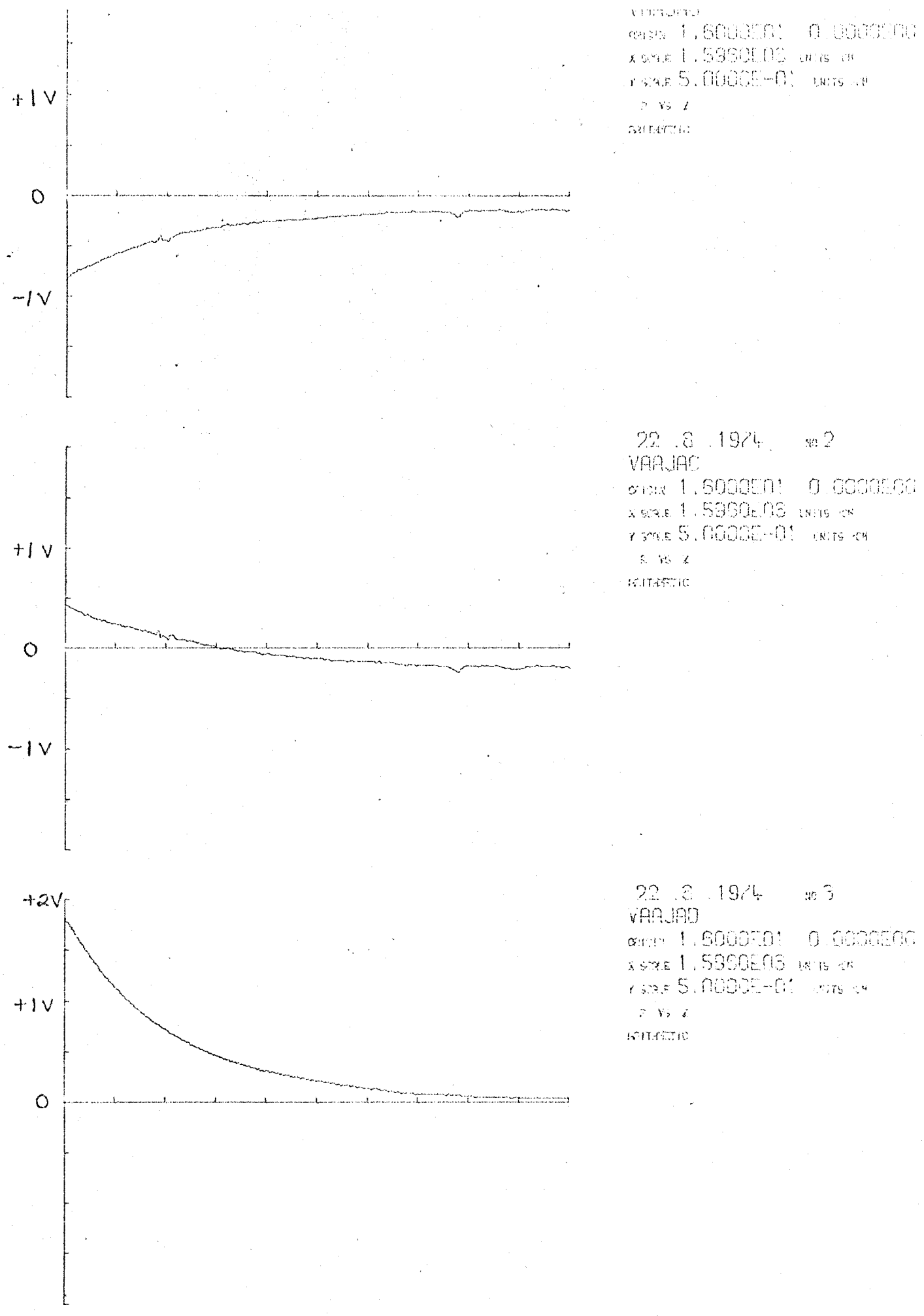

FIGURE 7-2. OUTPUT OF 'MAG1' FOR THE BASIC SPINNER AT 0^{o} INCIDENCE

TOP: e_1 CENTRE: e_2 BOTTOM: TACHOMETER OUTPUT. ALL AGAINST TIME.

```
£DATA MAG1

/INUM(NS)
/INUM(X,Y)
DO1 I←X,Y
/KILL("A","B","C","D","E","LD")
/ACQUIRE("A",NS,125,2,1000)
/CONV("A","B",5)
/SHORTRMS("B","C",5,5,0)
/CONV("C","D",4)
/ARITH("D","E",13,*1)
/CRN(I,A)
/ARITH("E",A,15,*1)
1/PLOT(A,10,8,*0,#122,2.0,-2.0)
/KILL("A","B","C","D","E")
IF(Y<3)GOTO2
/FUNCTION("AD","LD",3)
/PLOT("LD",10,-0.5,*0,#120)
/KILL("LD")
2END

£END
```

FIGURE 7.3 THE MYRIAD PROGRAM 'MAG1'. THIS PROGRAM RECONVERTS THE TAPE RECORDED DATA INTO ABSOLUTE VALUES, USING THE OUTPUT OF THE PROGRAM 'ONE'.

```
£DATA MAG2

/KILL("X","Y","Z","A","B","CP","CY","N","P","S","T")
/RNUM(U,QS,QSD)
/ARITH("AD","S",14,200.0)
/CONV("S","T",2)
/CONV("T","N",1,*0,9)
/ARITH("N","P",19,U)
/KILL("N","S","T")
DO 1 I←0,1
IF(I)0,0,2
V1←5.96
V2←-5.93
V3←QS
V4←-0.01
GOTO 3
2 V1←30.5
V2←23.6
V3←QSD
V4←-0.025
3/ARITH("AB","X",14,V1)
/ARITH("AC","Y",14,V2)
/ARITH("X","Z",4,"Y")
J←I+16
/CRN(J,A)
/ARITH("Z",A,15,V3)
/CONV(A,"CY",2,*0,9)
/ARITH("CY","CP",8,"P")
/PLOT("CP",-0.025,V4,*0,#100)
1/KILL("X","Y","Z","CP","CY")

/KILL("BA","BB","A","B","P","XCP")
END

£END
```

FIG. 7.4 MYRIAD PROGRAM 'MAG2'. USING THE OUTPUT OF 'MAG1', THIS PROGRAM PRODUCES THE PLOTS OF MAGNUS FORCE AND MOMENT COEFFICIENT VERSUS SPIN RATIO.

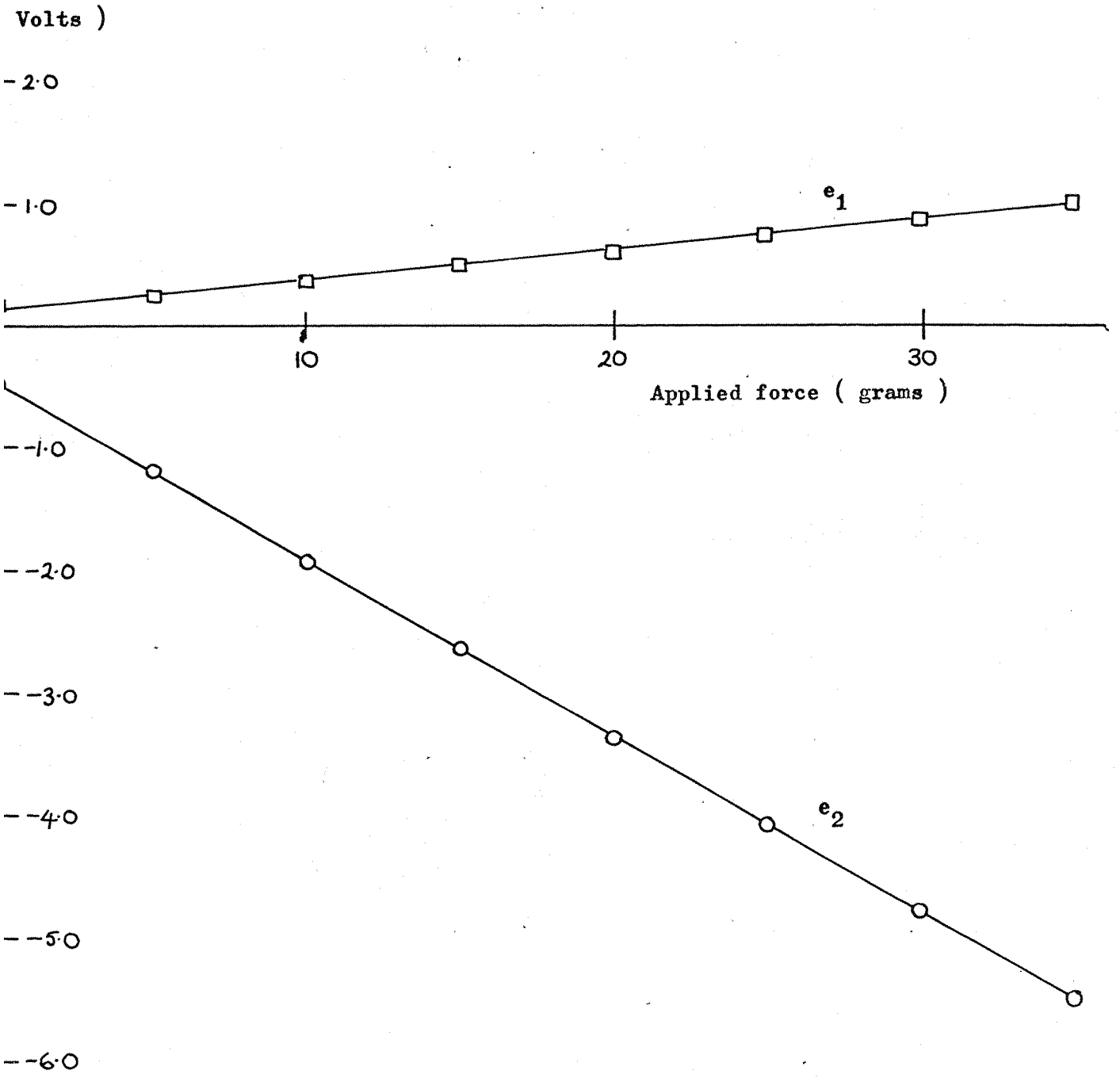

FIG. 7.5 Output of front (e_1) and rear (e_2) current signal amplifiers as a function of applied side force. Point of application was 26.3 mm upstream of moment reference centre.

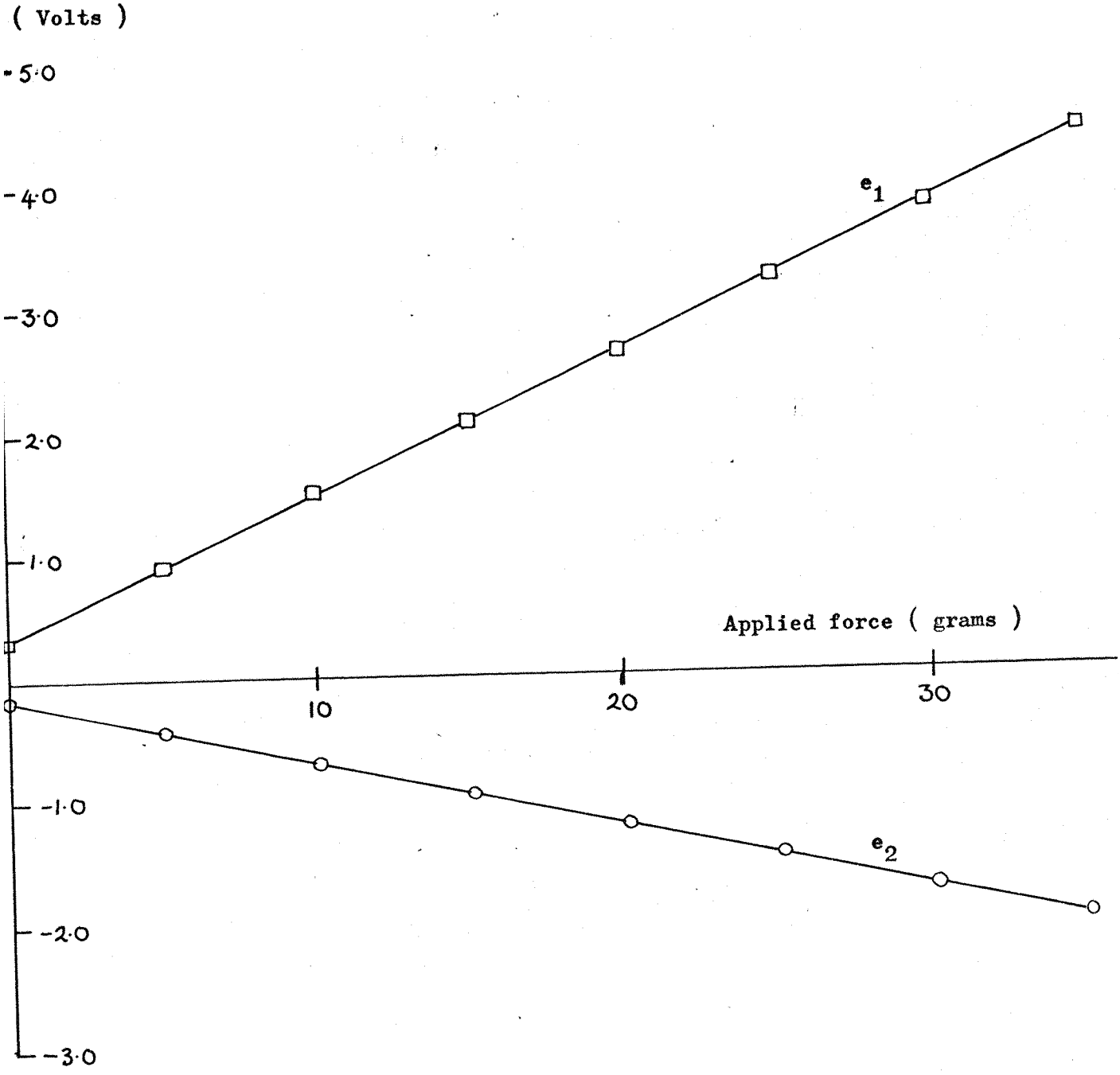

FIG. 7.6 Output of front (e_1) and rear (e_2) current signal amplifiers as a function of applied side force. Point of application was 22.4 mm down stream of moment reference centre.

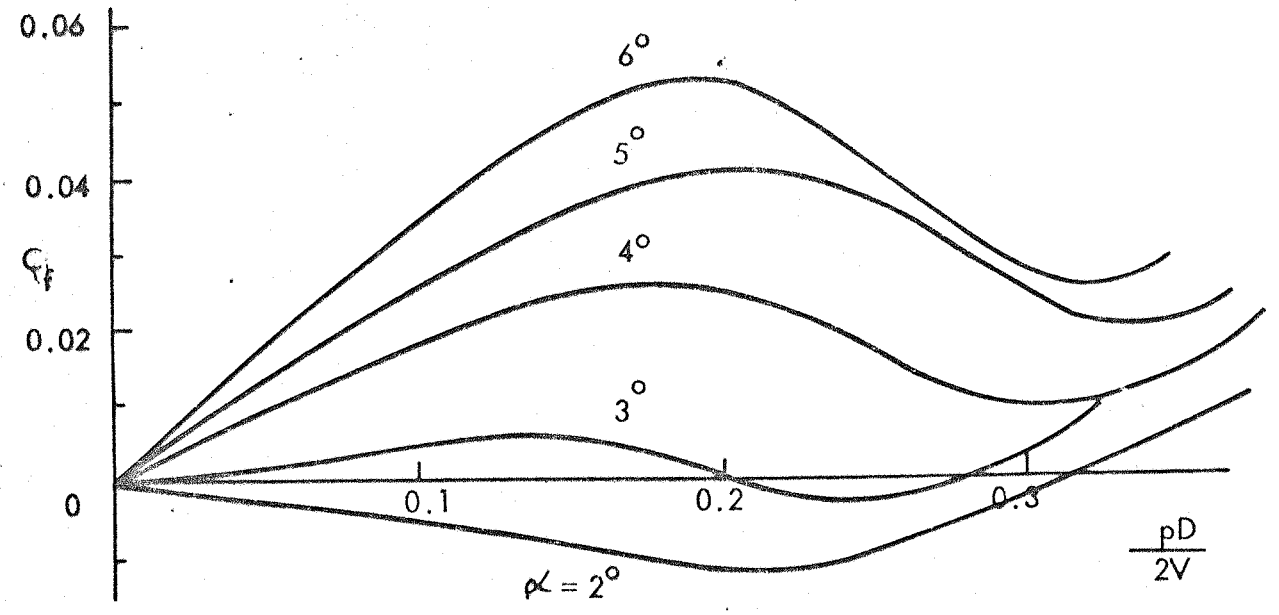

(b) Hemispherical base model with roughness.

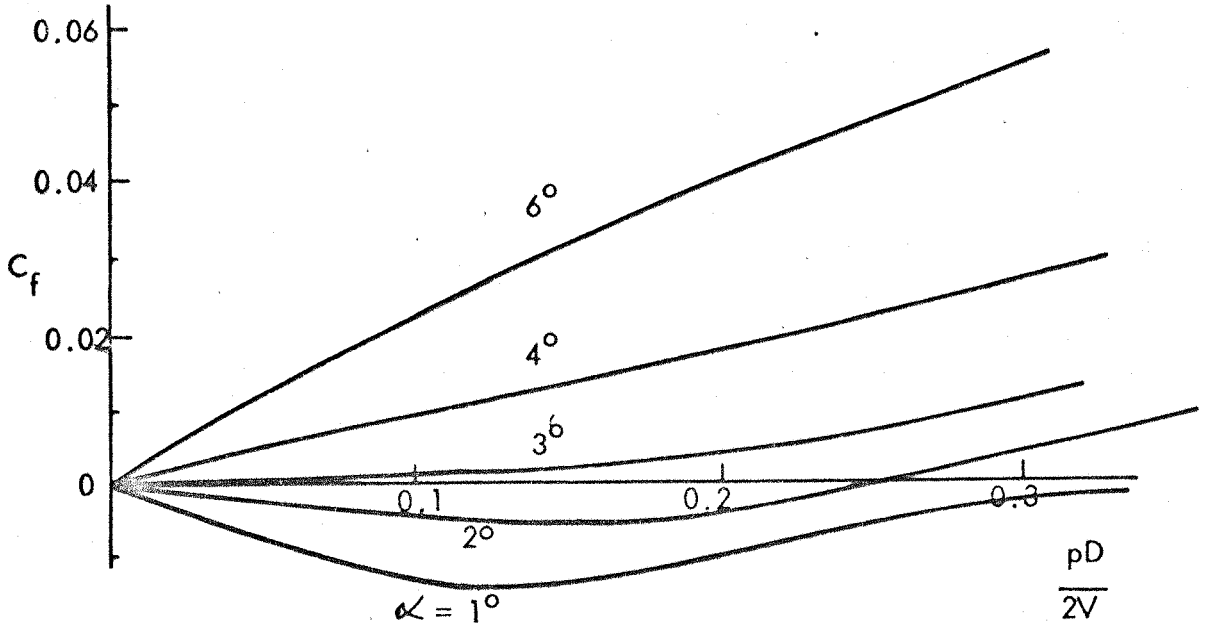

(a) Blunt base model with roughness

FIG. 8-1. VARIATION OF MAGNUS FORCE COEFFICIENT WITH SPIN RATIO AND INCIDENCE.

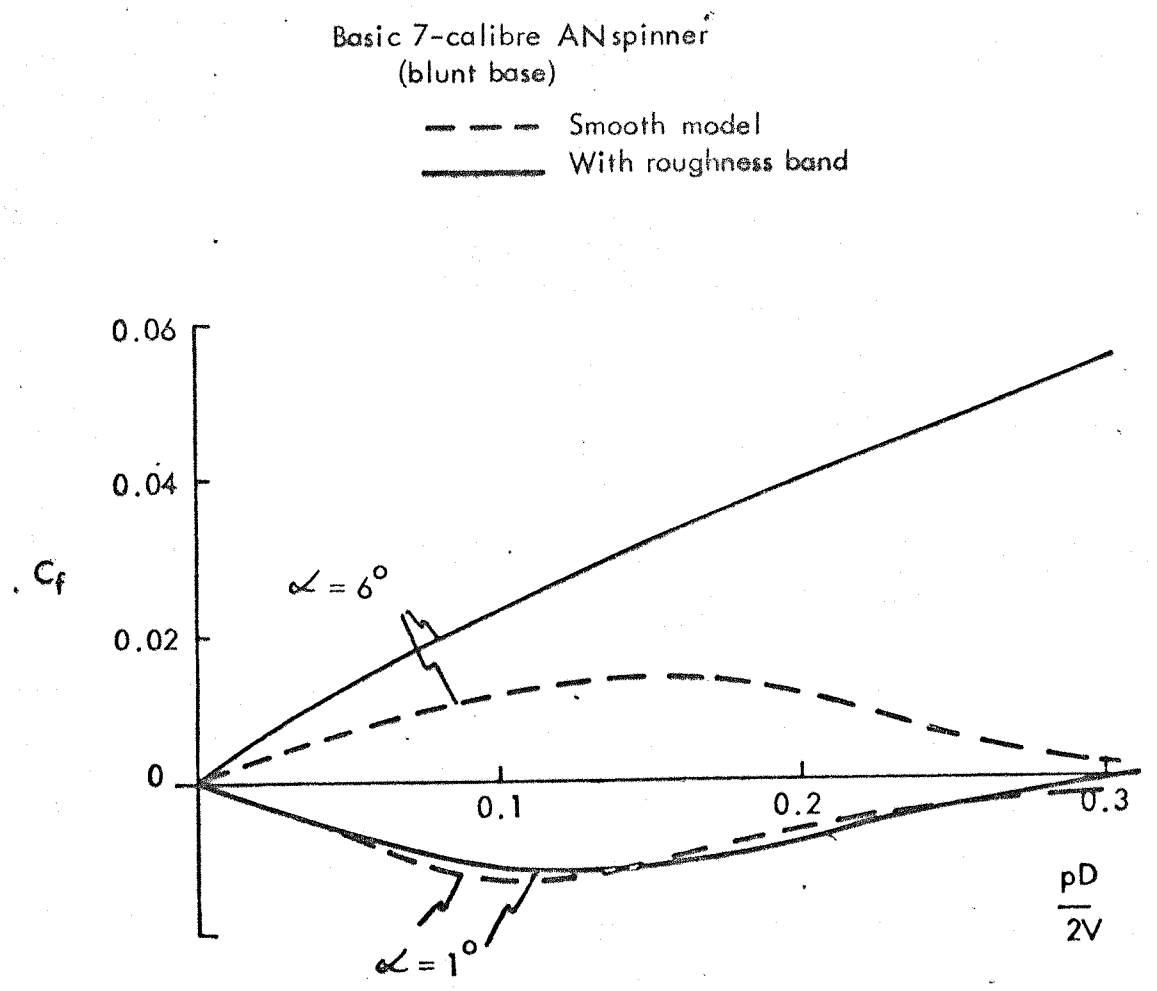

FIG. 8-2(a). EFFECT OF THE ADDITION OF A ROUGHNESS BAND TO THE BASIC SPINNER.

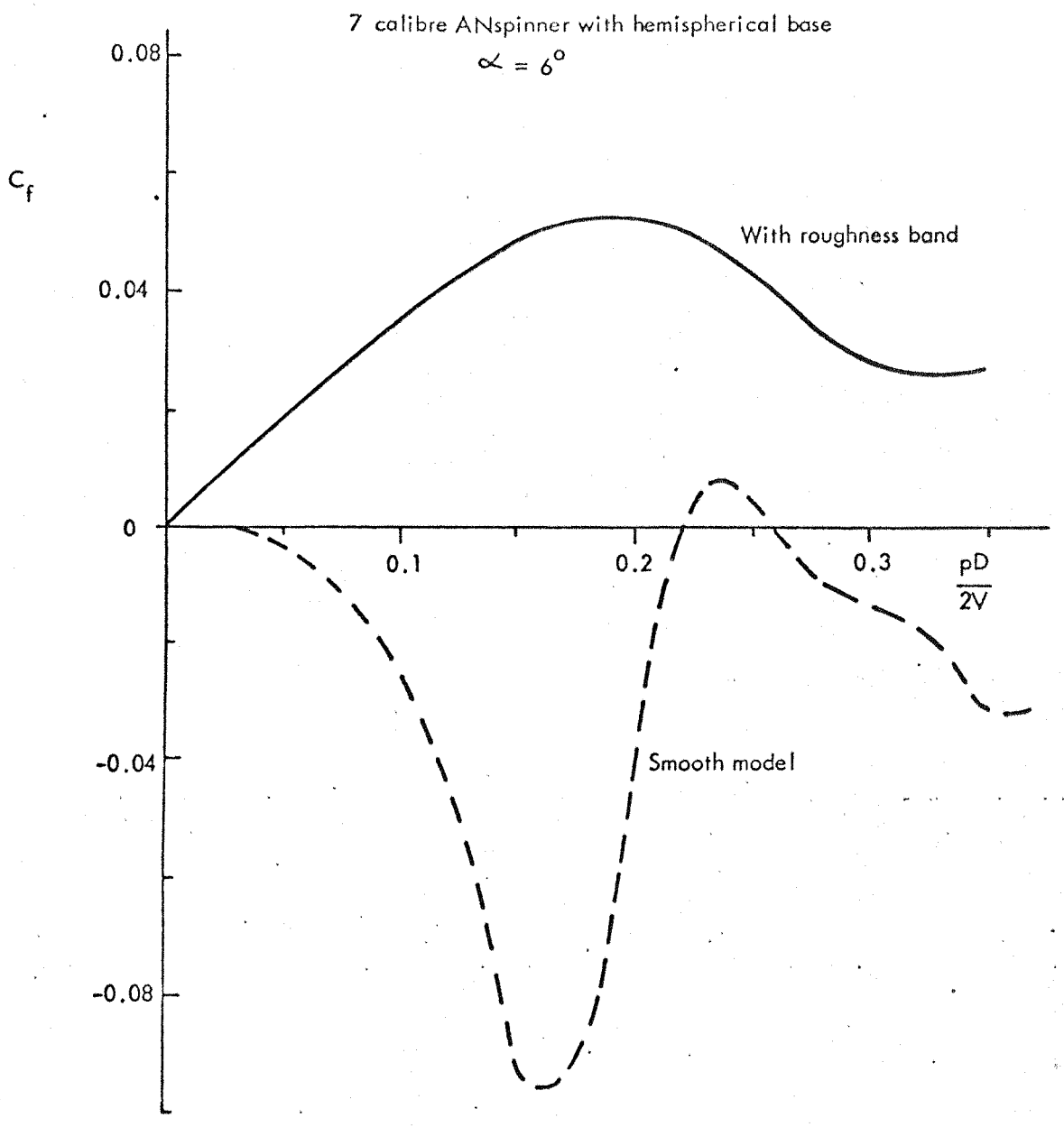

FIG. 8-2(b). EFFECT OF THE ADDITION OF A ROUGHNESS BAND TO THE SPINNER WITH HEMISPHERICAL BASE.

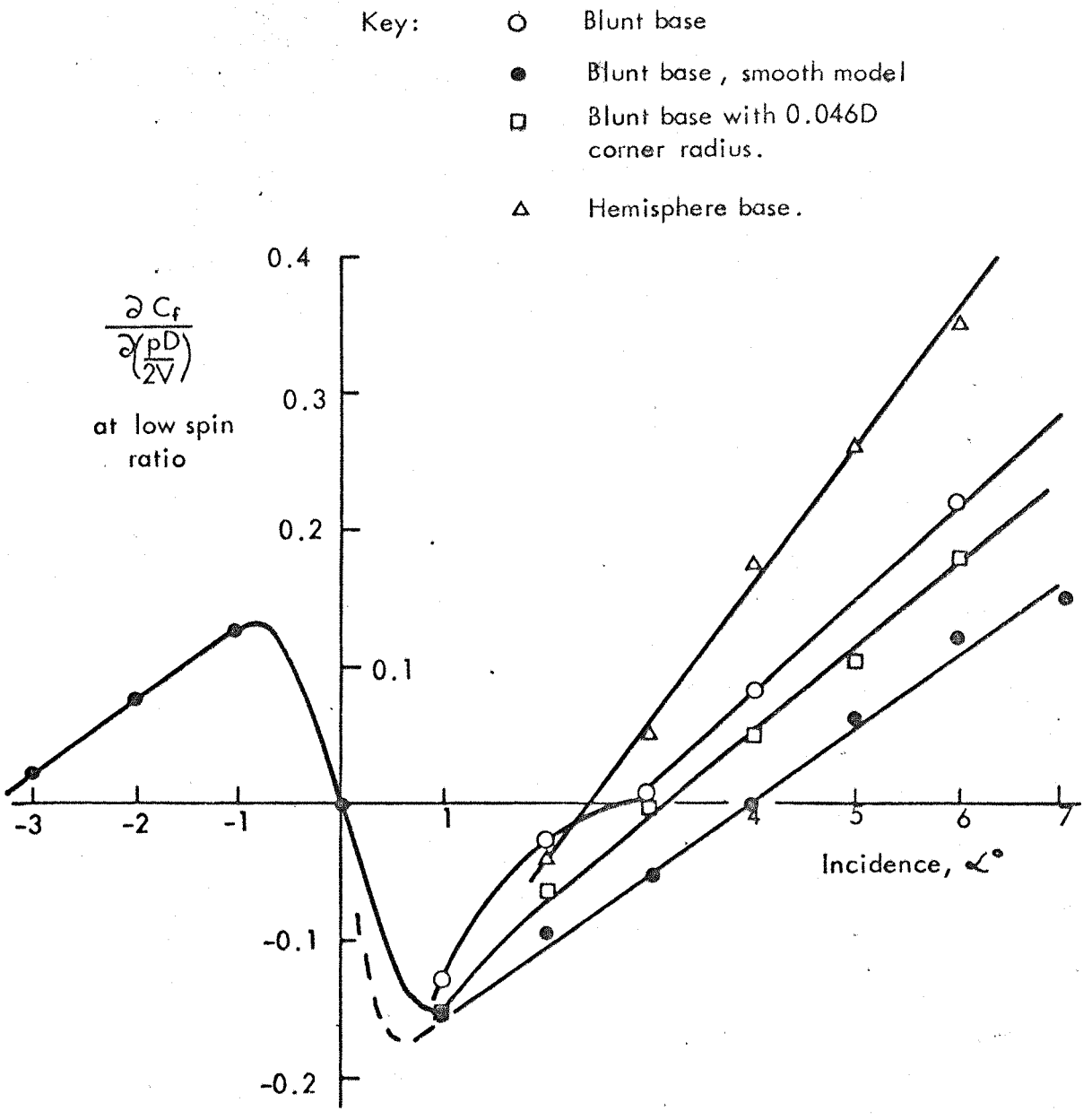

Roughness bands were applied except where stated.

FIG. 8-3(a). THE INFLUENCE OF BASE SHAPE AND INCIDENCE ON THE MAGNUS FORCE COEFFICIENT DERIVATIVE MEASURED AT LOW SPIN RATIO.

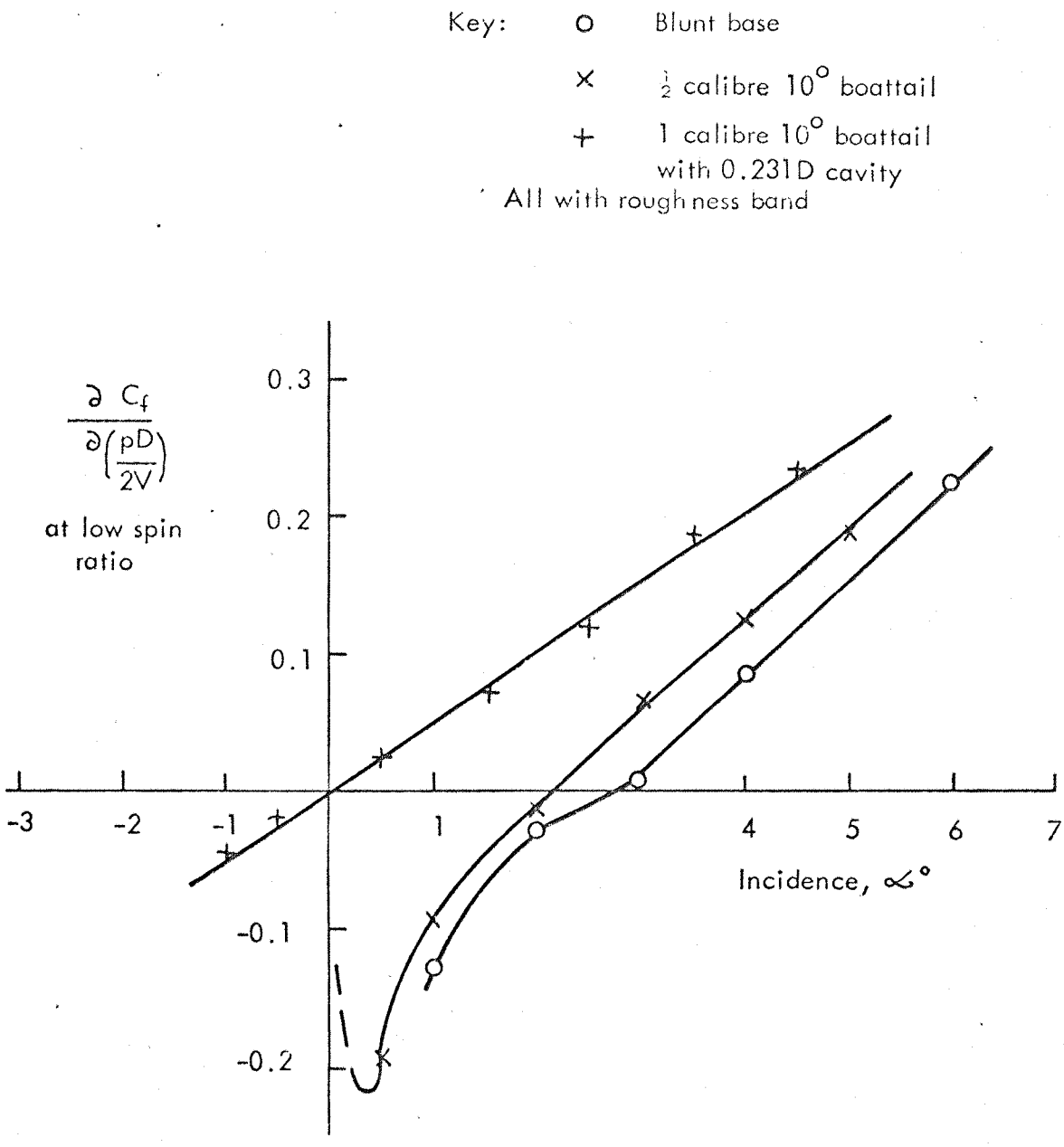

FIG. 8-3(b). THE INFLUENCE OF BASE SHAPE AND INCIDENCE ON THE MAGNU FORCE COEFFICIENT DERIVATIVE MEASURED AT LOW SPIN RATIO.

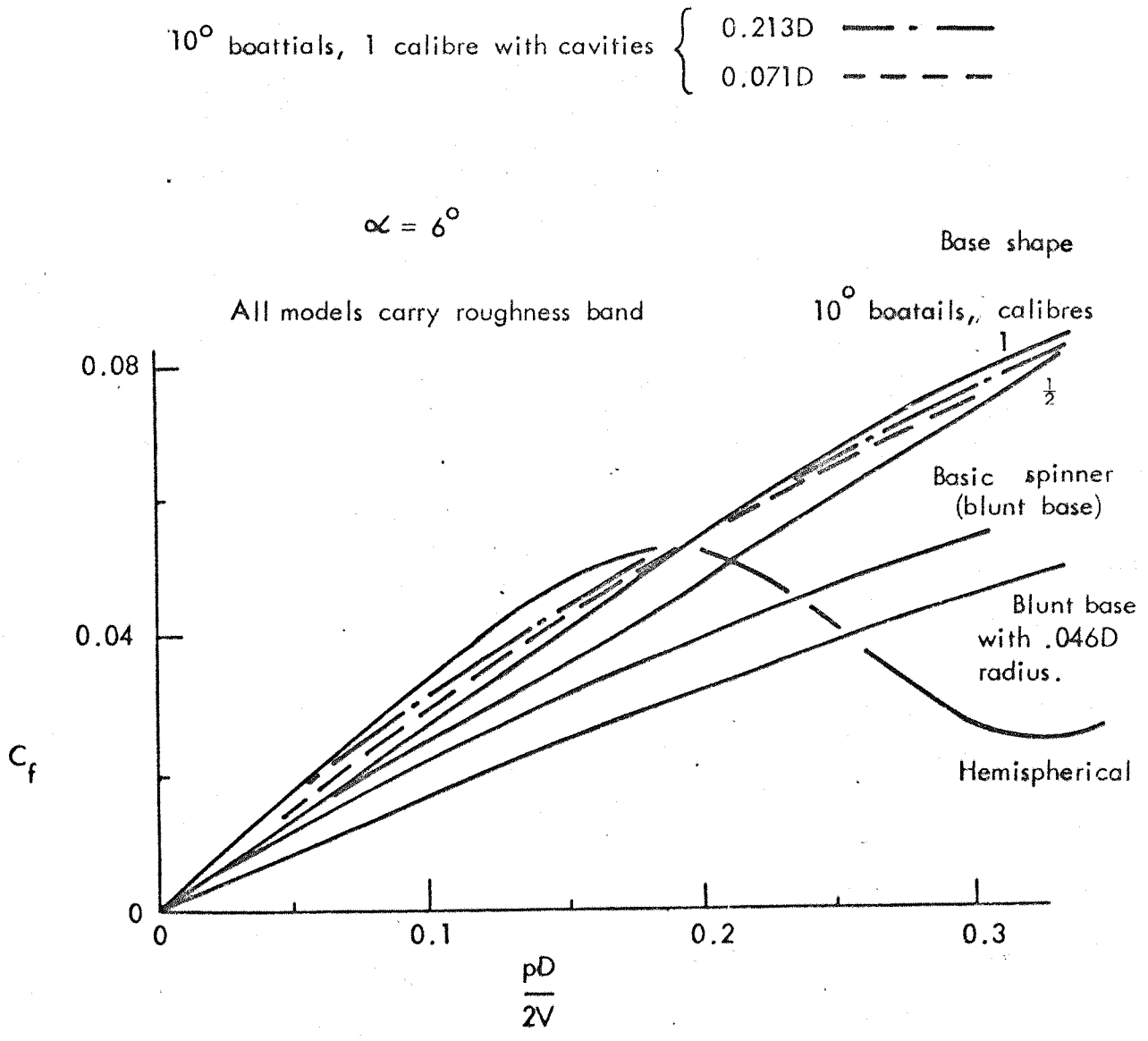

FIG. 8-4. THE INFLUENCE OF BASE GEOMETRY ON MAGNUS FORCE.

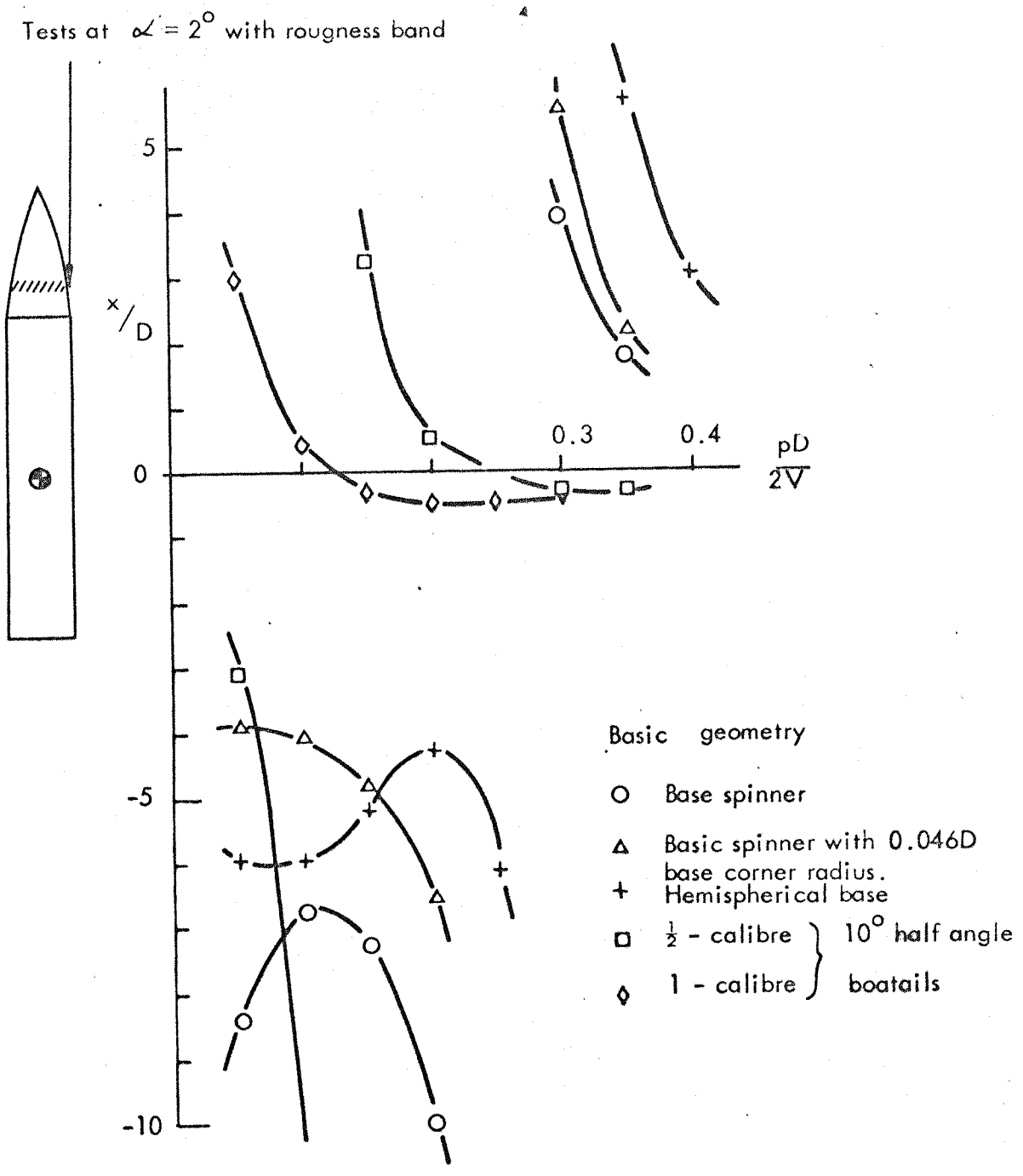

FIG. 8-5(a). EFFECT OF BASE GEOMETRY AND SPIN RATE ON THE EFFECTIVE POINT OF ACTION OF MAGNUS FORCE AT 2° ANGLE OF ATTACK.

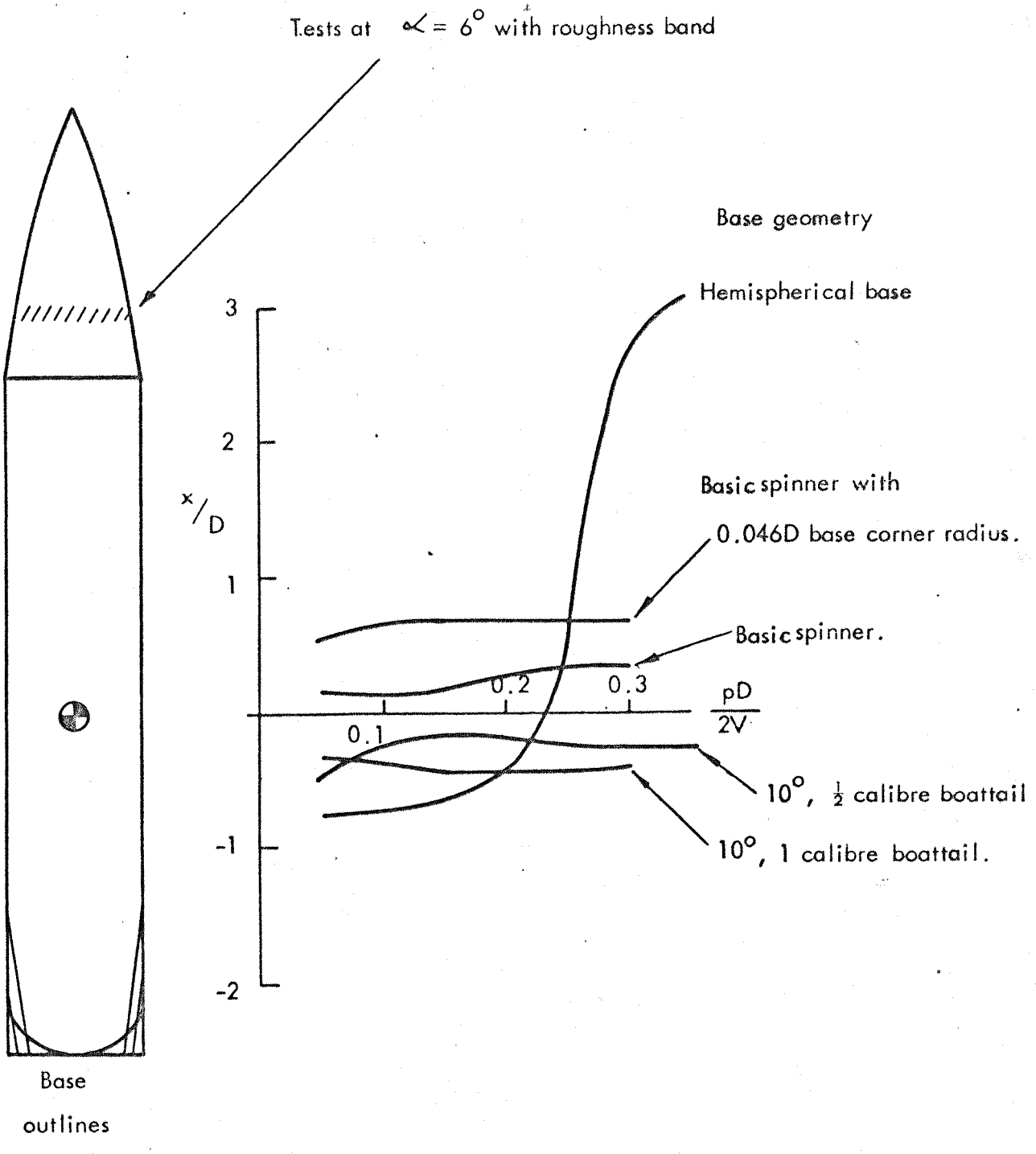

FIG. 8-5(b). EFFECT OF BASE GEOMETRY AND SPIN RATE ON THE EFFECTIVE POINT OF ACTION OF MAGNUS FORCE AT 6° ANGLE OF ATTACK.

Key:

— · — Theory of section 2.3 (ref.10)

□ WRE results, $\alpha = 10^\circ$ $R_{E_L} = 3.5 \times 10^5$ L/D = 7.07 (ref.20)

— — — MIT results, $\alpha = 9.5^\circ$ $R_{E_L} = 7.7 \times 10^5$ L/D = 5 (ref.16)

○ WRE results, $\alpha = 10^\circ$ $R_{E_L} = 14.1 \times 10^5$ L/D = 7.07 (ref.19)

——— Present work, $\alpha = 6^\circ$ $R_{E_L} = 7.6 \times 10^5$ L/D = 7 with added roughness.

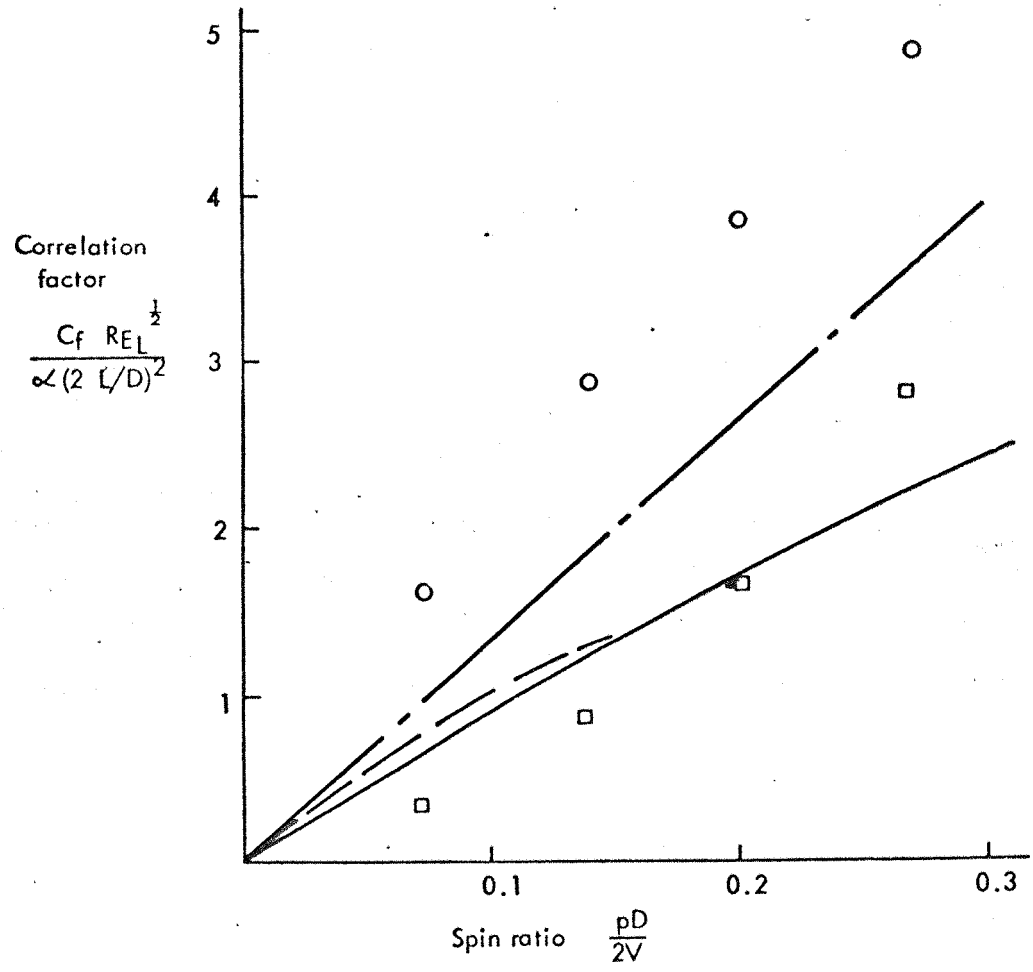

FIG. 8-6. CORRELATION OF EXPERIMENTAL AND THEORETICAL RESULTS FOR THE BLUNT BASE MODEL.

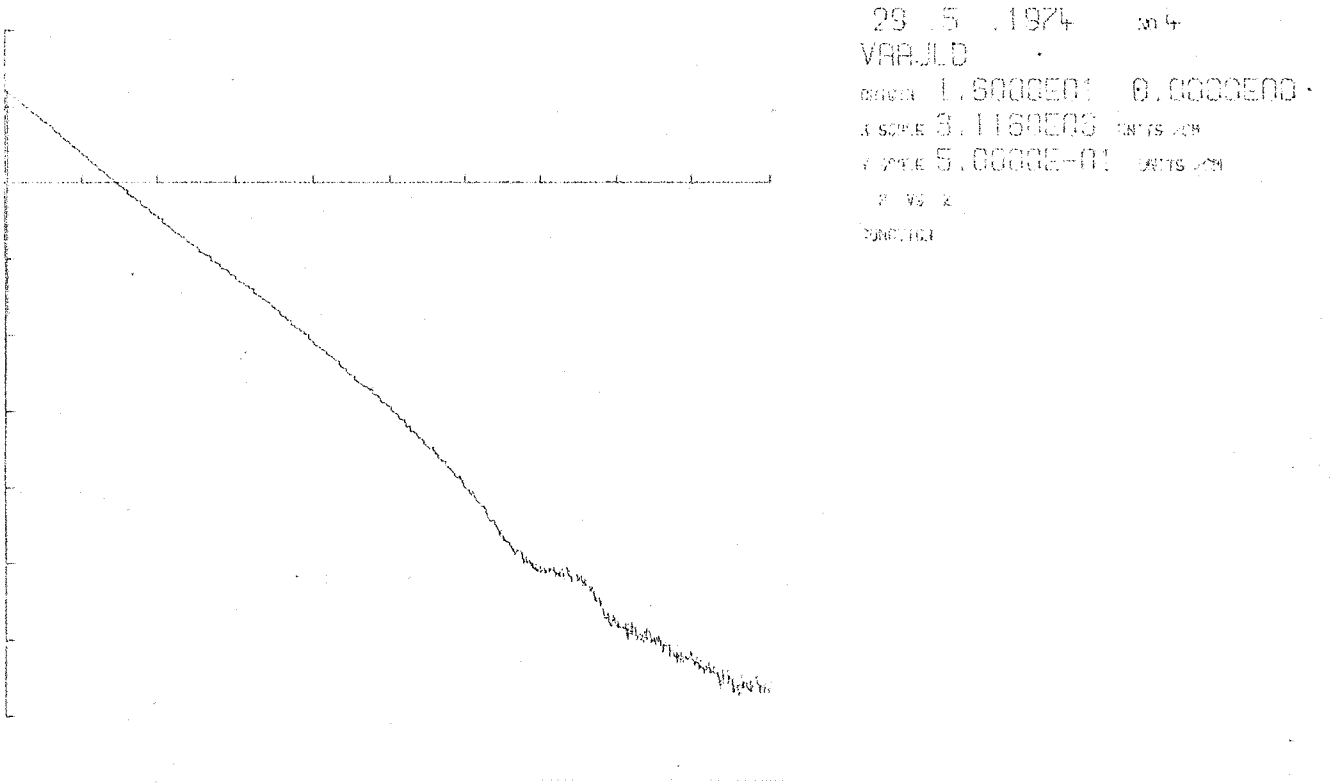

FIG 8.7 COMPUTER PLOT OF THE NATURAL LOGARITHM OF THE TACHOMETER OUTPUT VOLTAGE AGAINST TIME. THE SCALE OF THE TIME AXIS IS 3.116 SEC/CM.

APPENDIX A

MEASURED DATA

The raw data of Magnus force and moment coefficients as functions of spin ratio and incidence for all the shapes tested are recorded without further reduction in Figures A1 to A23. Some of the important features and trends of the data are described in this Appendix. Results are selected for presentation in Chapter 8 to highlight aerodynamic characteristics and systematic effects of such features as base geometry,

The base shapes tested are summarised in Table A-1, which is reproduced in part from Table 8.1 in Chapter 8.

TABLE A-1

Base Shapes and Case Numbers

Case No.	Base Geometry
1(a),(b)	Basic model, blunt base
2	Blunt base with 0.046D radius corner
3(a),(b)	Hemisphere
4	5^{o} boattail, $\frac{1}{2}$ calibre long
5	10^{o}, $\frac{1}{2}$ calibre
6	5^{o}, 1 calibre
7	10^{o}, 1 calibre
8	10^{o}, 1 calibre with 0.071D base cavity
9	10^{o}, 1 calibre with 0.213D cavity.

Cases 1(b) and 3(b) refer to the clean or smooth model. In all other cases a roughness band was applied to the nose.

Case 1. Basic spinner

1(a) With roughness (Figures A1 and A2)

The shape exhibits a substantial negative Magnus force near the base at low incidences (0^{o} - 3^{o}). The greatest effect is at very low incidences ($\sim 1^{o}$) and low pD/2V. At the higher spin ratios, the curves appear to be tending to the theoretically predicted linear functions.

Noteworthy is the change in trend of the curves in the 0.1 - 0.2 spin parameter regime. At higher spin ratios the coefficient tends towards the positive direction, and the centre of pressure moves nearer to the reference centre.

The higher incidences seem well-behaved. At 6^{o} there is an almost linear dependence of C_f on spin ratio.

1(b) 'Clean' model (Figures A3 to A6)

Qualitatively, the results are similar to those from the roughened model at low pD/2V. In the pitch interval 0^{o} - 3^{o}, the Magnus force coefficient derivative $dC_f/d(pD/2V)$ is greater than for the above case at low spin rates, and the cross-over point, where $dC_f/d(pD/2V) = 0$, lies at 4^{o}, as against 3^{o}. Plots of this derivative as a function of incidence for these and other models are shown in Figures 8.2(a) and (b). The derivative is estimated at $p = 0$.

The tendency of the C_f-spin ratio curves towards linearity observed with the roughened model above 3^{o} is not present in the 'clean' case. The trends for this smooth-model case are more complex, but show consistent variations with changes of incidence and spin rate, implying a more complicated fluid mechanic process. Since the main interest lay in simulating high Reynolds number behaviour, the pronounced differences in Magnus force between rough and smooth models provide a justification for concentrating most of the work on roughened models.

Case 2. Blunt Base, with 0.046 calibre radiused corner (Figures A7 and A8)

The roughness band was applied for these measurements. This base shows small differences in the force and moment characteristics from those of the blunt base, case 1(a). The cross-over point of the low spin force derivative is shifted to about $\alpha = 3^{o}$, and there are minor differences in the form of the C_f curve at $\alpha = 1^{o}$. The centre of pressure at 4^{o} incidence and above is a small distance further upstream.

Case 3. Hemisphere base

3(a) Roughness band applied (Figures A9 and A10)

For the limiting case of small pD/2V, the force coefficient derivative increases more rapidly with angle of incidence than with the previously discussed bases, see Figure 8.2(a). The zero cross-over

point is in the region 2 to $2\frac{1}{2}^{o}$. However, the most outstanding feature of the results is the stronger contribution of the base to the Magnus characteristics. Not only is there a large dip in the Magnus force over a range of spin ratios, the exact range depending on the pitch, but the Magnus force at the base is approximately doubled in magnitude. The conditions near the nose of the model are well-behaved and closely resemble those of the basic shape.

3(b) 'Clean' model (Figures all to A15)

Without the roughness band, the Magnus force on the hemisphere-based model undergoes extraordinary excursions into the negative, the region around the base being entirely responsible. The Magnus force coefficient reaches a value of -0.12 at 5^{o} incidence and a spin ratio of 0.15. For values of α and pD/2V on either side of this C_f decreases. At an incidence of 3^{o} two distinct negative 'humps' are evident. The general form is extremely complex, and the process of boundary layer transition and its effect on separation at the base probably plays a large part, so that the observed side forces are not true Magnus forces in the accepted sense. The results do show, however, that control of separation at the base is essential for well-behaved Magnus characteristics.

Case 4. 5^{o} Half-angle, $\frac{1}{2}$ calibre boattail. Roughness band applied. Figures A16 and A17

The major difference between this boattailed base and the blunt base is that the Magnus force coefficient at 4^{o} incidence is considerably larger than that of the basic shape (0.040 as compared with 0.025 at a spin ratio of 0.30). This appears to be a result at low angles of attack of a reduction in negative component of Magnus force at the base, and a corresponding increasing in positive Magnus force at the base at higher angles of attack. This is confirmed by the reduced angle of cross-over (i.e. the incidence at which $dC_f/d(pD/2V) = 0$) and the smaller peak value of negative C_f at $\alpha = 1^{o}$.

Case 5. 10° Half-angle, $\frac{1}{2}$ calibre boattail. Roughness band applied. (Figures A18 and A19)

Here, there is some modification of the C_f and C_T curves at the lower incidences, as compared with the $5^{\circ}/\frac{1}{2}$-calibre results. The negative base effect does not extend so far up the spin ratio range, or the incidence range, as can be seen from a comparison of the two sets of results at 1° and 2°. At the highest pitch angle tested with the $5^{\circ}/\frac{1}{2}$-calibre base (4°), comparison shows the $10^{\circ}/\frac{1}{2}$-calibre base to have the higher Magnus force coefficient, probably owing to the reduction in the base effect.

Case 6. 5° Half-angle boattail, length - 1 calibre (Tripping band applied)

Results showed a similarity with the $10^{\circ}/\frac{1}{2}$-calibre base at low angles of incidence.

Case 7. 10° Half-angle, 1-calibre boattail. Roughness band applied (Figures A20 and A21)

The base effect at the low incidences has almost disappeared with this base shape. Some obvious non-linearity can be seen at spin ratios below 0.1 in the $0 - 2.5^{\circ}$ range of pitch.

Note that the C_f scales used for $\alpha = 0$ to $2\frac{1}{2}^{\circ}$ are different from that used for 6° incidence. Also note that a small misalignment in pitch seems to have occurred.

At 6° incidence, the centre of Magnus pressure is behind the moment reference point.

Case 8. Boattail base with cavity of depth 0.071 calibres (Figure A22)

Data was obtained as just one angle of attack, 6°. This result may be compared with other force data for similar geometries in Figure 8.4. At this angle of attack the magnitude of Magnus force is very similar for all boattail bases for which data is available.

Case 9. Boattail base with cavity of depth 0.213 calibres (Figures A22 and A23)

This configuration shows a complete absence of negative Magnus forces at the base and was the only configuration tested which provided an almost linear variation of Magnus force coefficient with spin ratio over the range of incidences investigated. Compared with base no. 8 at an

incidence of 6°, no significant difference in Magnus force is evident, see Figure 8.4. At a spin ratio of 0.40, $C_T = 0.05$, $C_f = 0.094$, giving a centre of pressure 0.55 calibres upstream of the reference centre, i.e. 3.05 calibres from the base.

The linearity of the C_f and C_T curves is preserved throughout the small incidence range. The C_f curves appear to approximate to parabolas, with slopes diminishing with increasing spin ratio. The force coefficient at any one value of spin ratio is close to a linear function of angle of attack.

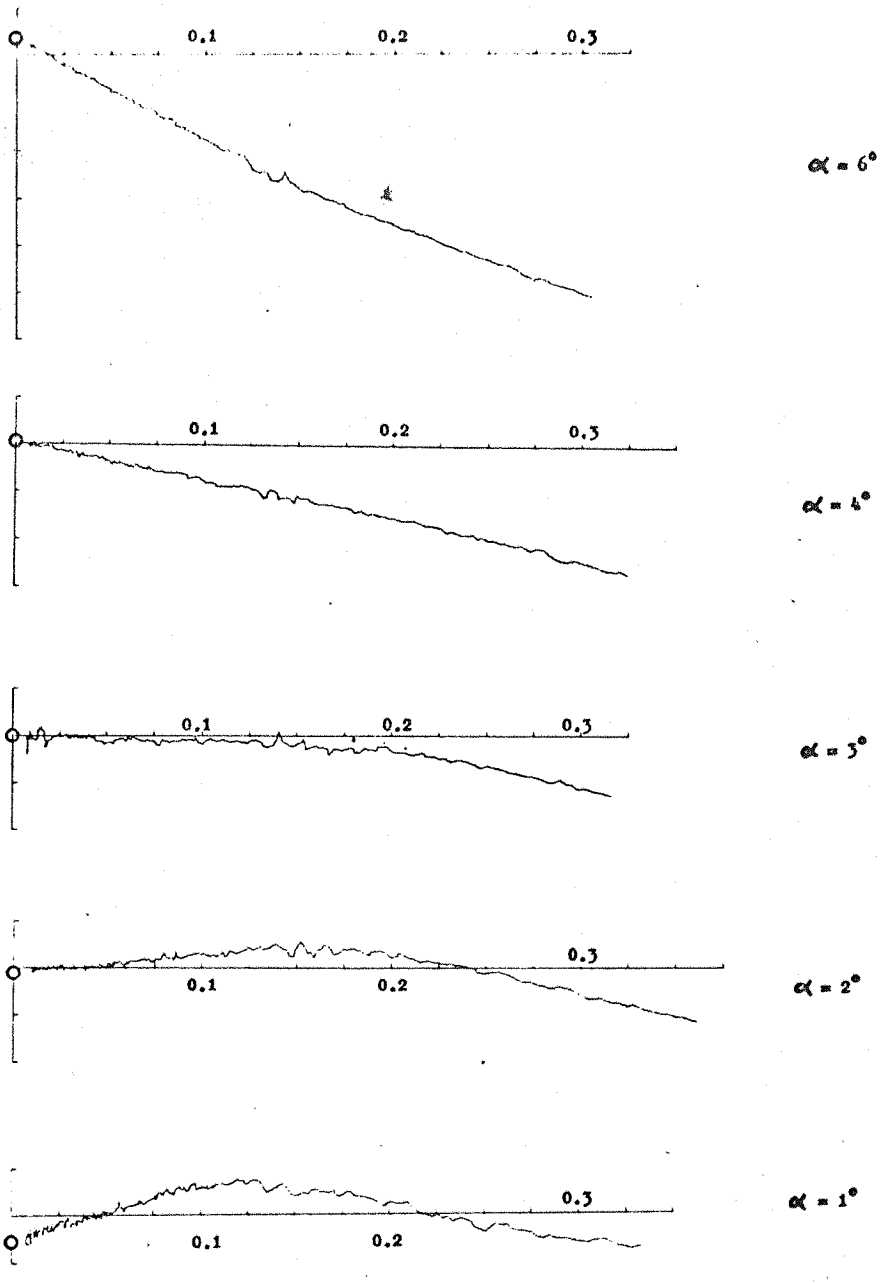

SIDE FORCE COEFFICIENT VERSUS pD/2V C_f 0.01 UNITS/DIV

7-CALIBRE OGIVE CYLINDER WITH BLUNT BASE pD/2V 0.025 UNITS/DIV

ROUGHNESS BAND APPLIED

FIGURE A1. CASE 1(a)

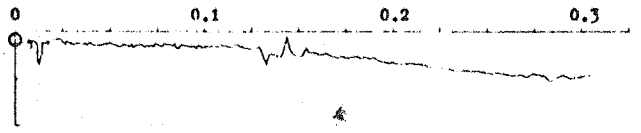

$\alpha = 6^\circ$

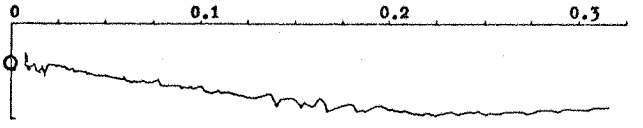

$\alpha = 3^\circ$

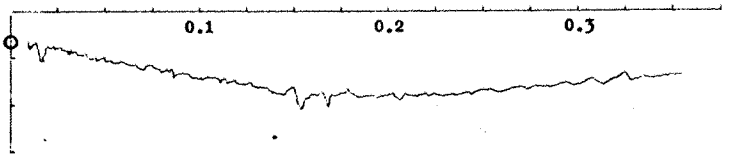

$\alpha = 2^\circ$

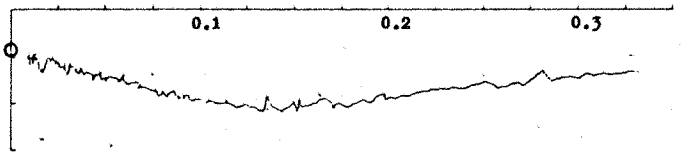

$\alpha = 1^\circ$

YAWING MOMENT COEFFICIENT VERSUS pD/2V C_T 0.025 UNITS/DIV

7-CALIBRE OGIVE CYLINDER WITH BLUNT BASE pD/2V 0.025 UNITS/DIV

ROUGHNESS BAND APPLIED

FIGURE A2. CASE 1(a)

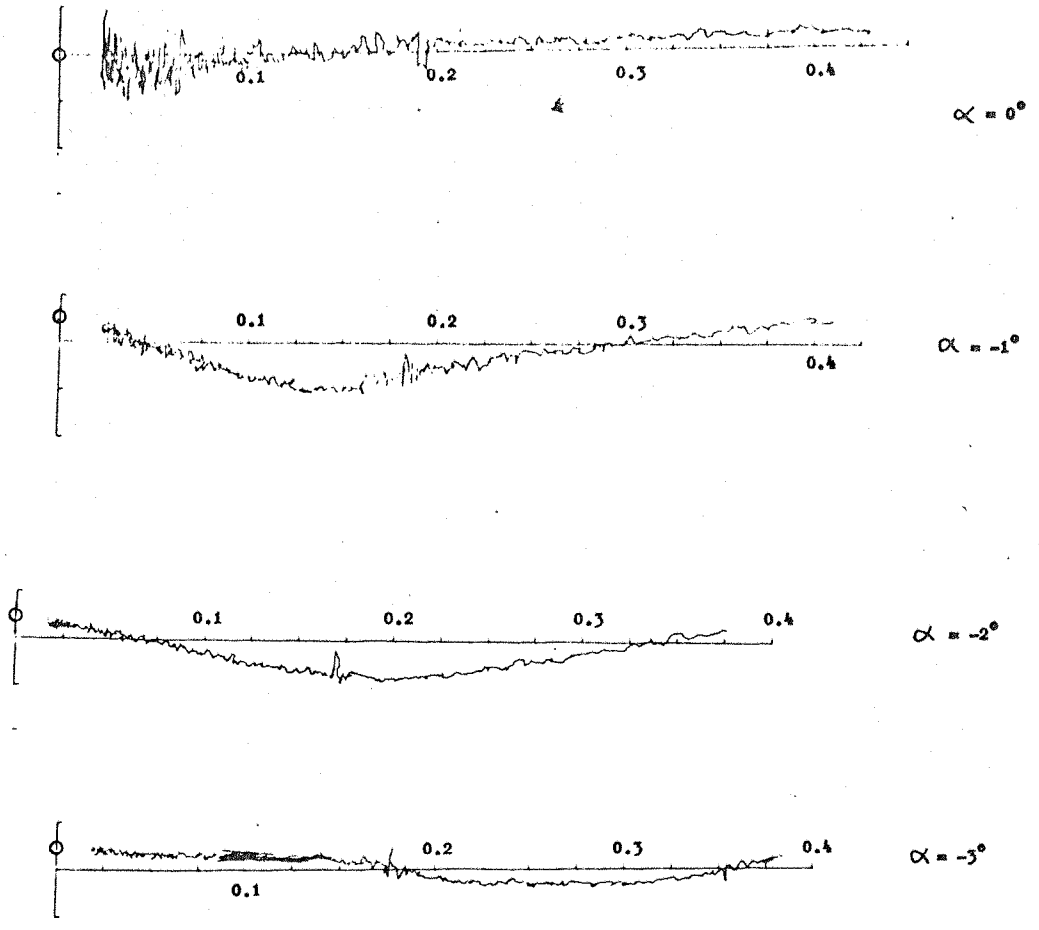

SIDE FORCE COEFFICIENT VERSUS pD/2V

7-CAL OGIVE

BLUNT BASE, CLEAN MODEL.

C_f: 0.01 UNITS/DIV

pD/2V: 0.025 UNITS/DIV

FIGURE A3. CASE 1(b)

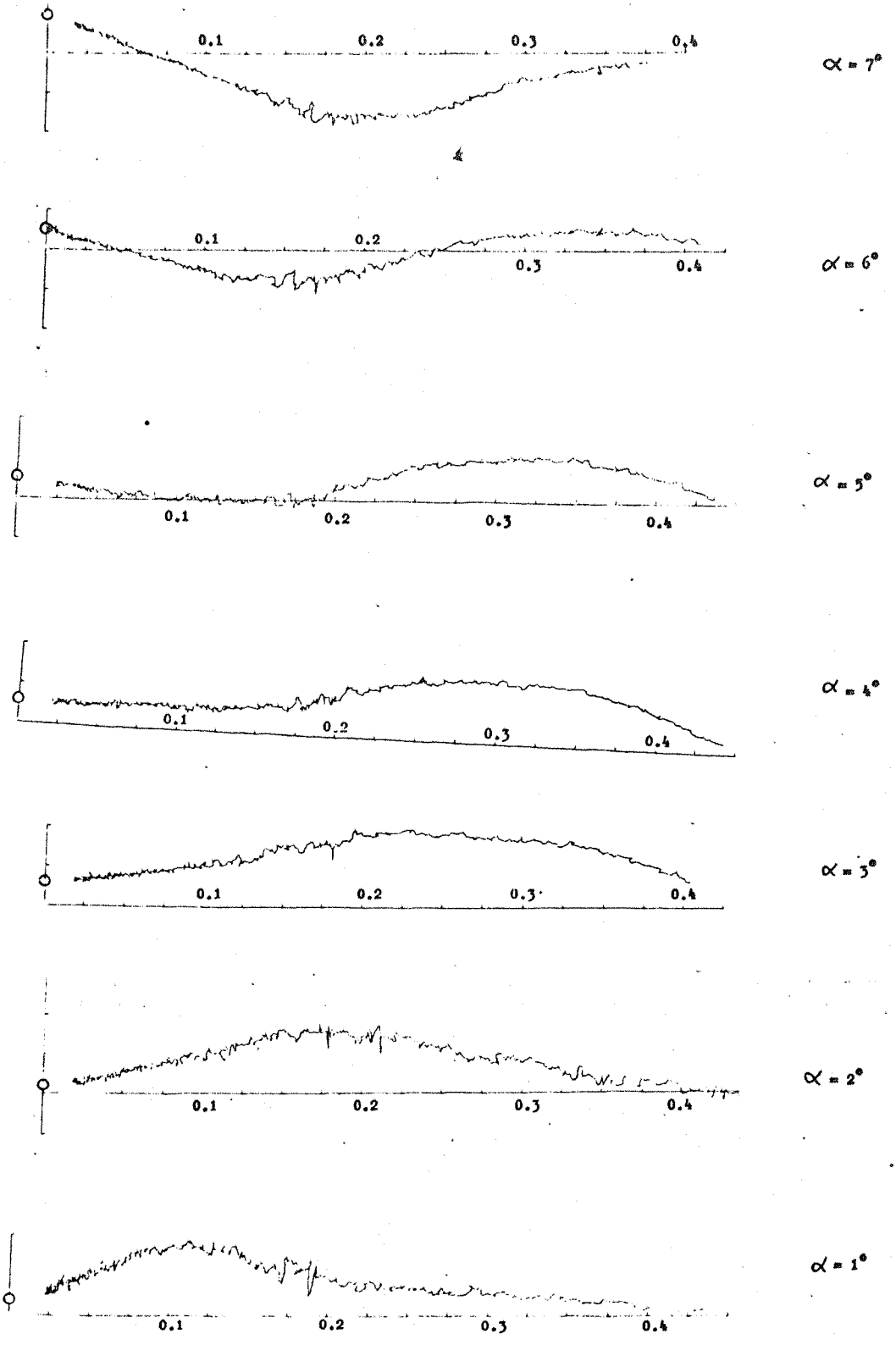

SIDE FORCE COEFFICIENT VERSUS pD/2V

7-CAL OGIVE WITH BLUNT BASE, CLEAN MODEL

Y SCALE: C_f 0.01 UNITS/DIV

X SCALE: pD/2V 0.025 UNITS/DIV

FIGURE A4. CASE 1(b)

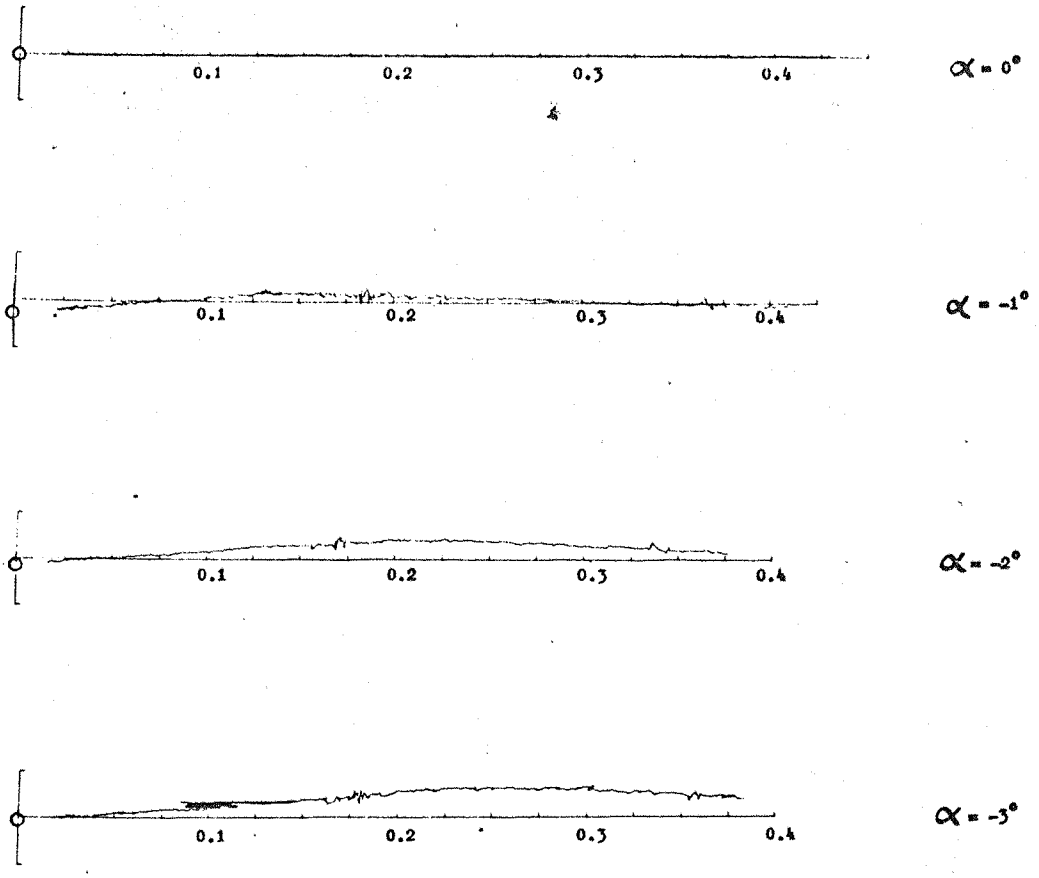

YAWING MOMENT COEFFICIENT VERSUS pD/2V

7-CAL OGIVE

BLUNT BASE, CLEAN MODEL

C_T: 0.1 UNITS/DIV

pD/2V: 0.025 UNITS/DIV

FIGURE A5. CASE 1(b)

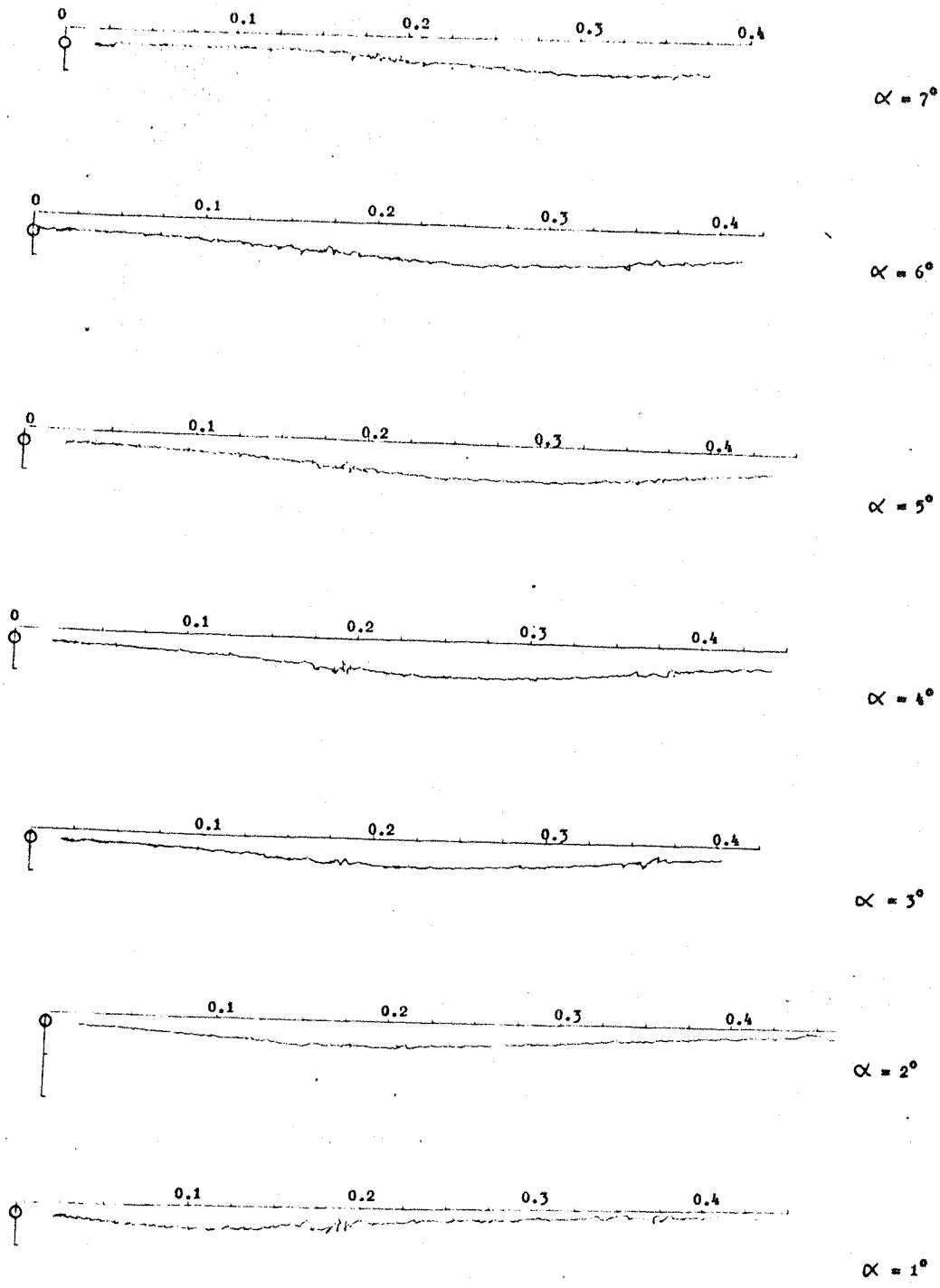

YAWING MOMENT COEFFICIENT VERSUS pD/2V

7-CAL OGIVE WITH BLUNT BASE, CLEAN MODEL

C_T: 0.1 UNITS/DIV

pD/2V: 0.025 UNITS/DIV

FIGURE A6. CASE 1(b)

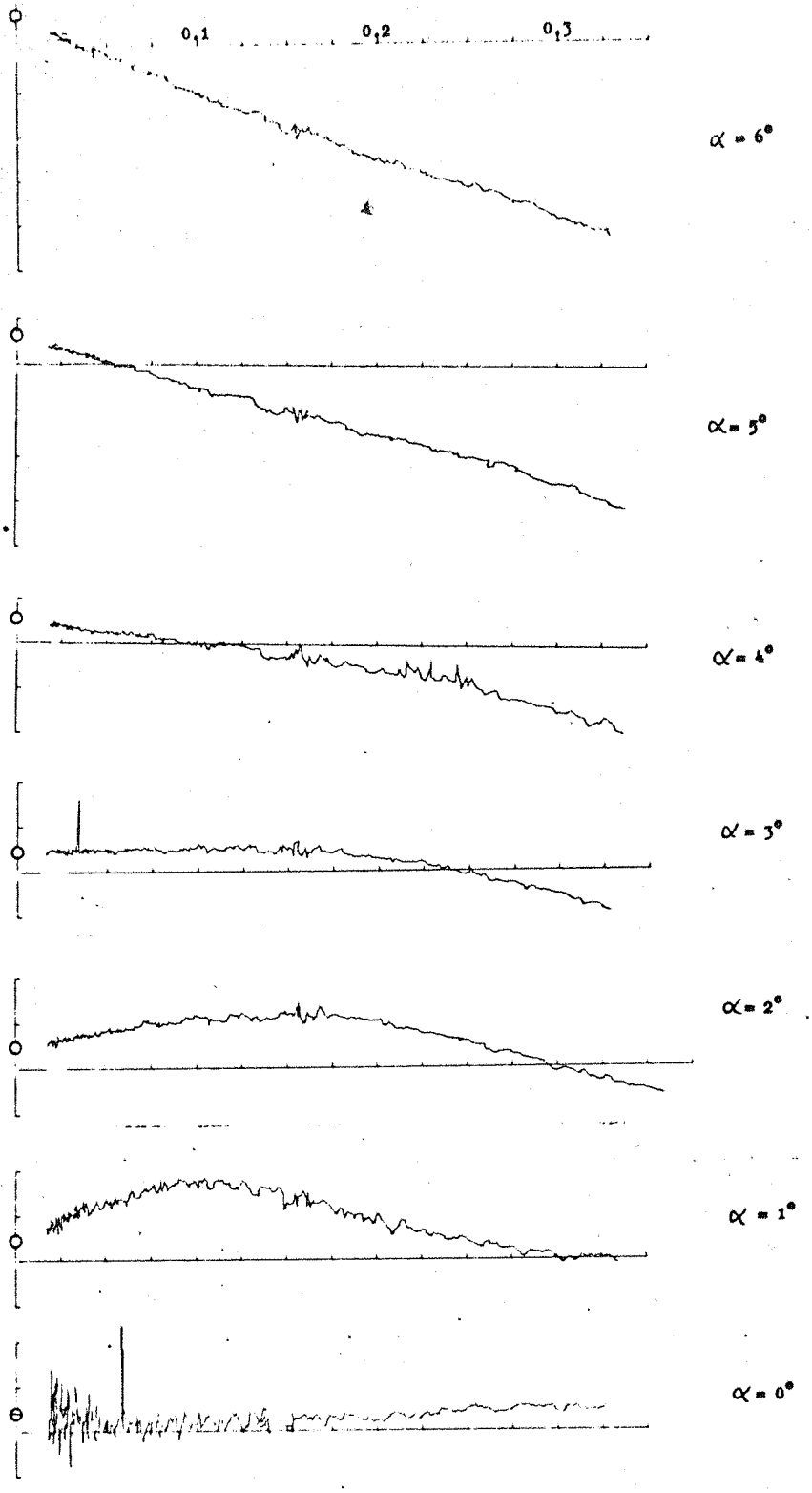

SIDE FORCE COEFFICIENT VERSUS pD/2V

BLUNT BASE WITH 0.046D CORNER RADIUS

ROUGHNESS BAND APPLIED

C_f: 0.01 UNITS/DIV

pD/2V: 0.025 UNITS/DIV

FIGURE A7. CASE 2

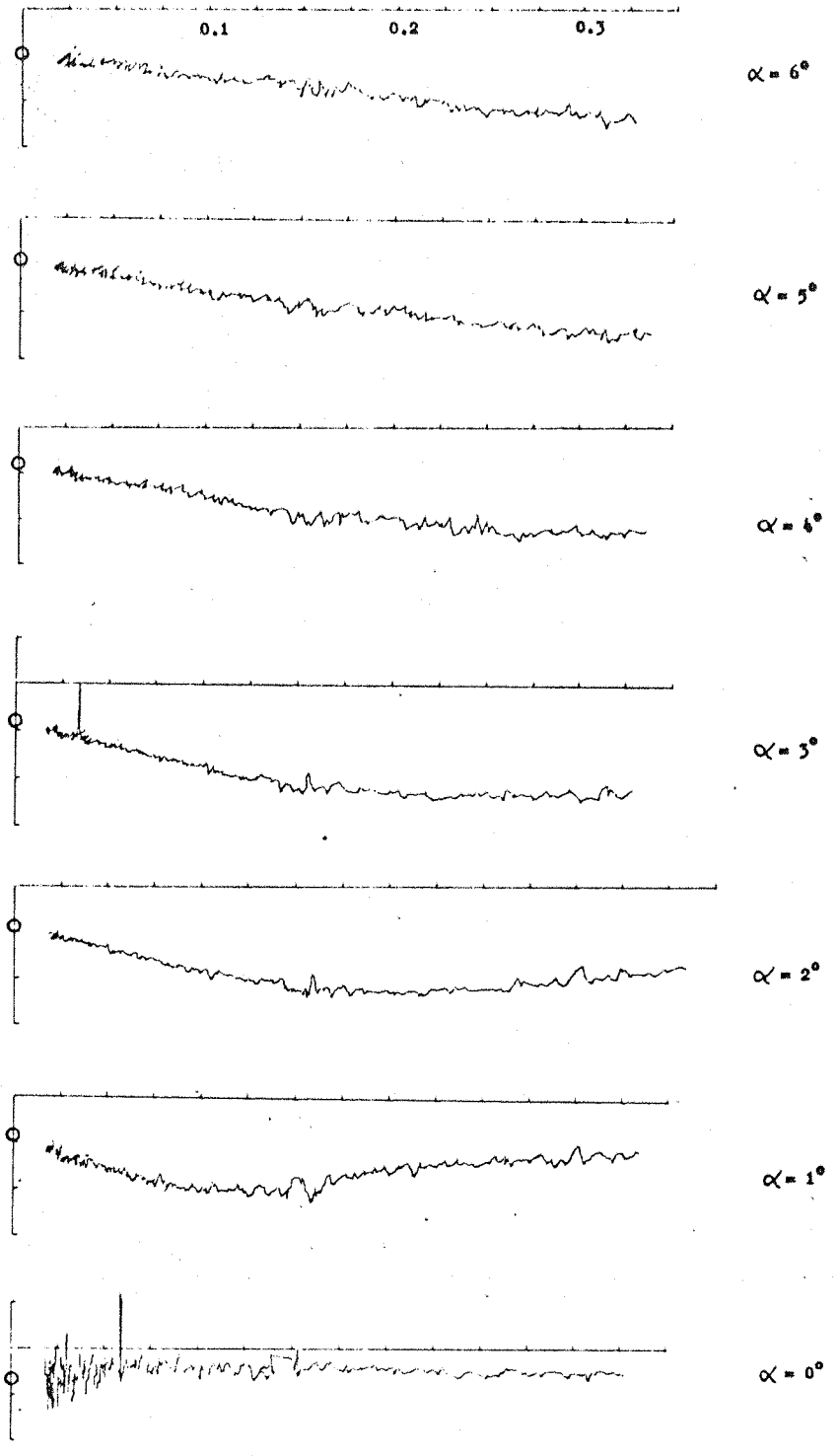

YAWING MOMENT COEFFICIENT VERSUS pD/2V — C_T 0.025 UNITS/DIV

BLUNT BASE WITH 0.046D CORNER RADIUS — pD/2V 0.025 UNITS/DIV

ROUGHNESS BAND APPLIED

FIGURE A8. CASE 2

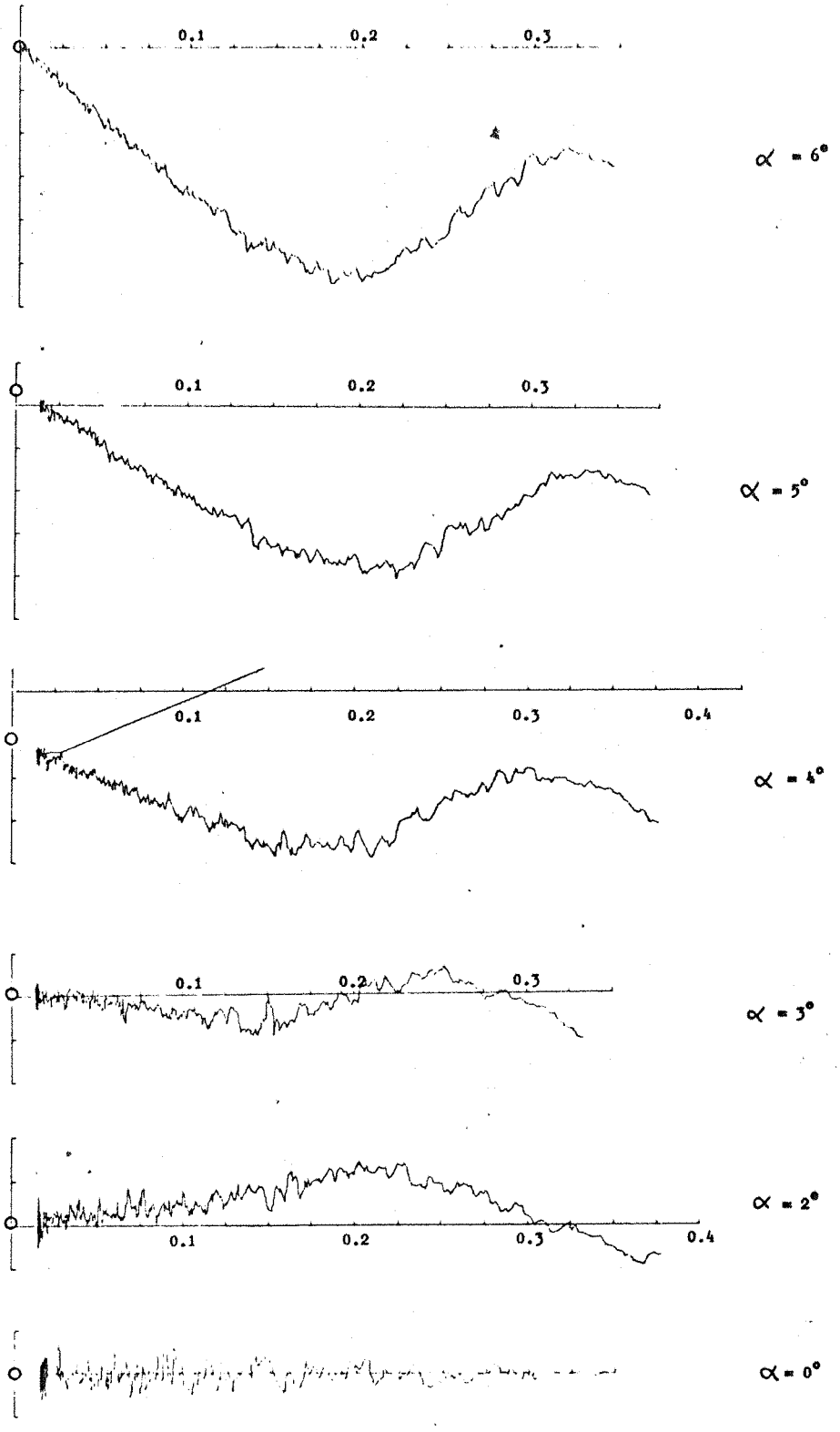

SIDE FORCE COEFFICIENTS VERSUS pD/2V

7-CAL OGIVE WITH HEMISPHERE BASE,

WITH ROUGHNESS BAND

C_f 0.01 UNITS/DIV

pD/2V 0.025 UNITS/DIV

FIGURE A9. CASE 3(a)

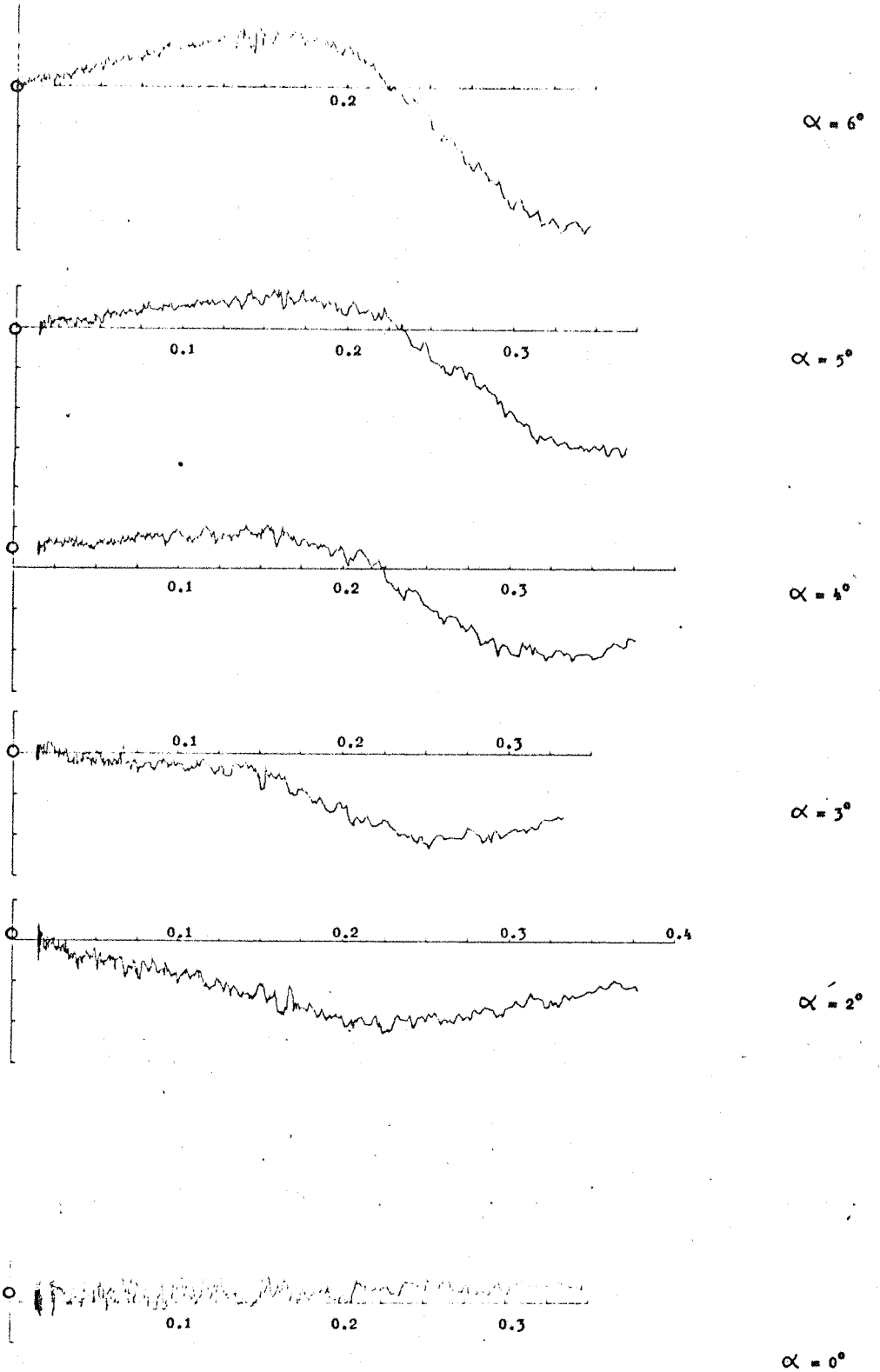

YAWING MOMENT COEFFICIENT VERSUS pD/2V

7-CAL OGIVE WITH HEMISPHERE BASE,

WITH ROUGHNESS BAND

C_T 0.025 UNITS/DIV

pD/2V 0.025 UNITS/DIV

FIGURE A10. CASE 3(a)

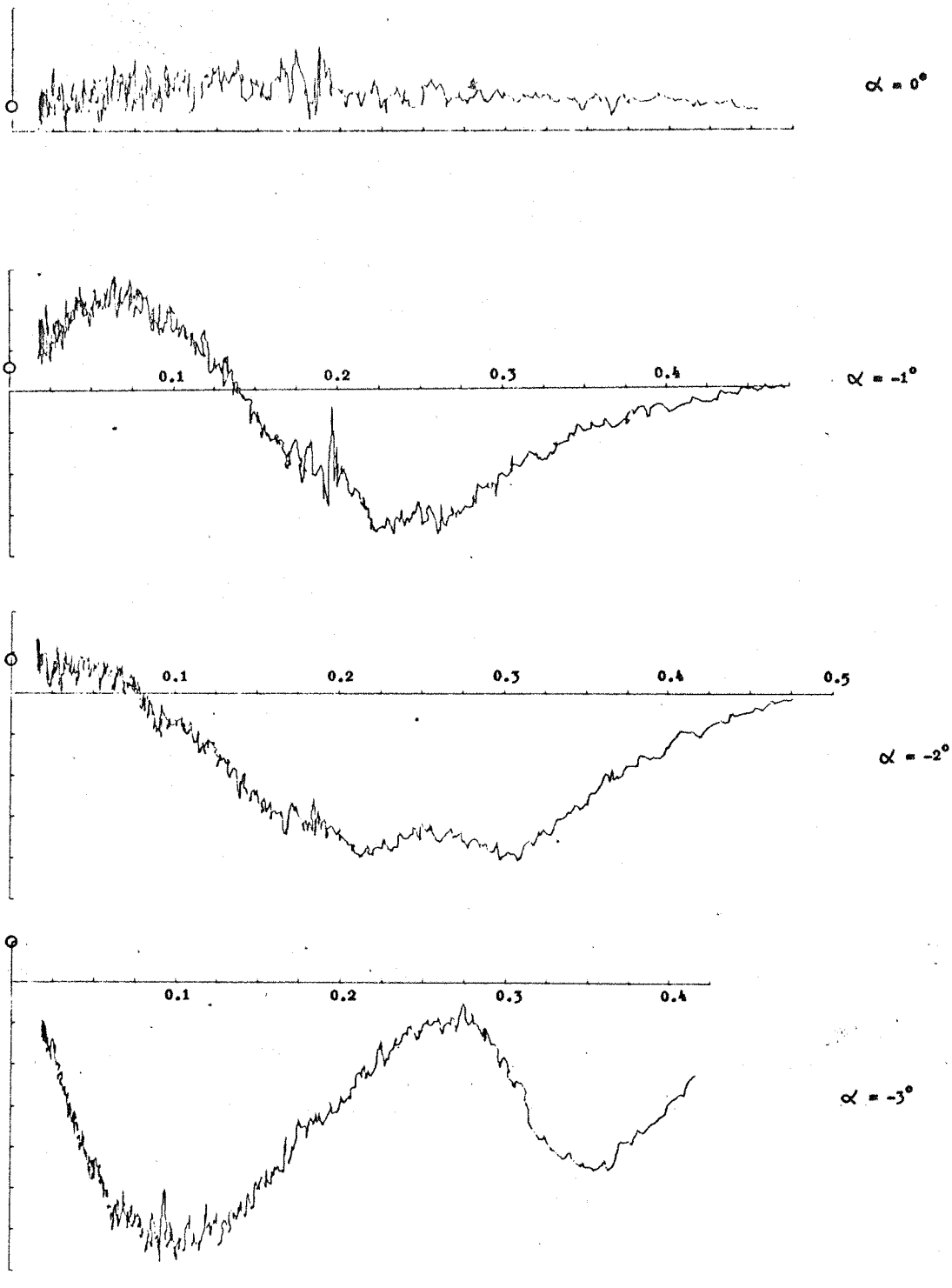

SIDE FORCE COEFFICIENT VERSUS pD/2V — C_f 0.01 UNITS/DIV

7-CAL OGIVE WITH HEMISPHERE BASE, CLEAN MODEL — pD/2V 0.025 UNITS/DIV

FIGURE A11. CASE 3(b)

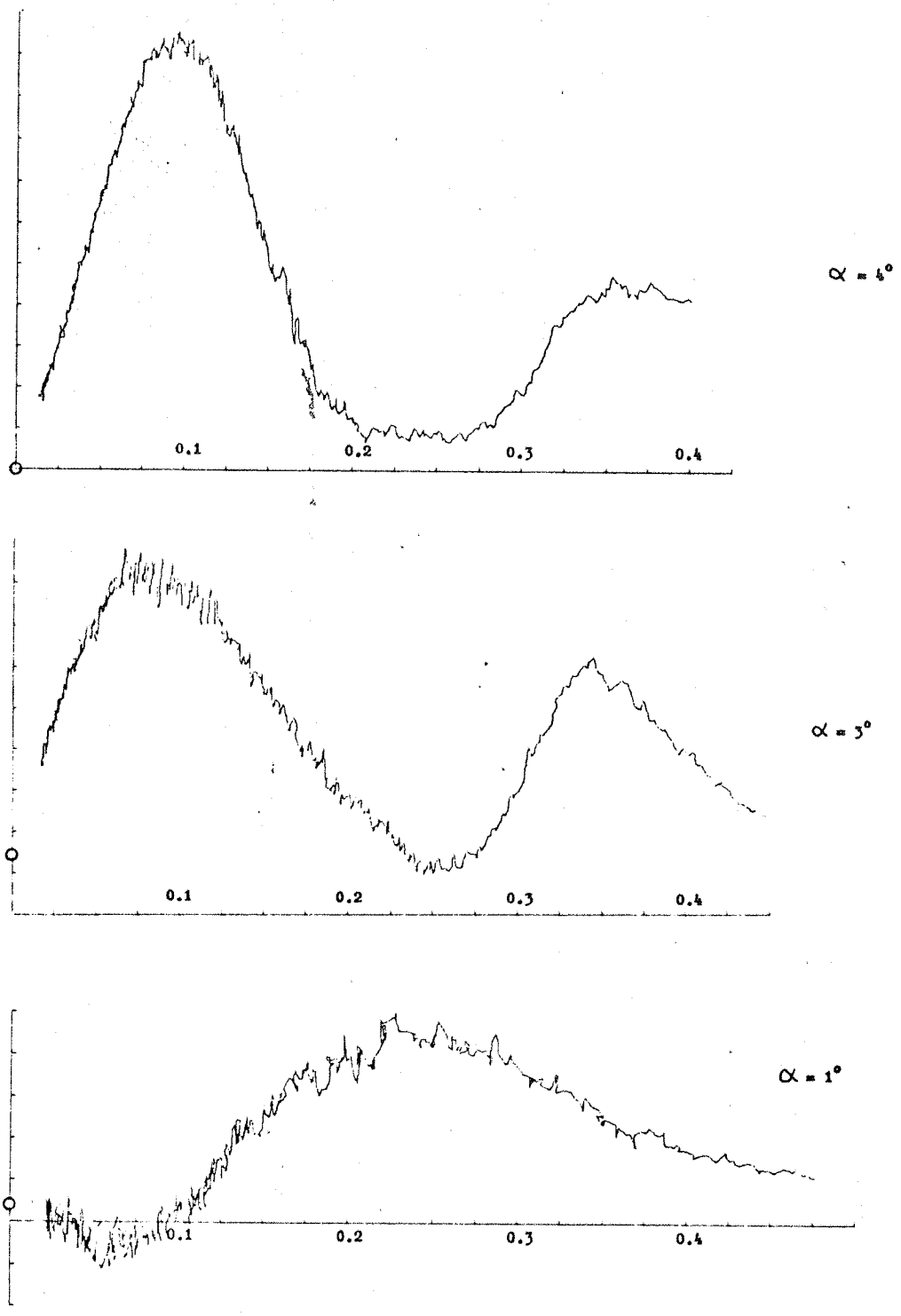

SIDE FORCE COEFFICIENT VERSUS pD/2V

7-CAL OGIVE WITH HEMISPHERE BASE, CLEAN MODEL

C_f 0.01 UNITS/DIV

pD/2V 0.025 UNITS/DIV

FIGURE A12. CASE 3(b)

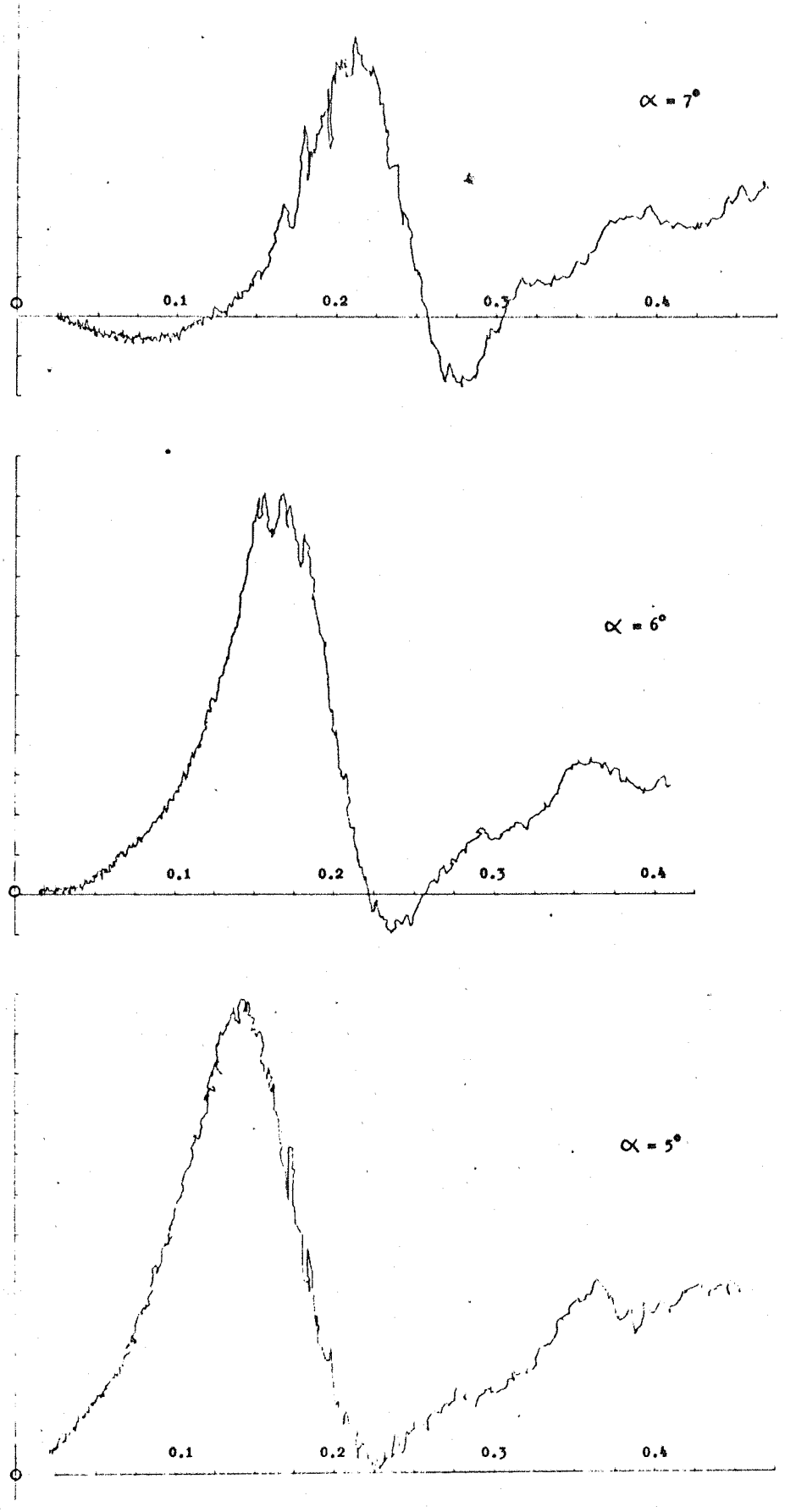

SIDE FORCE COEFFICIENT VERSUS pD/2V

7-CAL OGIVE WITH HEMISPHERE BASE, CLEAN MODEL

C_f 0.01 UNITS/DIV

pD/2V 0.025 UNITS/DIV

FIGURE A13. CASE 3(b)

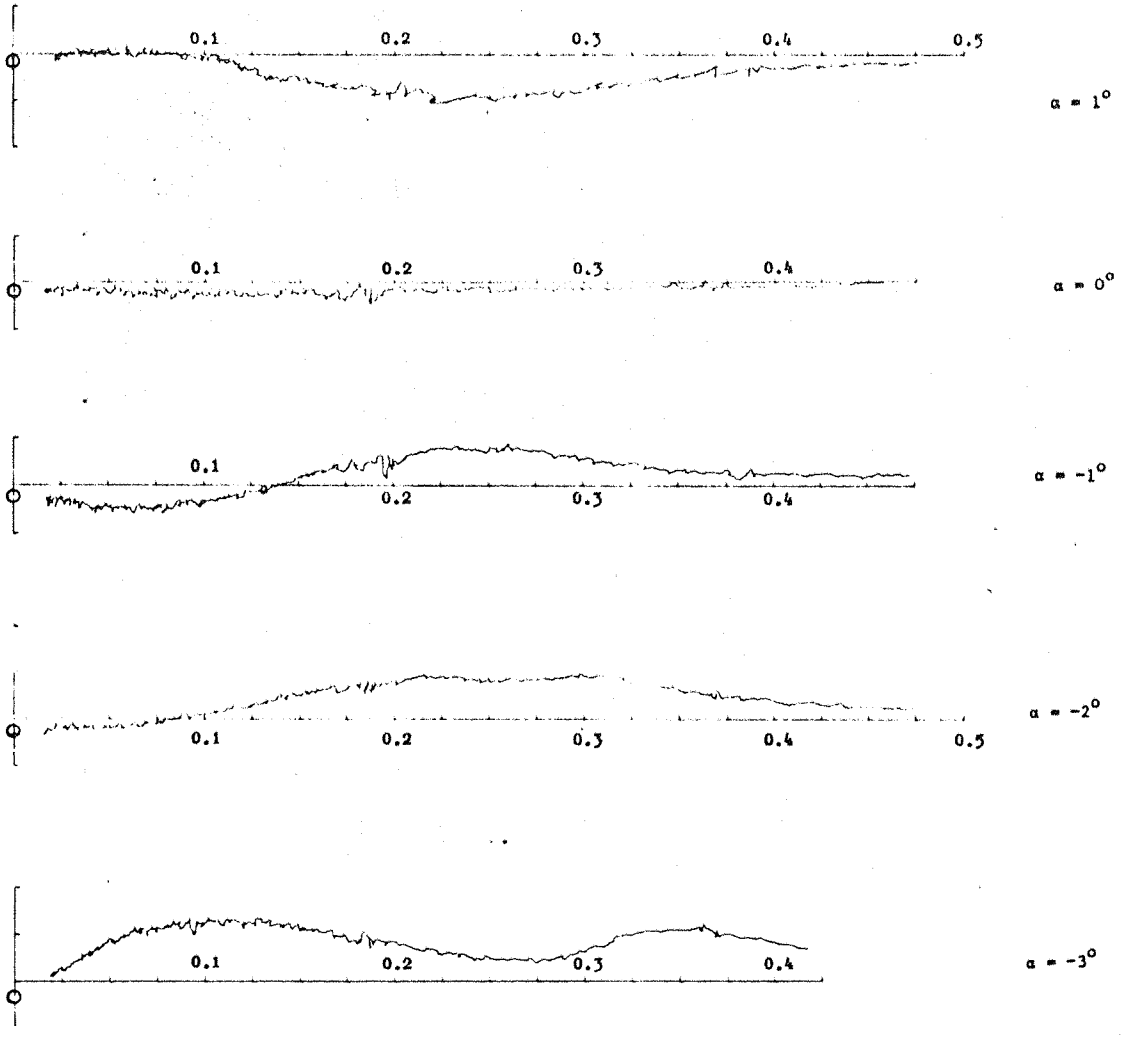

YAWING MOMENT COEFFICIENT VERSUS pD/2V

7-CAL OGIVE WITH HEMISPHERE BASE, CLEAN MODEL

C_T 0.1 UNITS/DIV

pD/2V 0.025 UNITS/DIV

FIGURE A14. CASE 3(b)

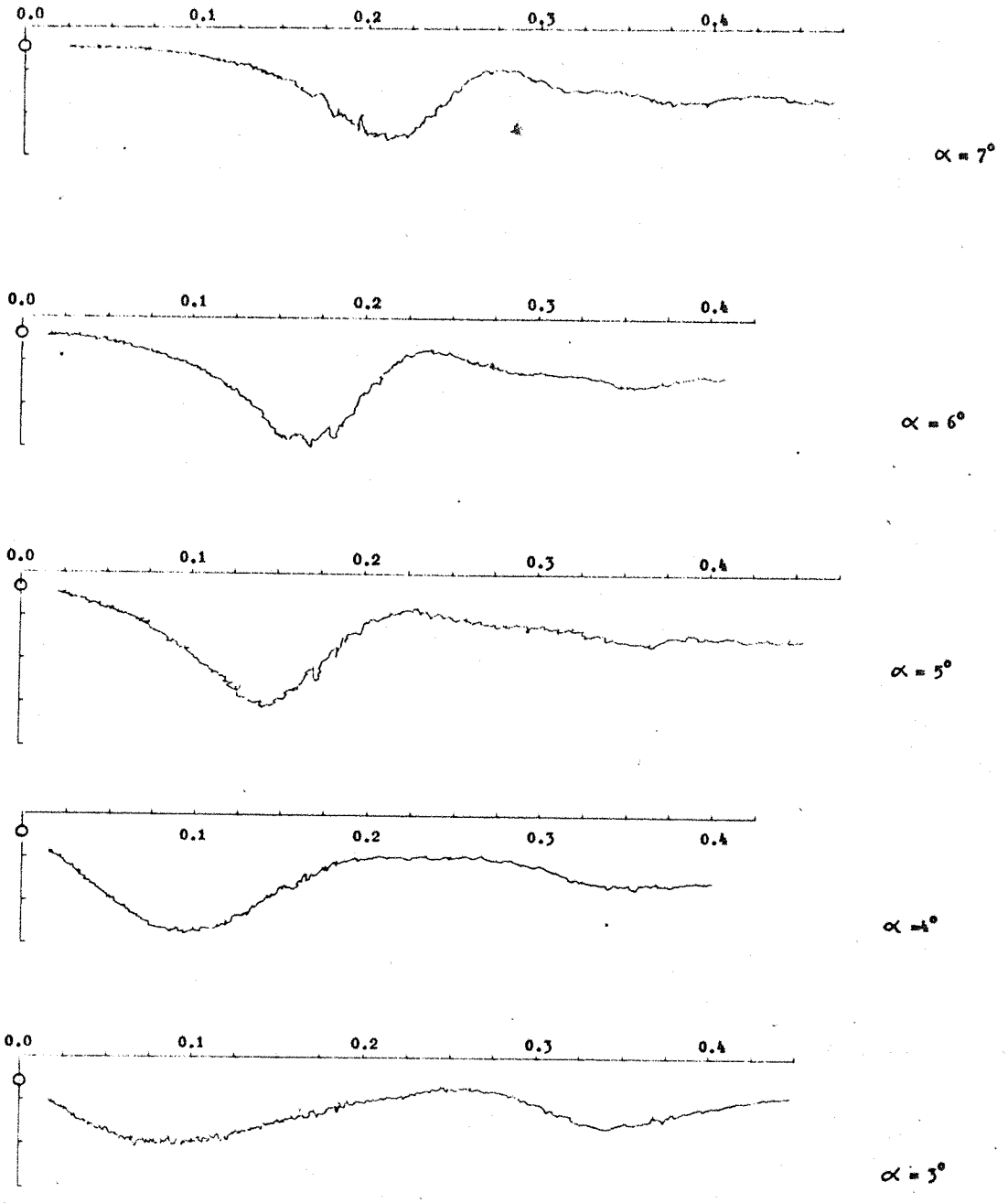

YAWING MOMENT COEFFICIENT VERSUS pD/2V

7-CAL OGIVE WITH HEMISPHERE BASE, CLEAN MODEL

C_T 0.1 UNITS/DIV

pD/2V 0.025 UNITS/DIV

FIGURE A15. CASE 3(b)

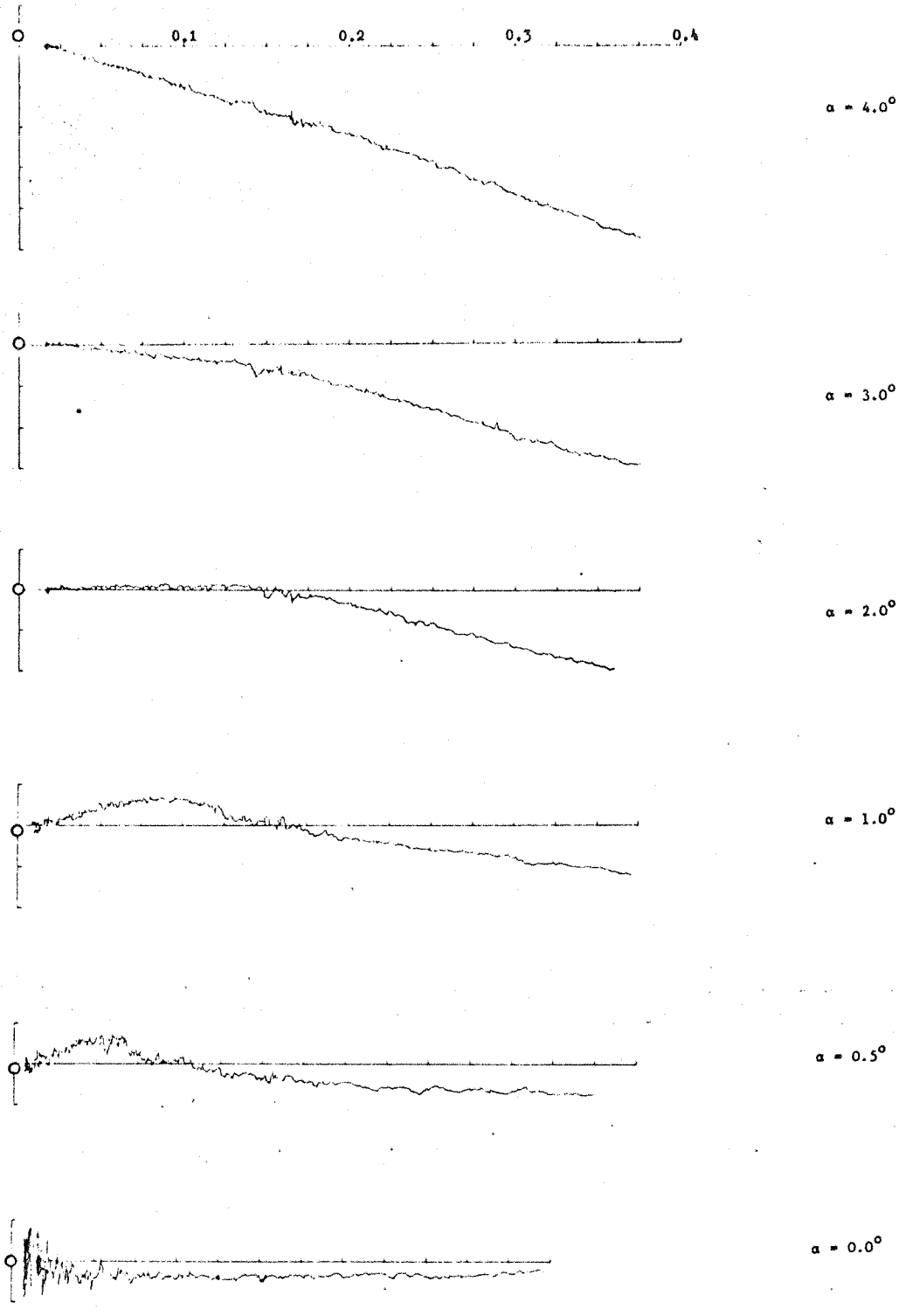

SIDE FORCE COEFFICIENT VERSUS pD/2V

7-CALIBRE OGIVE WITH ROUGHNESS BAND

5° HALF-ANGLE, ½-CALIBRE LENGTH BOATTAIL BASE

C_f 0.01 UNITS/DIV

pD/2V 0.025 UNITS/DIV

FIGURE A16. CASE 4

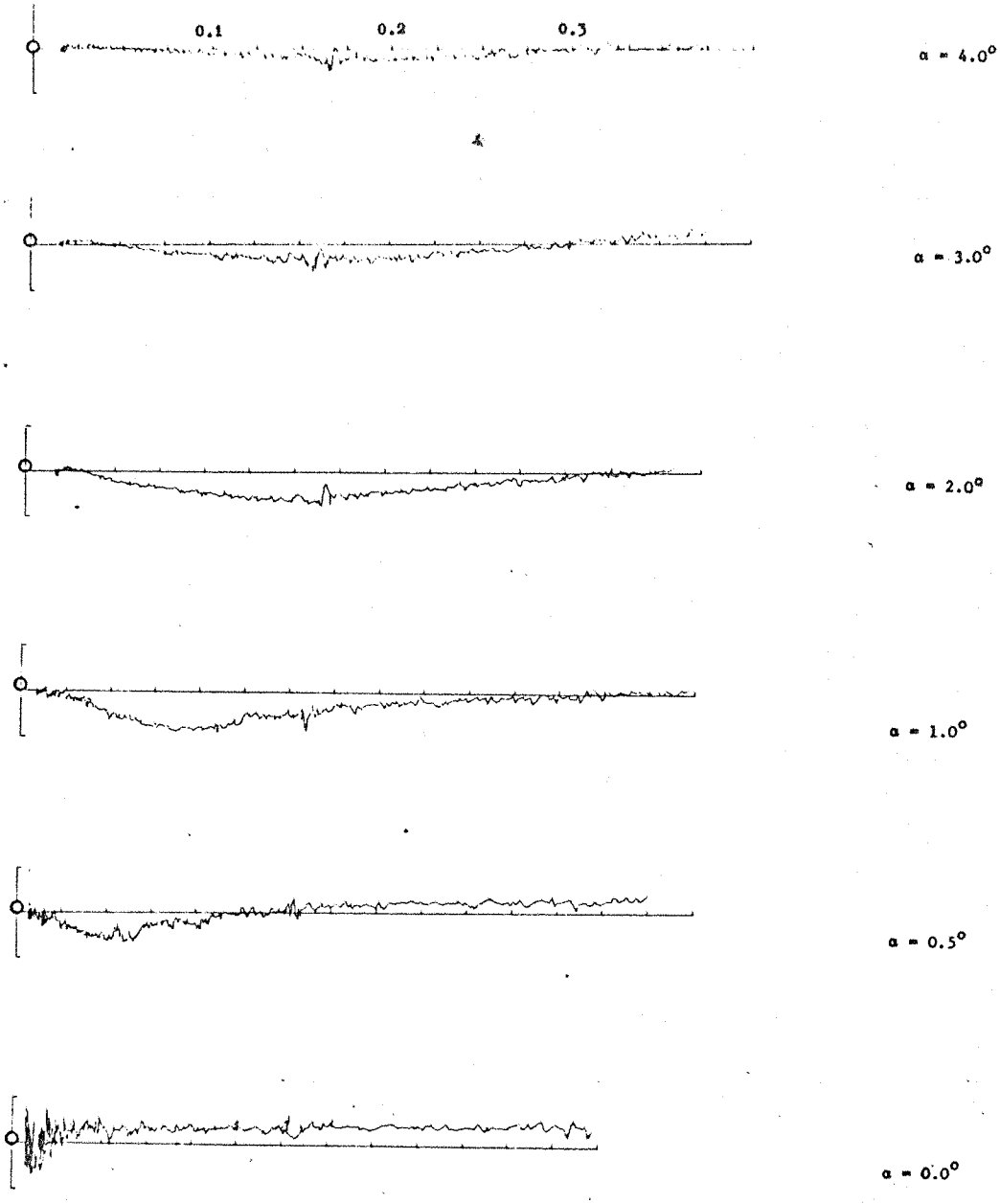

YAWING MOMENT COEFFICIENT VERSUS pD/2V

7-CAL OGIVE WITH ROUGHNESS BAND

5° HALF-ANGLE, ¼-CALIBRE LENGTH BOATTAIL BASE

C_T 0.025 UNITS/DIV

pD/2V 0.025 UNITS/DIV

FIGURE A17. CASE 4

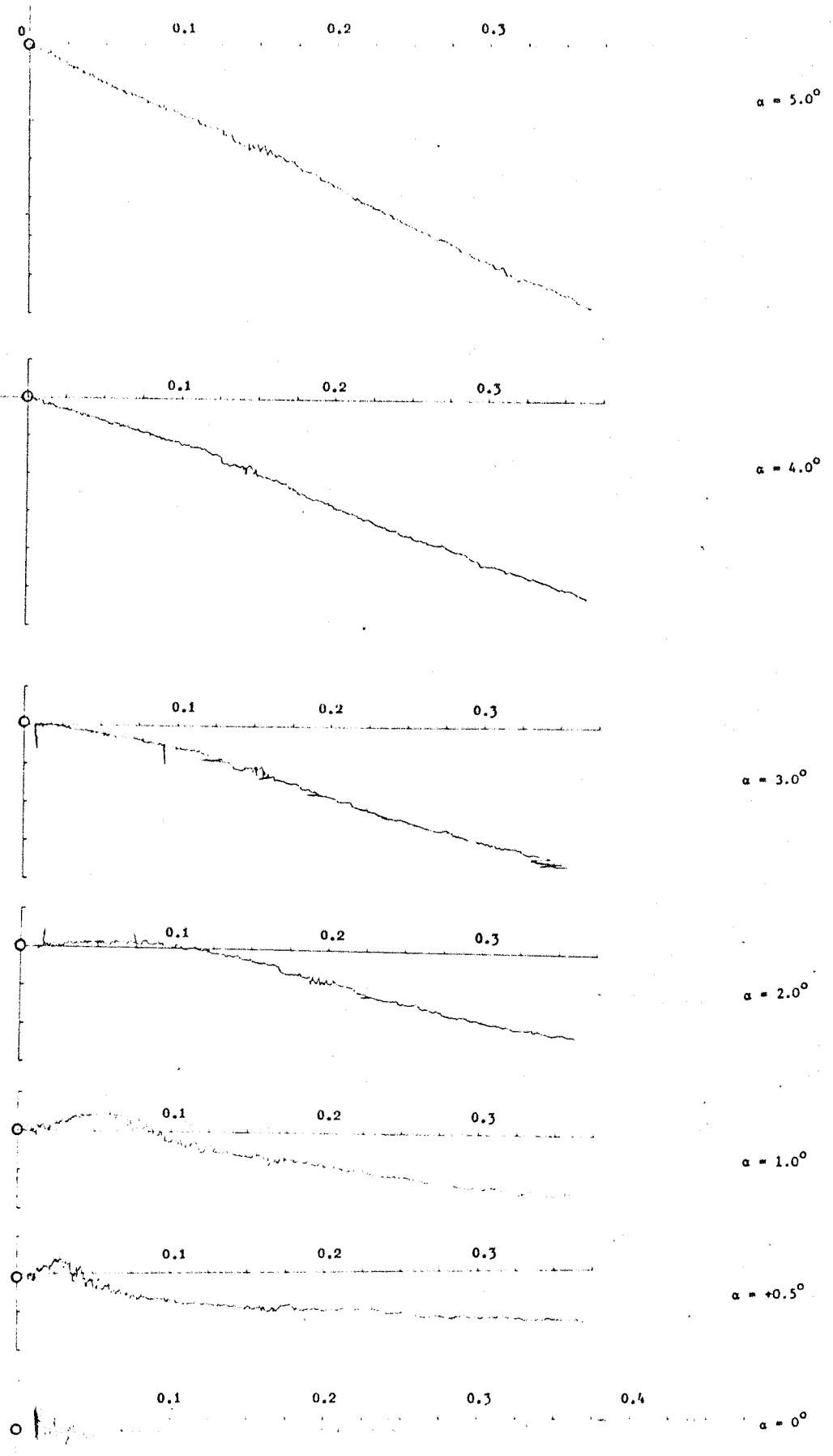

SIDE FORCE COEFFICIENT VERSUS pD/2/V

7-CALIBRE OGIVE WITH ROUGHNESS BAND

10° HALF-ANGLE, ¼-CALIBRE LENGTH BOATTAIL BASE

C_f 0.01 UNITS/DIV

pD/2V 0.025 UNITS/DIV

FIGURE A18. CASE 5

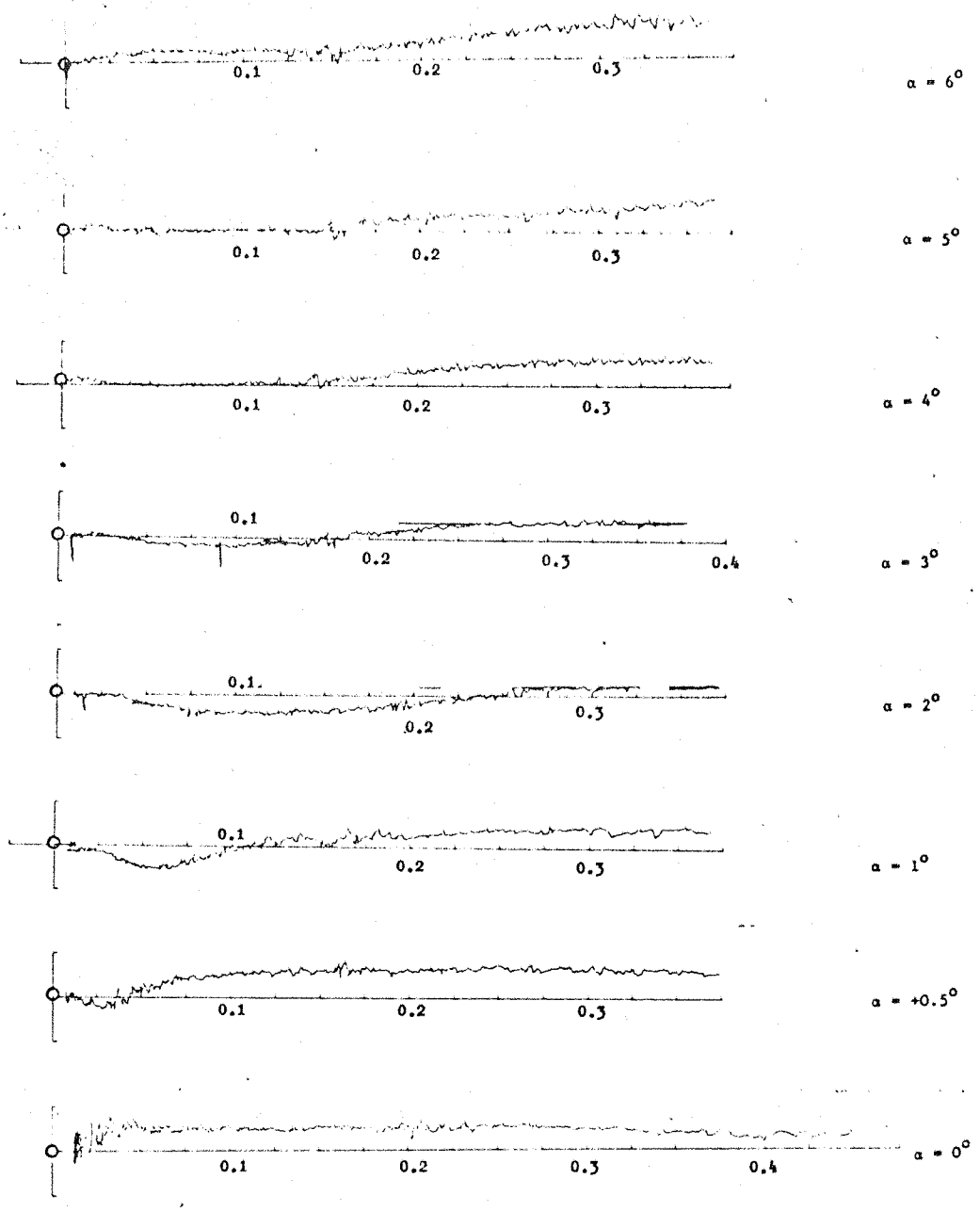

YAWING MOMENT COEFFICIENT VERSUS pD/2V

7-CAL OGIVE WITH ROUGHNESS BAND

10° HALF ANGLE, ¼-CALIBRE LENGTH BOATTAIL BASE

C_T 0.025 UNITS/DIV

pD/2V 0.025 UNITS/DIV

FIGURE A19. CASE 5

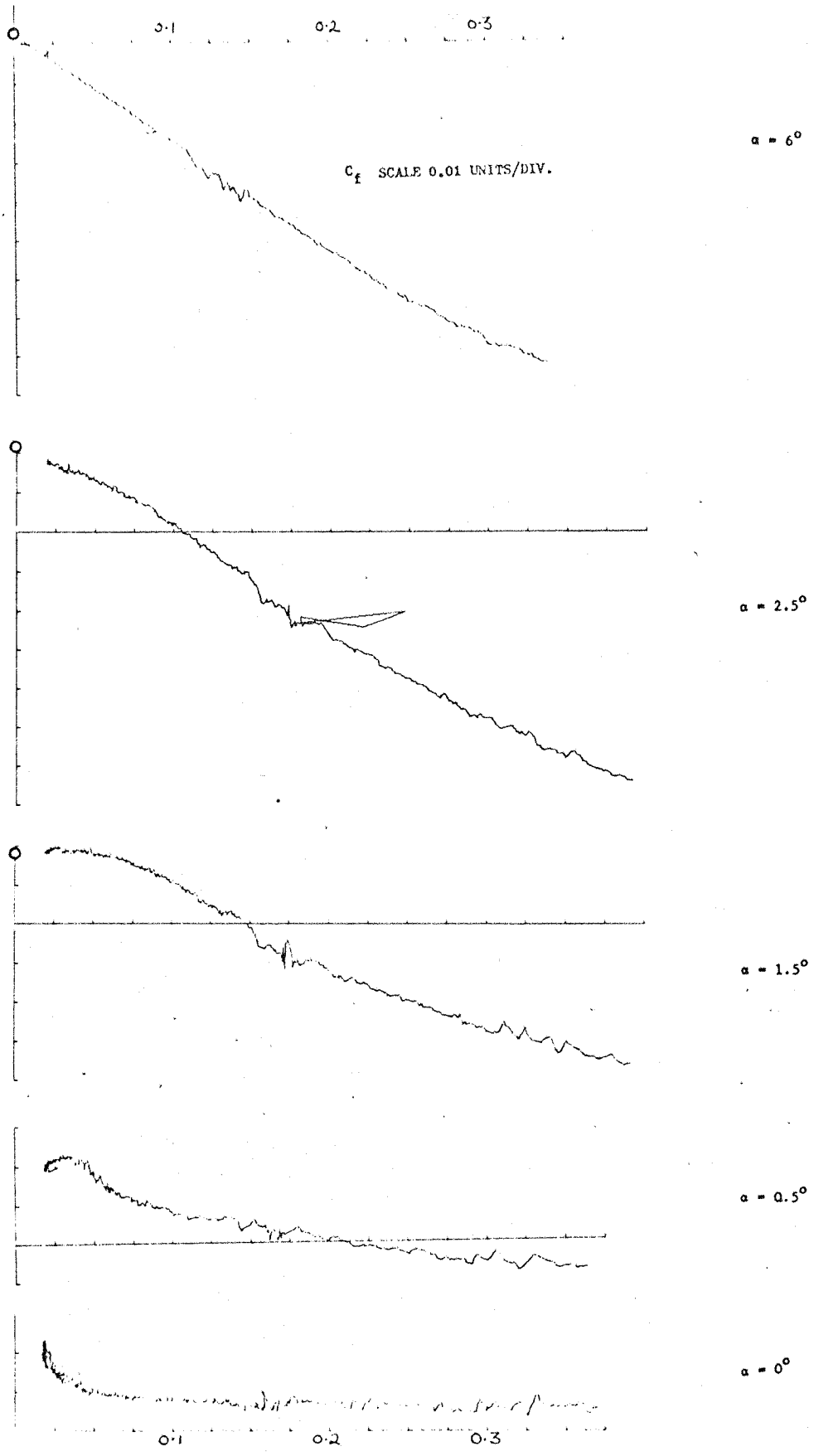

SIDE FORCE COEFFICIENT VERSUS pD/2V

7-CAL SPINNER WITH ROUGHNESS BAND

10° HALF-ANGLE, 1 CALIBRE LENGTH BOATTAIL BASE

C_f 0.005 UNITS/DIV

(EXCEPT α = 6°)

pD/2V 0.025 UNITS/DIV

FIGURE A20. CASE 7

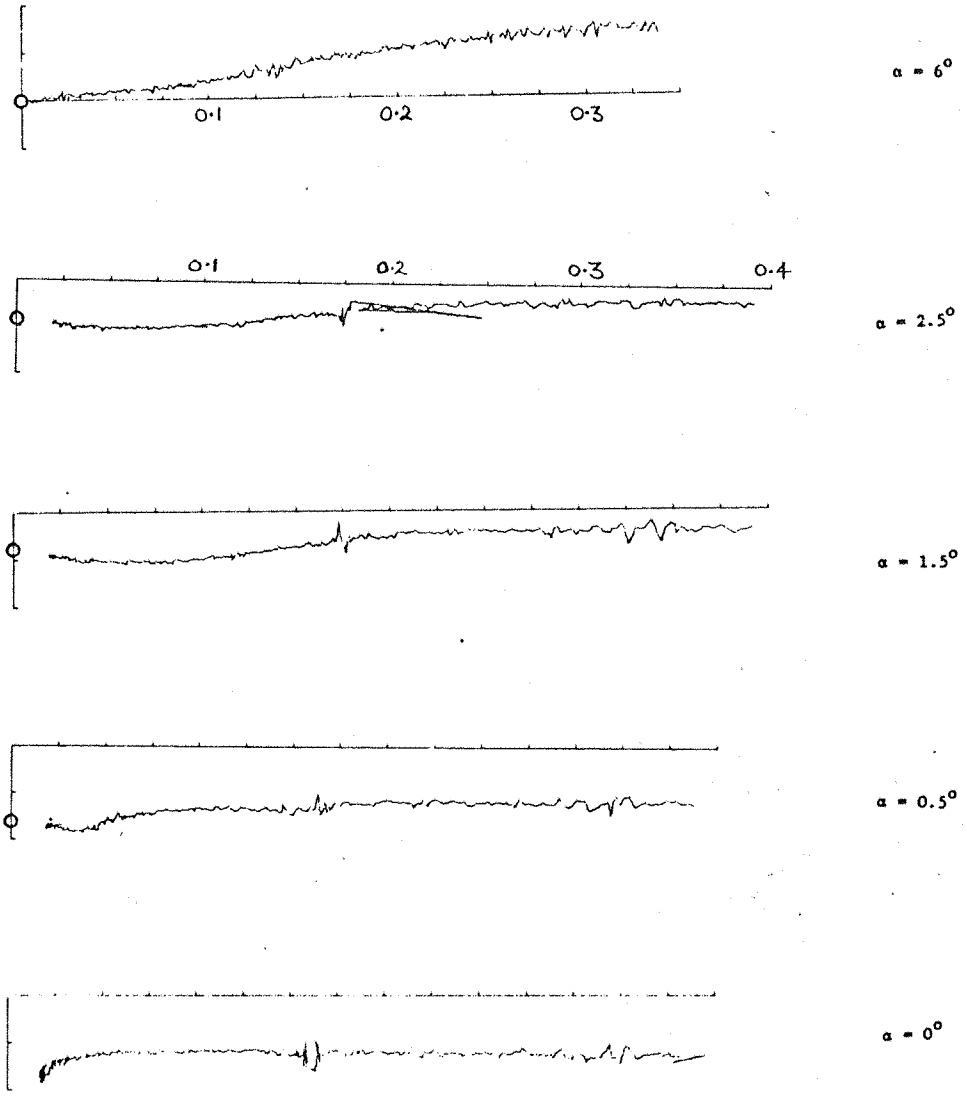

YAWING MOMENT COEFFICIENT VERSUS pD/2V — C_T 0.025 UNITS/DIV

7-CALIBRE AN SPINNER WITH ROUGHNESS BAND — pD/2V 0.025 UNITS/DIV

10° HALF-ANGLE, 1 CALIBRE BOATTAIL BASE

FIGURE A21. CASE 7

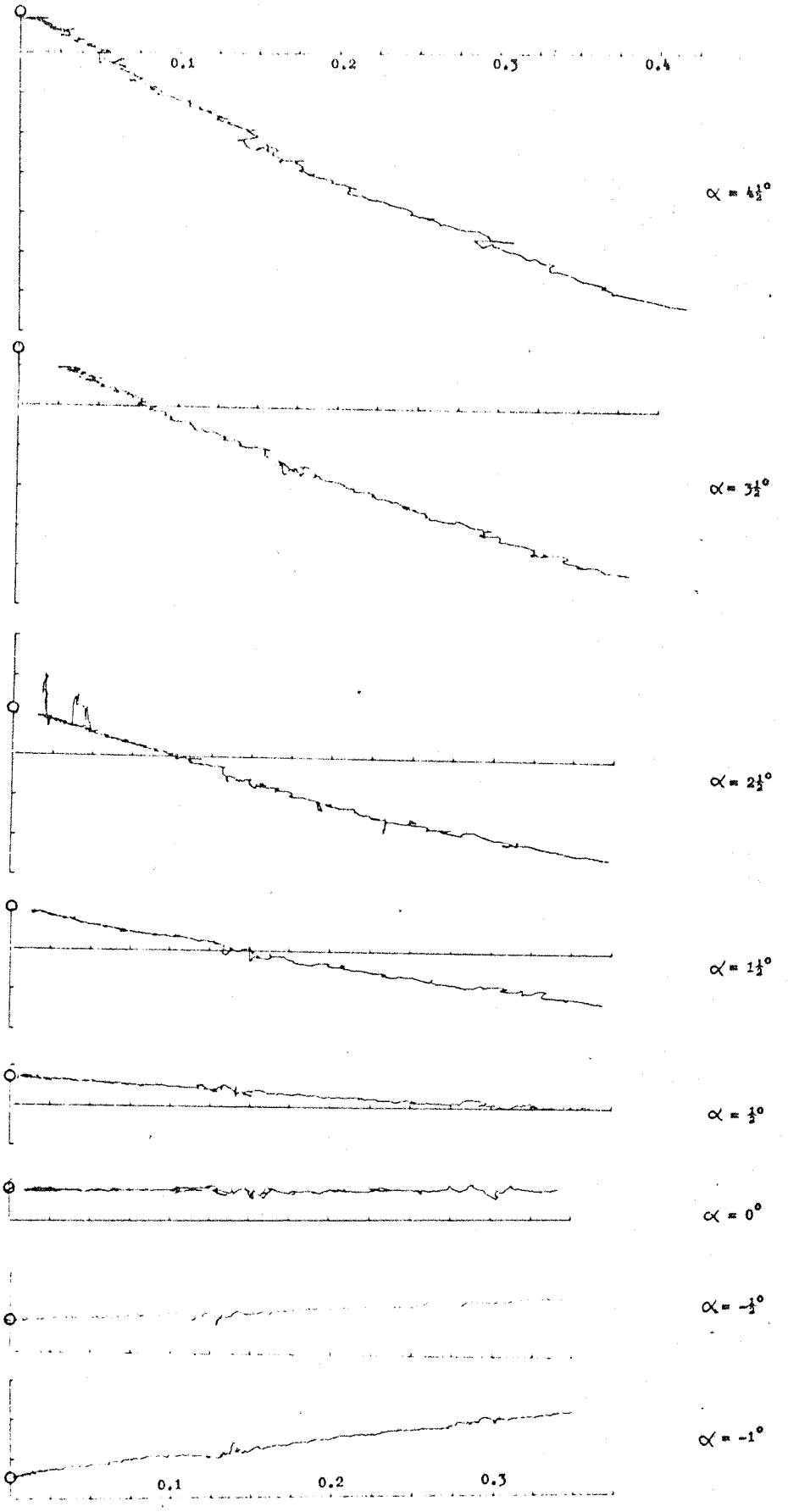

SIDE FORCE COEFFICIENT VERSUS pD/2V

7-CALIBRE OGIVE CYLINDER WITH ROUGHNESS

10° HALF ANGLE, 1 CALIBRE LENGTH BOATTAIL,

WITH 0.213D CAVITY

C_f: 0.01 UNITS/DIV

pD/2V: 0.025 UNITS/DIV

FIGURE A22. CASE 9

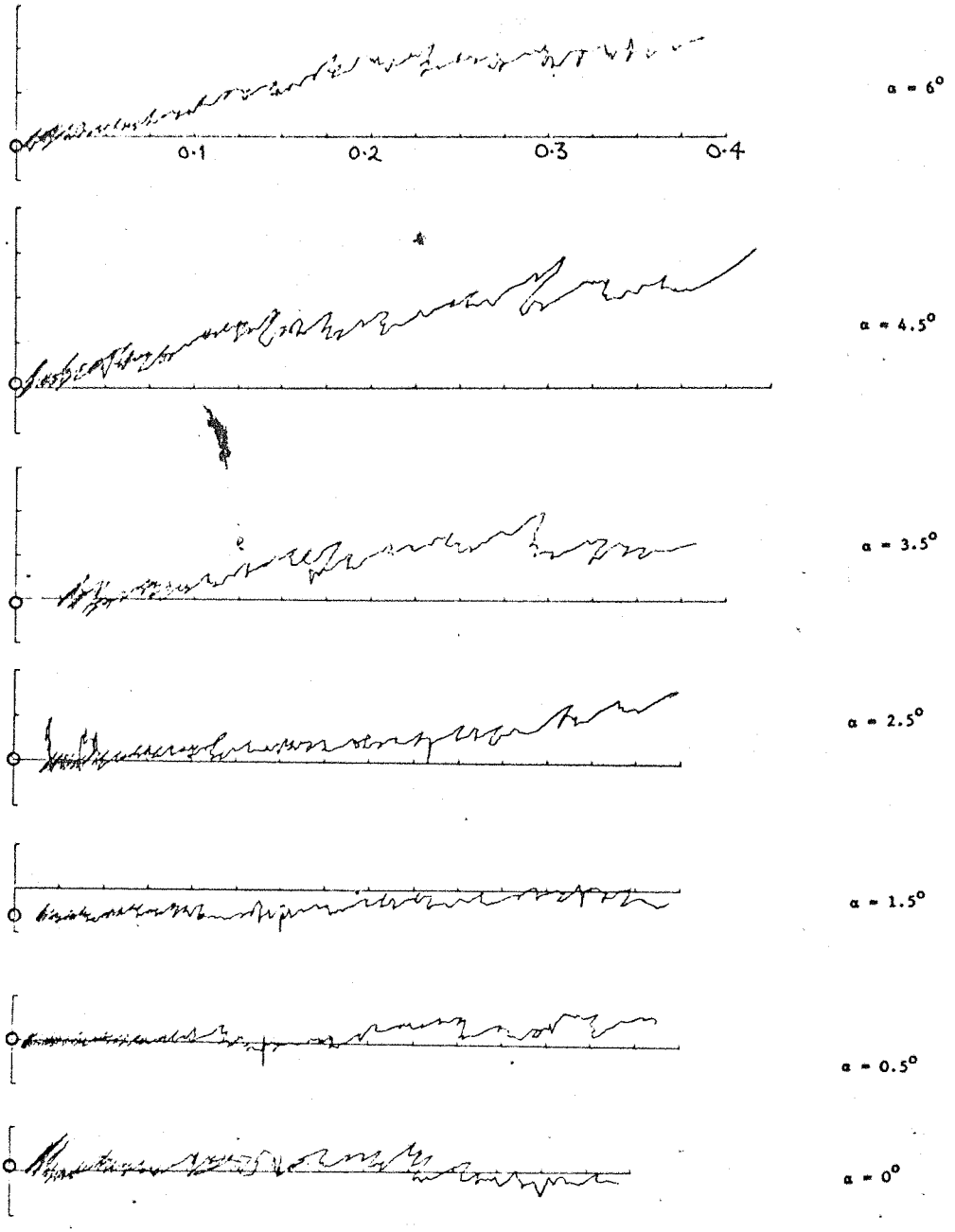

YAWING MOMENT COEFFICIENT VERSUS pD/2V

7-CALIBRE AN SPINNER WITH ROUGHNESS BAND

10° HALF ANGLE, 1 CALIBRE LENGTH BOATTAIL,

WITH 0.213D CAVITY

C_T 0.025 UNITS/DIV

pD/2V 0.025 UNITS/DIV

FIGURE A23. CASE 9

APPENDIX B

THE EFFECT OF THE PRESENCE OF A STING SUPPORT ON THE SUBSONIC DRAG COEFFICIENT OF A BLUNT BASED PROJECTILE AT ZERO INCIDENCE.

Introduction.

Measurements were made to determine the relationship between the diameter of a sting support and the zero incidence drag coefficient of the 7-calibre AN Spinner, using the magnetic balance and suspension system[24]. The outline of the model is shown in figure 3.1. The correlation between drag coefficient and base pressure values was was investigated. Five degrees of freedom of motion of the model were controlled magnetically, roll control being unnecessary, as imbalance and magnetic asymmetry of the model were sufficient to prevent rolling of the model during wind-on tests. In order to use the suspension system as a force balance, there must be no mechanical support between the model and the sting. However, their separation must be kept as small as possible, so as to mimic closely the flow around a mechanically supported model.

Experimental Hardware.

The interchangeable stings were of equal length, with a flare half-angle of 7.5 degrees, and were bolted to a knuckle joint at the end of a 25 mm diameter tubelar support arm. The support arm could be clamped in a range of vertical positions on a rigid stainless steel cross piece (See figure B-1). With this arrangement, the length of the tubular section of the sting (ℓ) was a function of sting diameter (d), but the ratio ℓ: d was greater than 9:1 in all cases. The ratio ℓ : D_B ranged from 9:1 to 6.5:1. Here, D_B is the body diameter.

Each sting was a length of brass tubing, blocked at its upstream end with epoxy resin. The resin was pierced with a cental hole 1 mm in diameter to enable base pressure to be measured. At the downstream end, a short length of stainless steel tube was joined to the sting. Base pressure was communicated to a vernier reading manometer by means of a length of 3 mm PVC tubing.

The second arm of the manometer was connected to an aperture in the wall of the working section 0.5 m upstream of the model. Size details of the stings tested are given in Table B.1.

The model consisted of a 22 mm diameter aluminium shell with ogive nose, scaled to the dimensions of the 7-calibre AN Spinner (See figure 3.1*). The model contained an Alcomax III permanent magnet. To avoid obstruction of the optical position sensor by the dummy sting, the axial light source and photocell were removed to the upstream end of the model (See also section 6.2).

Method.

The model was suspended at nominal zero incidence and controlled in axial position. The sting was positioned a small distance from the base (0.5 - 1.5 mm). With wind on, digital voltmeter readings proportional to the suspension coil currents were recorded. This was carried out with, and without the sting present. The sting could be disconnected from the 25 mm tubular support and removed from the working section in approximately one minute. Measurements of dynamic head were made using a second manometer. Both manometers contained methylated spirit of specific gravity 0.816. Precision of measurement was approximately $\pm$ 2 mm or $\pm$ 0.5% at the maximum dynamic head of 400 mm. Maximum flow velocity was 66 metres per second, giving a maximum Reynolds number of 0.77×10^6 based on model length.

In order to minimise the effect of various random drifts in the system, measurements of the absolute drag force were not made, but the digital voltmeter readings taken in the presence and in the absence of a sting were compared to produce the ratio of the two drag forces. Previous measurements of the absolute values on this balance gave $C_D = 0.26$ for the smooth model, and $C_D = 0.29$ for the model with a 0.25 mm 'trip wire' attached at the shoulder. These values are accurate to approximately $\pm$ 0.01.

The effect of dynamic head variations on the measured ratio of the drag coefficients was investigated for five different sting diameters. Over the range of flow velocities 33 - 66 metres per

---

* In these tests, a tripping wire was attached at the shoulder when a fully turbulent boundary layer was required. Grit was not used.

second, it was concluded that any change was smaller than the amplitude of the scatter on the measured data, i.e. less than $\pm$ 0.005. This applied both with and without the boundary layer trip applied.

The ratio of the drag coefficients was similarly found to be insensitive to movement of the sting from the base by several millimetres. As an example, the axial coil current (to first order, proportional to drag force) is plotted in figure B-2 as afunction of sting separation from the base. These measurements were made with a sting of 6.3 mm diameter, and with both model and sting inclined at 12° to the tunnel flow. Despite the latter condition, the figure serves to illustrate the point that the precise distance between the base and the end of the sting need not be maintained constant to an accuracy greater than approximately $\pm$ 1 mm. In fact, the sting was kept between 0.5 and 1.5 mm from the base for all the measurements.

Base Pressure Measurement.

Measurements of the quantity $p_b - p_2$, where p_2 is the upsteam static pressure and p_b is the base pressure as measured at the end of the dummy sting, were made during the test runs in which the drag force was measured with the sting present. The vernier scale manometer enabled pressure readings to be made with an accuracy of $\pm$ 0.025 mm.

Reduction of the Data.

The drag coefficient is defined by

$$C_D = D/q_1 S$$

and the base pressure coefficient by

$$C_{PB} = \frac{p_b - p_1}{q_1},$$

where p_1 = test section static pressure
q_1 = test section dynamic pressure
p_b = base pressure
p_2 = static pressure 0.5 m upsteam of model

q_2 = dynamic pressure 0.5 m upstream of model

S = base area of model

D = drag force.

To calculate the base pressure coefficient, C_{PB}, a blockage correction was applied to the measured value of $p_b - p_2$. The effect of blockage by sting support and model on the dynamic and static pressure at the position of the model is illustrated in figure B-3. From the slope of this graph the ratio q_2/q_1 was calculated to be 0.98. Using this result, the base pressure coefficient becomes

$$C_{PB} = 0.98 \frac{p_b - p_2}{q_2} + 0.02.$$

The base drag coefficient is defined by

$$C_{DB} = \frac{-\int (p_b - p_1) dS}{q_1 S} = -\frac{\int C_{PB} dS}{S}.$$

For the case of a uniform distribution of base pressure, C_{PB} is not a function of position on the base and

$$C_{DB} = -C_{PB}.$$

Results

C_D and C_{DB} are plotted as a function of sting diameter in fugure B-4, on the assumption of uniform base pressures. Both sets of data show an upward trend in the coefficients as the sting diameter is increased beyond 0.5 D_B. This appears to reach a maximum where $0.6 < d/D_B < 0.8$ and is followed by a rapid decrease as d/D_B approaches unity. The addition of a 0.25 mm diameter 'tripping wire' at the shoulder in an attempt to develop a fully turbulent boundary layer over the model increased the total drag coefficient by approximately 0.03. However, the base drag coefficient was reduced by approximately 0.02.

The difference between the coefficients ($C_D - C_{DB}$) remained nearly constant over the range of sting diameters. This applies even to the case with $d/D_B = 1$, where C_{DB} changes sign.

TABLE B.1

Dummy Sting Sizes

Nominal Diameter(in.)	Measured Diameter (d)	d/D_B
0.125	0.118	0.136
0.250	0.247	0.285
0.3125	0.310	0.358
0.375	0.375	0.433
0.4375	0.438	0.505
0.500	0.500	0.577
0.625	0.625	0.721
0.750	0.755	0.871

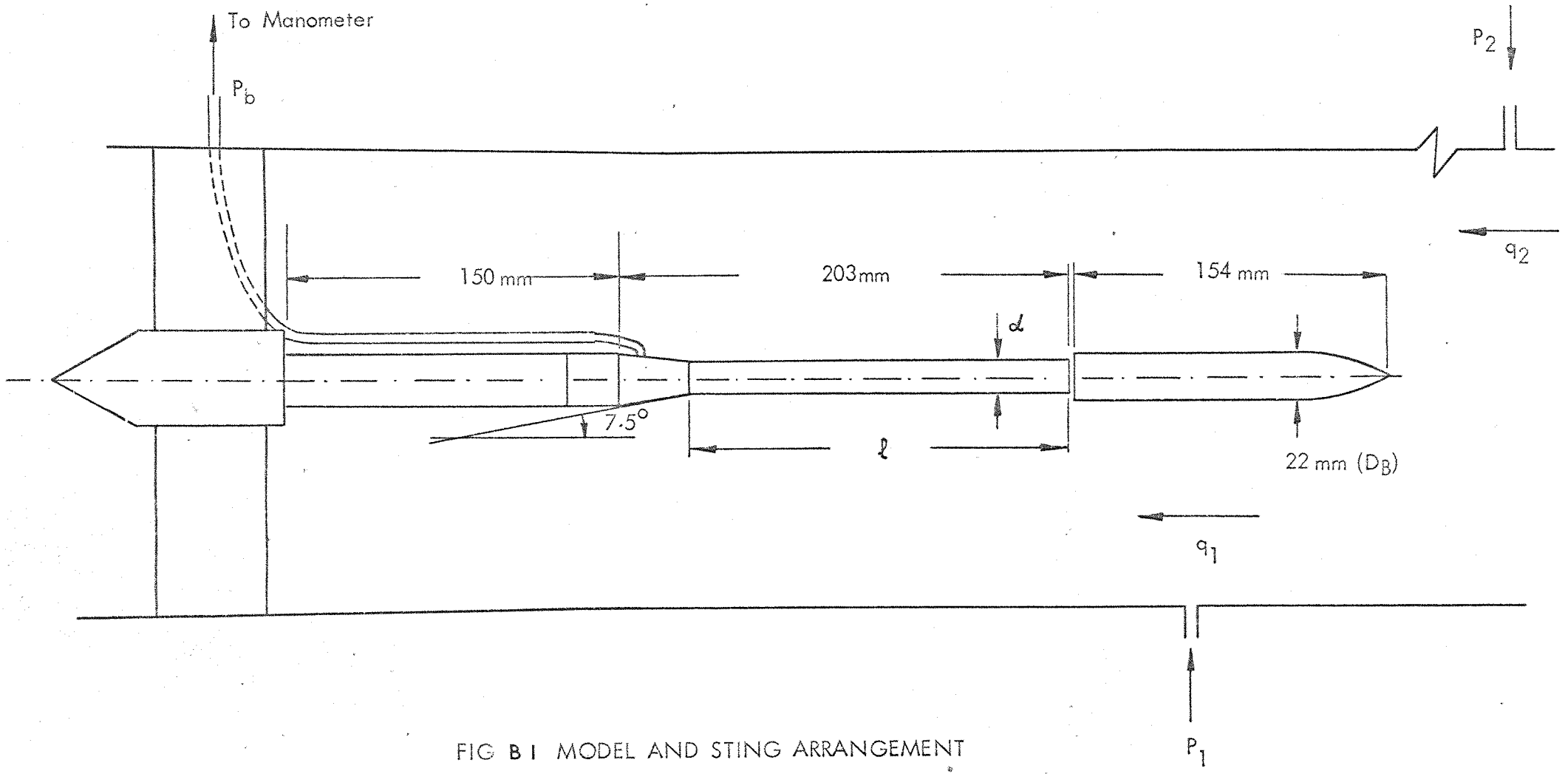

FIG B I MODEL AND STING ARRANGEMENT

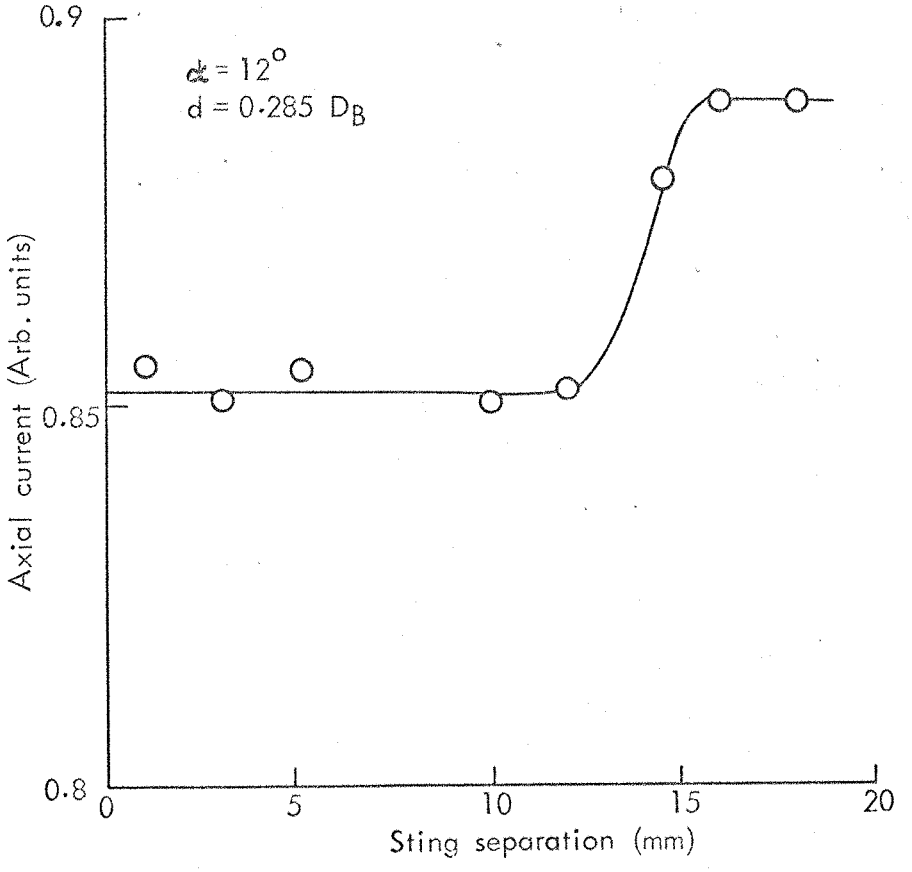

FIG B 2 EFFECT OF STING SEPARATION ON AXIAL FORCE

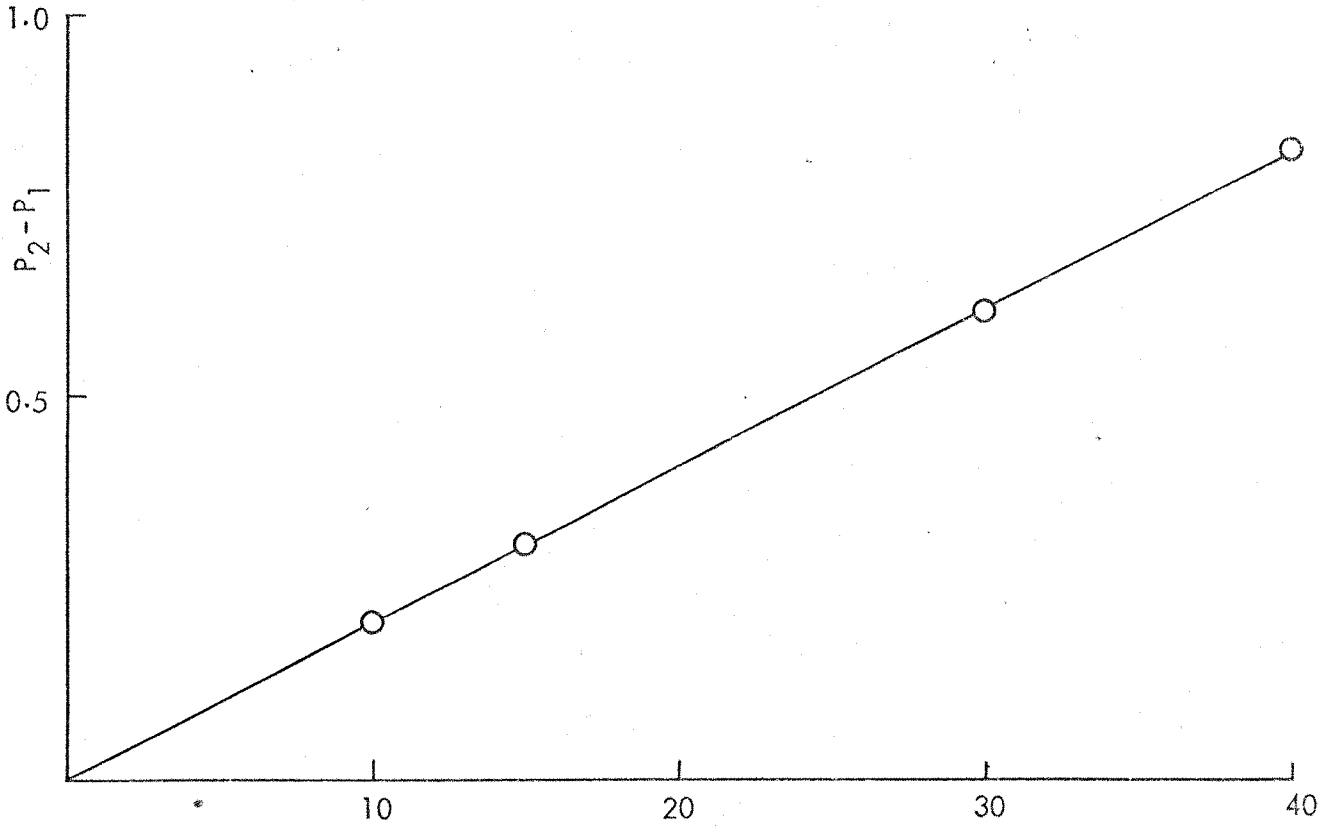

Dynamic head q_2 derived from tunnel calibration (units for both scales are GM/CM^2)

FIG B 3 EFFECT OF MODEL BLOCKAGE

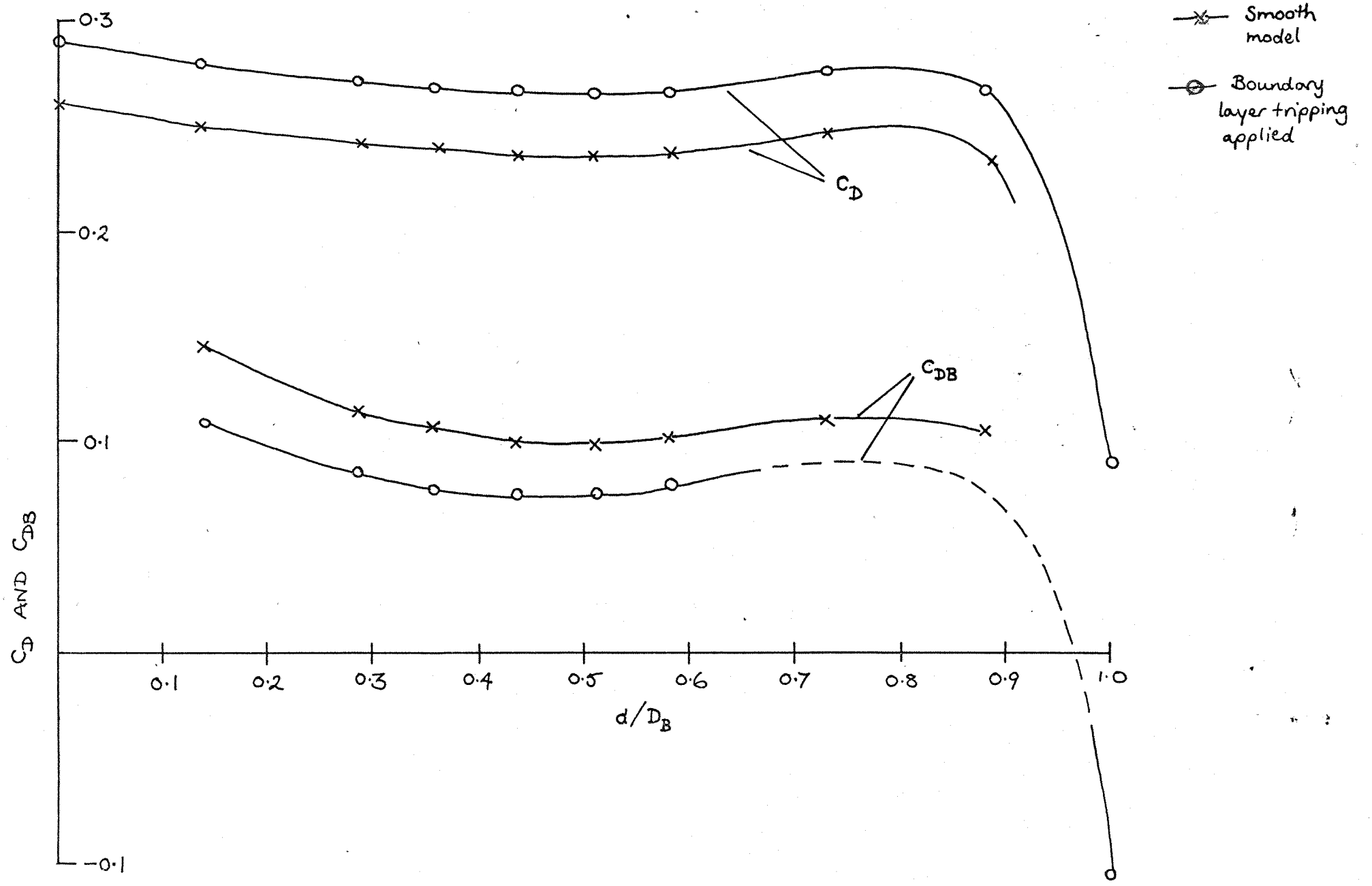

FIG. 34. TOTAL DRAG COEFFICIENT (C_D) AND BASE DRAG COEFFICIENT (C_{DB}) AS A FUNCTION OF DUMMY STING DIAMETER (d)

APPENDIX C

MEASUREMENTS OF THE WIND TUNNEL FLOW ANGULARITY

Introduction

The first Magnus force measurements made with the magnetic suspension balance were confined to the low pD/2V regime (see section 7.2)[17]. The model used was the basic 7-calibre AN spinner, having a blunt base, and the pitch incidences ranged from $+1^{o}$ to $+7.5^{o}$. Only anticlockwise rotation of the model was possible. Data at zero incidence was precluded by temporary difficulties with spinning the model at that incidence.

As a result of the lack of zero incidence data, and the vanishing of the Magnus force derivative ($\partial C_f / \partial(pD/2V)$) at a pitch incidence of approximately 3^{o}, the data appeared to suggest the possibility of a flow angularity of 3^{o} in the test section. This uncertainty prompted the investigation described in this appendix.

Equipment

The experimental equipment consisted of a 5-hole 'yaw probe' supported in the test section at the approximate location of the model. The probe itself was a 100 mm length of stainless steel tubing with a conical end (cone half-angle 45^{o}). Five pressure tappings on the cone were connected through PVC tubing to a manometer outside the wind tunnel containing methylated spirit.(See Fig. C1).

The probe support was one of the 'dummy' stings used in the sting interference measurements of Appendix B and mounted on its support structure. The probe was strapped to a 'vee' block fitted on to the end of the sting. The probe could easily be removed, turned through 180^{o} about its own axis, and replaced in position, leaving its angle of incidence unchanged. It was desirable to provide this facility, since by taking the average of pressure readings made with the probe in the two opposite attitudes, any pointing error inherent in the probe could be eliminated.
A diagram of the experimental arrangement is shown in Fig. C2.

The angle of incidence of the probe was altered manually, with the sting and probe pivoting at the knuckle joint on the sting support. The distance from the end of the probe to the pivot was 294 mm.

The incidence of the probe was measured by means of a height gauge. Readin s were taken of the height of both ends of the probe above the floor of the working section. By this means, the angle of incidence could be measured with an accuracy of $\pm 0.2^{\circ}$ relative to the tunnel floor. The relative accuracy of measurement was greater, being approximately $\pm 0.05^{\circ}$.

Method

The wind tunnel dynamic head was maintained at 300 mm of water for all the tests. This corresponded to a working section flow velocity of 71.5 metres/second. The pressure readings for two opposing pairs of pressure tappings on the probe were noted, the two tappings being set in the same vertical plane. The probe was then removed from the 'vee' block, turned through 180°, and replaced. The second pair of readings was then taken, with the tunnel dynamic head at the same level.

This series of measurements was repeated at several angles of incidence. The measurement of the angle of incidence was carried out as described above. The height of the upstream end of the probe was kept constant, and the downstream end of the support was moved vertically on the stainless steel cross piece.

Results

The mean pressure difference between the two tappings on the probe was plotted against measured incidence of the probe. The result is shown in figure C3. The units of pressure difference are millimetres of methylated spirit, and the incidence is plotted in degrees.

The angle at which the pressure difference is zero is $-0.45^{\circ} \pm 0.2^{\circ}$. Negative incidence indicates that the probe points upwards. The floor of the working section is angled slightly in order to compensate for boundary layer growth (see section 2.1). A flow angularity relative to the tunnel floor of -0.25° is therefore expected, since the vertical dimension of the test section diverges at an angle of 0.50°. The results thus suggest zero flow angularity, within the tolerance of measurement.

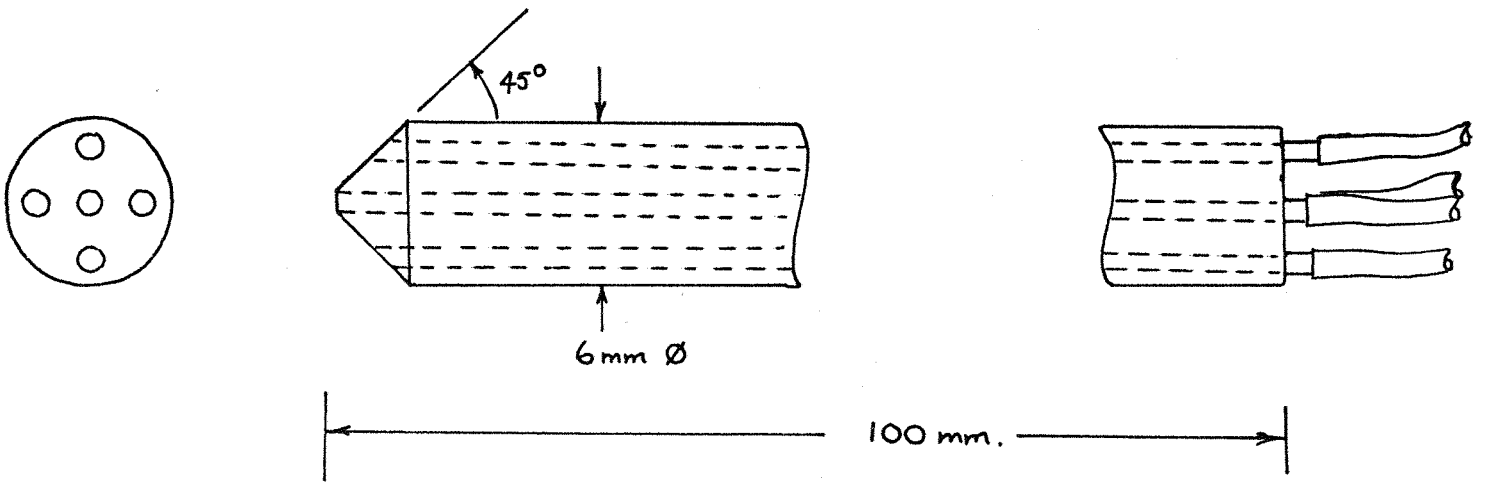

FIG. C1. THE YAW PROBE

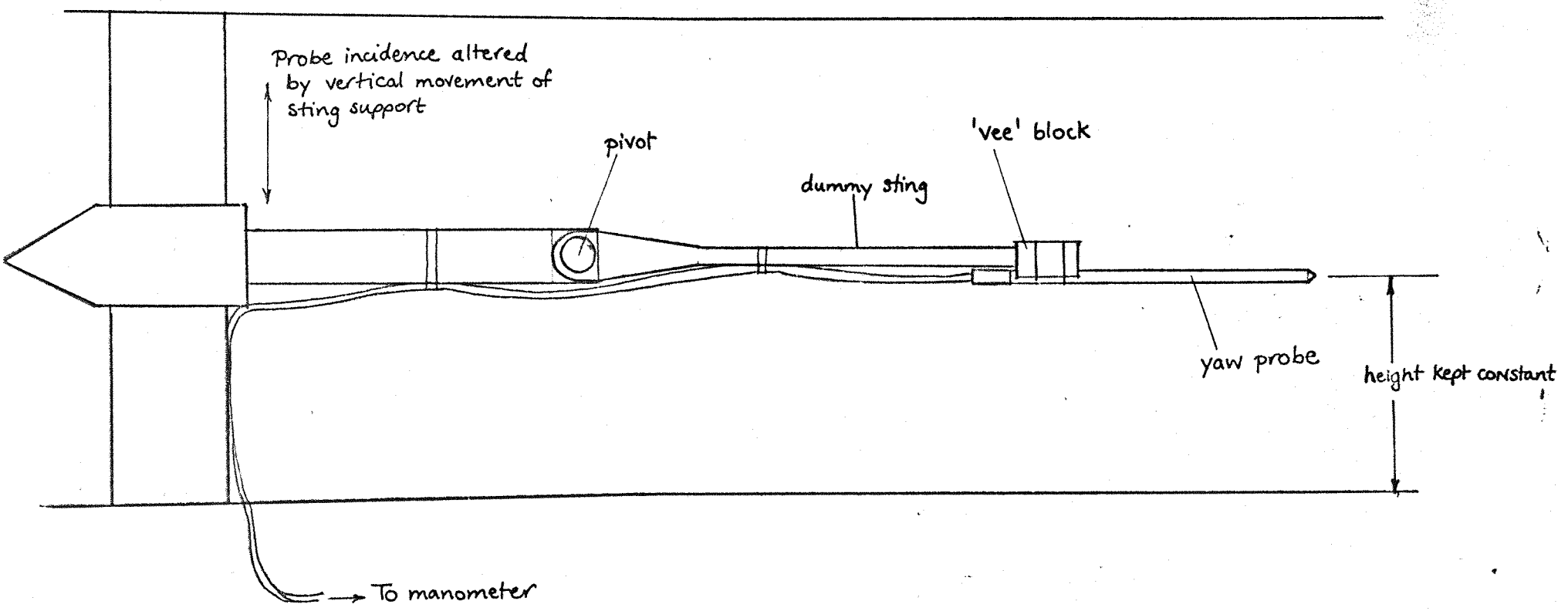

FIG. C2. EXPERIMENTAL ARRANGEMENT FOR THE FLOW ANGULARITY TESTS

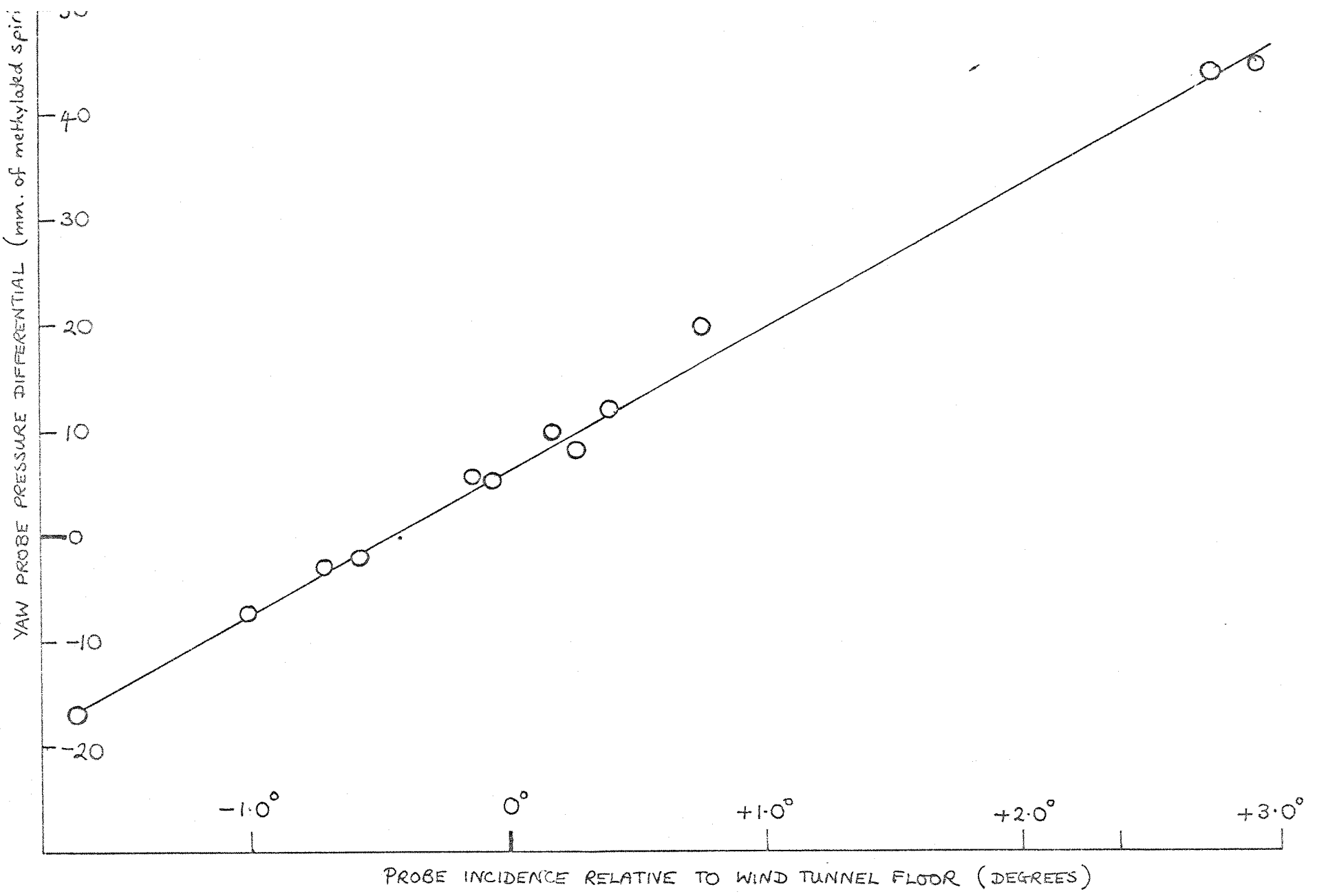

FIG. C3. YAW PROBE PRESSURE DIFFERENCE AS A FUNCTION OF MEASURED ANGLE OF INCIDENCE

APPENDIX D

MEASUREMENTS OF THE WIND TUNNEL TURBULENCE LEVEL

Introduction

As a supplement to the aerodynamic measurements of steady and Magnus coefficients on the 7-calibre AN spinner, the wind tunnel turbulence level was measured. The measurements were of the simplest kind, being an evaluation of the root mean square fluctuations in the direction of the mean flow.

Equipment

The test equipment consisted of a hot-wire anemometer with associated electronics, and a Hewlett Packard true r.m.s. meter. The hot wire probe was a single wire device; the wire diameter was 0.005 inches (0.12 mm) and its length approximately 3 mm. The wire is supplied with a constant current, which raises its temperature above ambient. The wire is placed perpendicular to the direction of the mean flow. Fluctuations in the velocity component in the direction of the mean flow cause changes in the heat transfer rate from the wire to the stream, and this in turn leads to fluctuations in the resistance of the wire. With a constant current maintained in the wire, these resistance variations give rise to voltage fluctuations across the wire terminals which can be amplified and fed to an r.m.s. meter to indicate turbulence level.

Owing to the non-linear characteristic of the hot wire anemometer, a linearising circuit is included in the electronics package. Calibration of the anemometer requires immersing the probe in a flow of known velocity. In the present case, the tunnel manometer provided calibration at a velocity of 250 feet/sec (76.2 metres/sec.)

Method

The hot wire probe was strapped to one of the 'dummy' stings used in the flow interference tests described in Appendix B. Its position was nominally on the centre line of the tunnel, and near the centre of the working section.

Setting up the probe required the adjustment of the current through the hot wire. The adjustments were outlined in the manual supplied with the anemometer. The damping factor of the circuit controlling the hot wire current also required adjustment for each individual probe. Calibration of the device entailed running the wind tunnel at a known flow speed (76.2 metres/sec) and adjusting the gain of the output stage of the anemometer amplifier. The calibration was carried out such that an output of 1 volt corresponded to a flow speed of 50 feet/second (15.2 metres/sec).

With the probe calibrated, the tunnel was run at a number of representative air speeds up to 76.2 metres/second, and the root mean square voltage fluctuations were measured using the r.m.s. voltmeter for each speed.

Results

The r.m.s. velocity fluctuations in the direction of the mean flow are tabulated in Table D1 for 5 flow speeds. The level appears to settle down to 0.15% over the range of speeds used in the steady and Magnus measurements described in this thesis. This is rather higher than typical for a tunnel of this kind, and this may be the result of disturbances in the diffuser caused by noise and turbulence from the injectors[25].

TABLE D1

Longitudinal component of turbulent intensity at 5 flow velocities

Mean flow velocity	R.M.S. velocity fluctuations	
U	$\sqrt{\overline{u^2}}$	$\sqrt{\overline{u^2}}/U$
(metres/sec)	(metres/sec)	(%)
76.2	0.12	0.15
61.0	0.092	0.15
45.8	0.069	0.15
30.4	0.056	0.185
15.2	0.031	0.20